

Epigraph

If we knew what it was we were doing,
it wouldn't be called "research", would it?

- Albert Einstein

University of Alberta

Development of Microfluidic Chips and a Customised Flow Control System for use in a Label-Free Cytometer

by

Debbie Feng Shan Ha

A thesis submitted to the Faculty of Graduate Studies and Research
in partial fulfillment of the requirements for the degree of

Master of Science

in

Microsystems and Nanodevices

Department of Electrical and Computer Engineering

©Debbie Feng Shan Ha
Fall 2013
Edmonton, Alberta

Permission is hereby granted to the University of Alberta Libraries to reproduce single copies of this thesis and to lend or sell such copies for private, scholarly or scientific research purposes only.

Where the thesis is converted to, or otherwise made available in digital form, the University of Alberta will advise potential users of the thesis of these terms.

The author reserves all other publication and other rights in association with the copyright in the thesis and, except as herein before provided, neither the thesis nor any substantial portion thereof may be printed or otherwise reproduced in any material form whatsoever without the author's prior written permission.

Abstract

Conventional cytometry uses fluorescently labeled cells that are laborious and costly to prepare. Using a label-free technique, individual cells can be differentiated by light scattering patterns, a result of different physical attributes. This thesis describes the development of a microfluidic label-free cytometer. The key components include a microfluidic chip, a laser light scattering system for cell characterization, and a microfluidic flow control system. A PDMS microfluidic chip was developed and described in detail. A customised flow control system with sorting functionality was constructed to respond faster than commercial pumps. The linear relationship between applied pump pressure and average flow speed was confirmed experimentally, as well as a sorting flow response of 48.3ms or less. Results from laser light scatter experiments with different biological cells were presented, where scatter patterns for each cell type were visually distinguishable.

Contents

1	Introduction	1
1.1	Niche market for label-free technology	2
1.1.1	VSEL stem cells	2
1.1.2	Screening of pathogens in blood	5
1.1.3	Other Applications	6
1.2	Outline	7
2	Background on label-free cell imaging	9
2.1	Current cytometric technologies and their basic components	10
2.2	Light scattering spectroscopy	12
2.3	Mie scattering theory	14
2.4	Importance of organelles	17
3	Microfluidics background	24
3.1	Laminar flow	26
3.2	Pressure-driven flow	27
3.2.1	Hydrodynamic focusing	28
3.2.2	Shear force	33
3.3	Available pressure driven flow systems	35
4	Microfluidic chip design for laser light scattering of cells	40
4.1	Choice of materials	40
4.1.1	Optical properties	41
4.1.2	Reducing background noise level	43
4.1.3	Surface properties	45
4.1.4	Bonding	46

4.1.5	Biological compatibility	48
4.2	Optical guiding	49
4.3	Channel width	51
4.4	Modified PDMS chip	52
4.4.1	Fabrication	53
4.4.2	Reducing surface roughness	59
5	Measurement of bead and biological cell scatter	62
5.1	Sample preparation	63
5.2	Setup and procedure	66
5.3	Scatter collection angle	69
5.4	Bead scatter	71
5.5	Biological cell scatter	75
5.6	Recommendations	80
6	Customised flow control system	81
6.1	Materials and cost	81
6.2	Setup and procedure	83
6.3	Pressure to flow speed calibrations	88
6.3.1	Spherical volume method	89
6.3.2	Pendant drop method	90
6.3.3	Results	94
6.4	Hydrodynamic focusing	97
6.5	Integration of a solenoid valve for sorting	101
6.5.1	Experimental detection of cell sorting response time	102
6.5.2	Experimental fluorescence triggered sorting	105
7	Conclusions	108
7.1	Summary	108
7.2	Ongoing Work and Future Directions	111
7.2.1	Glass to PDMS chip	111
7.2.2	Wide-angle Cytometer	113
7.2.3	Other suggestions	115
	References	118
	Appendices	127
A.1	Failed Chip Designs	127

A.1.1	Previous Label-free Glass Chip Design	127
A.1.2	Full glass chip	128
A.1.3	PMMA chip	129
A.2	Mie Code Modifications	132
A.3	Scatter intensity	134
A.3.1	Determining scatter intensity with Mie calculations	136
A.3.2	Experimental scatter intensity	137
A.4	Raw data for pressure to flow speed calibrations	141
A.5	Raw data for hydrodynamic focused ratio to a ratio of pressures	144
A.6	LabVIEW code for fluorescent bead sorting	145

List of Tables

2.1	Properties of organelles within a biological cell [46, 47, 48]	19
3.1	Pressure driven flow system characteristics	36
4.1	Comparison of the optical properties [79]	43
4.2	Roughness of Silicon Master	60
5.1	Cell characteristics	63
6.1	Materials & costs for a pressure driven pump	82
6.2	Materials & costs for a cell sorting side-flow pump	82
6.3	Raw data for pressure to flow calibrations	94
6.4	Response Times of Various Solenoid Valves	104
7.1	Software settings used for Intensity measurements	138
7.2	Raw data for pressure to flow speed calculations in a 200 μm wide channel, see Section 6.3.	142
7.3	Raw data for pressure to flow speed calculations in a 60 μm wide channel, see Section 6.3.	143
7.4	Raw data for Hydrodynamic focused ratio of sheath to sample as a function of increasing flow ratios for different main flow pressures, see Section 6.4.	144

List of Figures

1.1	Cell potency chart reproduced from [1]	4
2.1	Fluorescently labelled cell, adapted from [35]	11
2.2	Information contained in angular light scattering, adapted from [20, 33].	13
2.3	Light scattering geometry for a single scatterer centred at the origin. The incident wave propagates along the $+z$ direction and the scattered wave has a polar angle of θ , and an azimuthal angle of ϕ . [39]	14
2.4	Illustration of an animal cell showing some organelles [45].	18
2.5	Experimental 2D scatter pattern of (a) Sparse distribution of blobs from a human Raji cell that has mitochondria (b) Light and dark bands from a yeast cell that does not have mitochondria [21]	20
2.6	Drawing and micrograph of a mitochondria [49]	21
2.7	(a) Human Raji cell model with 300 randomly distributed mitochondria, nucleus, and cytoplasm (b) corresponding 2D FDTD simulated scatter pattern [21]	21
2.8	Comparisons between the experimental and simulated 2D light scatter patterns from Jurkat and CD34+ cells; (a) Experimental scatter from a Jurkat cell; (b) Experimental scatter from a CD34+ cell; (c) and (e) Simulated Jurkat model and corresponding scatter; (d) and (f) Simulated CD34+ model and corresponding scatter [26]	22
2.9	2D scatter patterns displaying the ability to distinguish between different stages of maturities of the haemopoetic cell. (a) (d) (g) experimental, simulated model, simulated scatter for a platelet; (b) (e) (h) experimental, simulated model, simulated scatter for a myeloid precursor cell; (c) (f) (i) experimental, simulated model, simulated scatter for a CD34+ cord blood cell [27]	23
3.1	Dimensionless velocity profile in a rectangular channel as a result of pressure-driven flow. [58]	28

3.2	Hydrodynamic focusing in a microfluidics chip (a) Two inlets can be used to merge sheath fluid and sample fluid (b) Two side channels introduce sheath fluid and cells are focused two-dimensionally in the centre of the stream (c) One sheath channel can also be used to focus cells to a wall. [57]	29
3.3	Schematic of the top view of a symmetric 2D hydrodynamic focusing in a square channel. [59]	30
3.4	Dimensionless velocity profile when the viscosity of sheath fluid and sample fluid ratio is varied. (a) $\beta = 0.5$ (b) $\beta = 1$ (c) $\beta = 2$ [58] . . .	31
3.5	Focusing sample to sheath width ratio as a function of increasing flow ratios for a sheath channel that is 90° from the main channel, where f is the focusing ratio of focusing width to channel width, and r is the volumetric flow ratio of sheath volume to sample volume[59].	32
3.6	Focusing fraction as a function of distance from the junction for $\kappa = 6$ [59]	32
3.7	Mass fraction distribution of the focused fluid in the channel cross-section calculated when $\kappa = 20$ [60]	33
3.8	Deformation of a spherical cell when exposed to laminar shear stress. [62]	34
3.9	Sorting of cells when (a) side flow is turned 'OFF' (b) side flow is turned 'ON'	35
3.10	Schematic for a pressure generated pump, Fluigent MFCS-FLEX system. [74]	38
4.1	Transmission spectra taken at normal incidence of the plastic materials. Top panel: (A) 0.25 mm, (B) 3.0 mm, and (C) 5.0 mm PMMA. Bottom panel: (D) Borofloat, (E) COC, (F) 0.25 mm, and (G) 2.0 mm PC, (H) PDMS. [76]	42
4.2	Scattering due to surface roughness and internal impurities such as micro-bubbles or dust particles for (i) PDMS to PDMS chip (ii) Borosilicate glass to PDMS chip.	44
4.3	PMMA chip with speckles caused by glue falling in the channel . . .	47
4.4	Flow pattern due to insertion of optical fibres. Cells flowing through the chip do not flow in a straight line.	49
4.5	Cross-sectional view of an integrated waveguide in a PDMS chip formed using high index PDMS ($n=1.43$) as a core and air ($n=1$) and low index PDMS ($n=1.41$) as the cladding.	50
4.6	PDMS chip with integrated waveguides, implementation of hydrodynamic focusing, and fluid sorting channels. Photos taken from [75]. .	53
4.7	Design for the $200 \times 60 \mu\text{m}$ chip	54
4.8	Design for the $300 \times 60 \mu\text{m}$ chip	54
4.9	Fabrication process for Si master	56

4.10	Pouring the low-index PDMS on to the Si master while in a clamp.	57
4.11	Fabrication process for PDMS chip	58
4.12	Plot of roughness on PDMS master using different DRIE processes (a) Cryo in the channel (b) Cryo not in the channel (c) Bosch in the channel (d) Bosch not in the channel	61
5.1	Schematic diagram for optical setup for label-free cytometer.	67
5.2	Photograph of optical setup for label-free cytometer.	68
5.3	Schematic of the laser entering the chip via an integrated waveguide perpendicular to the microfluidic channel, hitting a cell, and scattering upwards into a CCD.	69
5.4	Left: A schematic diagram of the scattered light path in the microscope- based label-free microfluidic cytometer [27]. Right: Light scattering geometry for a single scatterer centred at the origin. The incident wave propagates along the $+z$ direction and the scattered wave has a polar angle of θ , and an azimuthal angle of ϕ . [39]	70
5.5	Comparison of polystyrene bead scatter patterns from (a) original data, diameter $15\ \mu\text{m}$, (b) Su's 2011 paper [27], diameter $9.6\ \mu\text{m}$	72
5.6	Mie solution to scatter from a 532nm incident beam on a $9.6\ \mu\text{m}$ polystyrene bead ($n=1.59$) in PBS ($n=1.334$). For both perpendicular and parallel polarization. Top: For angles 1 to 180° . Bottom: For angles 79 to 101° (22° cone angle), with average polarization showing 9 peaks.	73
5.7	Mie solution to scatter from a 532nm incident beam on a $15\ \mu\text{m}$ polystyrene bead ($n=1.59$) in PBS ($n=1.334$). For both perpendicular and parallel polarization. Top: For angles 1 to 180° . Bottom: For angles 79 to 101° (22° cone angle), with average polarization showing 14 peaks.	74
5.8	Scatter patterns from (a) CD34+ (b) NC-37 (c) HL-60 (d) Kg-1a.	76
5.9	Comparison of CD34+ scatter patterns from (a) original data (b) Su's 2011 paper [26]	77
5.10	Scatter pattern from a healthy myeloid precursor from [27].	78
5.11	Scatter patterns from E. coli DH5 α	79
6.1	Functional block diagram for the pump system and how it interfaces with the optical system.	84
6.2	Schematic for pressure driven pump flask setup	85
6.3	Falling droplet that we assume to be spherical (a) unmodified image (b) modified image showing the extrapolated droplet shape and length measured to determine radius.	90
6.4	Geometry of the pendant drop, where F_g is the gravitation force, F_p is the force due to the pressure in the tube, F_σ is the force due to surface tension.	91
6.5	Estimating β , radius of curvature, from (a) unmodified image (b) mod- ified image showing the extrapolated droplet shape.	92

6.6	Estimating z_0 , length of droplet, from (a) unmodified image (b) modified image showing the extrapolated droplet shape.	93
6.7	Average flow speed of DI water in the main channel of a 200 μm wide PDMS chip as a function of the applied pressure	95
6.8	Average flow speed of DI water in the main channel of a 60 μm wide PDMS chip as a function of the applied pressure, with adapted data from [75]	96
6.9	CCD images of double sheath hydrodynamic focusing in a 200 μm wide channel when main flow pressure is 44 mbar and sheath flow is varied.	98
6.10	Hydrodynamic focusing in a 200 μm wide channel with line plot profile. Main sample flow had a pressure of 44 mbar and sheath flow was set to a pressure of 52 mbar.	99
6.11	Hydrodynamic focused ratio of sheath to sample as a function of increasing flow ratios for different main flow pressures.	99
6.12	Frame by frame images of side flow switching 'off', extracted from a 30 fps video.	102
6.13	Front panel of LabVIEW showing the signal from a fluorescent bead flowing through the detection area.	106
6.14	Superimposed image of a fluorescent bead being sorted. Colours have been inverted for easier viewing.	106
7.1	Scatter pattern of CD34+ cells with a glass to PDMS microfluidic chip with a 300 μm channel width without background subtraction showing lower background noise.	112
7.2	Cross-sectional view of (a) leaky waveguide in a PDMS to glass chip (b) light shining through the waveguide and leaking out through the glass.	112
7.3	Top: Light scattered at 90° (side scatter) propagates to the CCD, while light close to 0° and 180° (forward and back scatter) light is reflected by total internal reflection at the glass-air interface. Bottom: The microfluidic chip is pressed against the CCD eliminating air gaps, creating a wider cone angle and allowing forward and back-scatter to propagate through to the CCD.	114
7.4	Deep etched quartz using the Alcatel Deep Etch system (a) 10 μm lines, 65/ <i>mum</i> depth (b) Pitting on the etched surface [93]	128
7.5	Deep etched Pyrex, 10 μm lines, 26 μm depth, [93]	129
7.6	PMMA base bonded with UV epoxy to 500 μm thick 0211 glass cover (a) bottom view showing channel (b) top view showing input and output connectors.	130
7.7	Mie scatter for a CD34+ cell with 72 mitochondria.	135
7.8	Chameleon CCD calibration curves of gain vs. normalised intensity [100]137	

7.9	Selection in ImageJ of a 60 pixel circular area for the scatter pattern from a CD34+ cell with a histogram of the selection showing intensity data.	139
7.10	Normalised intensity for discrete CD34+ samples.	140
7.11	Back panel of LabVIEW showing the signal collection from the PMT which triggers the solenoid valve after a delay when the signal exceeds a threshold value for a certain amount of time.	145

Glossary of Acronyms

1D :	One-dimensional
2D :	Two-dimensional
3D :	Three-dimensional
AIDs :	Acquired immunodeficiency syndrome
BGS :	Bovine growth serum
CB :	Umbilical cord blood
CBS :	Canadian Blood Service
CCD :	Charge-coupled device
COC :	Cyclic olefin copolymer
DAQ :	Data acquisition device
DI :	De-Ionized
DPSS :	Diode pumped solid state
DRIE :	Deep reactive ion etching
E. coli :	Escherichia coli
EDTA :	Ethylenediaminetetraacetic acid
ESC(s) :	Embryonic stem cell(s)
FACS :	Fluorescence-activated cell sorting
FDTD :	Finite difference time domain
fps :	frames per second
FWHM :	Full width half maximum
G-CSF :	Granulocyte-colony stimulating factor
HAV :	Hepatitis A virus
HBV :	Hepatitis B virus
HCV :	Hepatitis C virus
HDMS :	Hexamethyldisalazane
HIV :	Human immunodeficiency virus
HSC:	Hematopoietic stem cells
HTLV-I/II :	Human T-lymphotropic virus Type I / Type II
ICPRIE :	Inductively coupled plasma
ID :	Inner diameter
IMDM :	Iscoves modified Dulbeccos medium
IPA :	Isopropyl alcohol (also isopropanol or propan-2-ol, 2-propanol)
LB :	Lysogeny broth
LED :	Light-emitting diode
LIF :	Laser induced fluorescence
LOC :	Lab-on-a-chip
LOD :	Limit of detection
LSS :	Light scattering spectroscopy
MACS :	Magnetic activated cell separation
MEM(s) :	Micro-electro-mechanical (system)

MFCS :	Microfluidic control system
MNC :	Mononuclear cells
NA :	Numerical aperture
ND :	Neutral density (filter)
NIR :	Near-infra red
OD :	Outer diameter
OD600 :	Optical density at 600nm
PB :	Peripheral blood
PBS :	Phosphate buffered solution
PC :	Poly carbonate or Lexan
PD :	Photodiode
PDMS :	Poly dimethylsiloxane
PEA :	Poly epoxyacrylate
PFA :	Paraformaldehyde
PMMA :	Poly methyl methacrylate
PMT :	Photomultiplier tube
POC :	Point-of-care
PR :	Photo resist
RBC :	Red blood cells
Re :	Reynolds number
RGB:	Red green blue
RIE :	Reactive ion etching
RMS :	Root mean square
RPMI :	Roswell Park Memorial Institute
SNR :	Signal-to-noise ratio
STS :	Surface Technology Systems
TLA :	Three-letter acronym
UV :	Ultra-violet
VSEL(s) :	Very small embryonic like stem cell(s)
WBC :	White blood cell
WNV :	West Nile virus

Chapter 1

Introduction

Flow cytometry is the process whereby the physical or chemical characteristics of cells (or particles) are measured as they pass by a detector in a single file. The flow cytometer has copious biomedical applications. It has long been used in the medical community to determine particle count and also, in the case of flow sorting, to remove particular types of cells from a general sample. It thus aids doctors and researchers in assessing prognosis, determining treatment, attaining concentrated samples, and identifying certain cell subpopulations. Most often, cells have to be tagged with fluorescent labels in order to enhance the optical contrast. This process is costly, time consuming, and may potentially alter cellular function.

An alternative to labelled cells is to study the light scattering from unadulterated cells, or label-free cells. Light scattering can provide a wealth of information on the size, shape, and morphology of a cell allowing the distinction of one type from another. Cellular light scatter information can be used as an indicator to detect the presence, absence, or progress of conditions that impact the physical structure of cells.

Much research has been done at the University of Alberta to develop a label-free cytometer that is able to distinguish and sort cells using only light scattering

patterns and intensity from individual cells. The design incorporates traditional flow cytometry techniques such as optics, electronics, mechanics, with microfluidics and Lab-on-Chip (LOC) systems to miniaturise and integrate all parts into one device.

This dissertation aims to bring the label-free cytometer closer to commercial realisation. To do so, it explores some of the engineering problems faced in the construction of a label-free flow cytometer and presents solutions for an optimal microfluidics chip design and pump system.

1.1 Niche market for label-free technology

Current commercial bench-top cytometers have been designed to fit the needs of clinical laboratories. However, there is a demand for miniature cytometers for small sample volumes or cytometers that identify only specific cells in a given cell mix. Making the technology label-free would further streamline the process. Furthermore, while the throughput of the label-free cytometer is low in comparison due to the requirements for slower flow to collect scatter, it has the advantages of being low cost and flexible enough to integrate multiple sample steps into one device.

There are two promising applications that are currently being pursued with the label-free cytometer: (i) the sorting of rare Very Small Embryonic-Like stem cells (VSELS) from blood for research and therapies and (ii) the differentiation and identification of prokaryotic from eukaryotic cells for the detection of pathogens in blood.

1.1.1 VSEL stem cells

Stem cells have the potential to treat tissues damaged by genetic defects, injuries, or disease and have thus attracted much attention in the medical research community. When a patient sustains an injury, stem cells for the affected cell type can be trans-

planted into the patient. This in turn regenerates the cell type(s) required to repair the injured tissue. Ideally, stem cells will be isolated from a patient and reintroduced into the same patient for treatment purposes. As the body's immune system will not attack familiar cells, the use of the patients own cells would negate the need for immunosuppressive therapy, allowing the patient to maintain a competent immune system when they need it the most. For example, human hematopoietic stem cells (HSC) are currently being used in clinical transplantation to treat haematological disorders such as leukemias and lymphomas, as well as other cancers. However, being multi-potent, HSC are restricted by lineage and are only able to differentiate into different types of blood cells, reducing the flexibility of its function as shown in Figure 1.1. Pluripotent embryonic stem cells (ESCs), on the other hand, exhibit the potential to differentiate into all the different cell types. Unfortunately, the current methods for isolating embryonic stem cells makes it impossible to isolate and reintroduce them into the same patient.

Recently, pluripotent VSELs have been found in peripheral blood (steady state and mobilised), umbilical cord blood, and bone marrow [2]. Similar to ESCs, these cells are able to differentiate into hematopoietic (blood), mesenchymal (connective tissue, bone, cartilage, muscle, fat), and neural (nervous system) cells. Thus, if isolated in sufficient quantities from adult tissue, VSELs can be used in regenerative medicine to treat damaged tissue without the ethical controversy of ESCs.

Depending on the person, there is about 150 to 300 VSELs per millilitre of peripheral blood [3]. With approximately 5 million cells per micro-litre of human blood [4], a simple calculation sets the concentration of VSELs as 1 in 25 million cells, making it very rare. Unfortunately, centrifugation, the standard procedure to sort red blood cells, white blood cells, and plasma, result in a 60% loss of VSELs [5]. The current method of sorting VSELs is a challenge and requires the use of six to twelve labels

[2, 6, 7] making it costly. Furthermore, in each labelling step, some of the VSEL stem cells are lost, reducing the already low concentration of these rare cells. Thus, there arises a need to find a cost effective system of enriching VSEL concentration that minimises the number of cells lost.

A cost effective way of isolating the cells could lead to new treatments for heart disease, eye disease, diabetes and neurodegenerative disorders, as well as provide insight into the development of many forms of leukaemia. It also can lead to other applications including the discrimination between malignant and non-malignant hematopoietic cells in blood which could help resolve important clinical problems including the early detection of malignant cells circulating in blood and early detection of relapse after remission. Accurate detection of rare malignant cells would be particularly im-

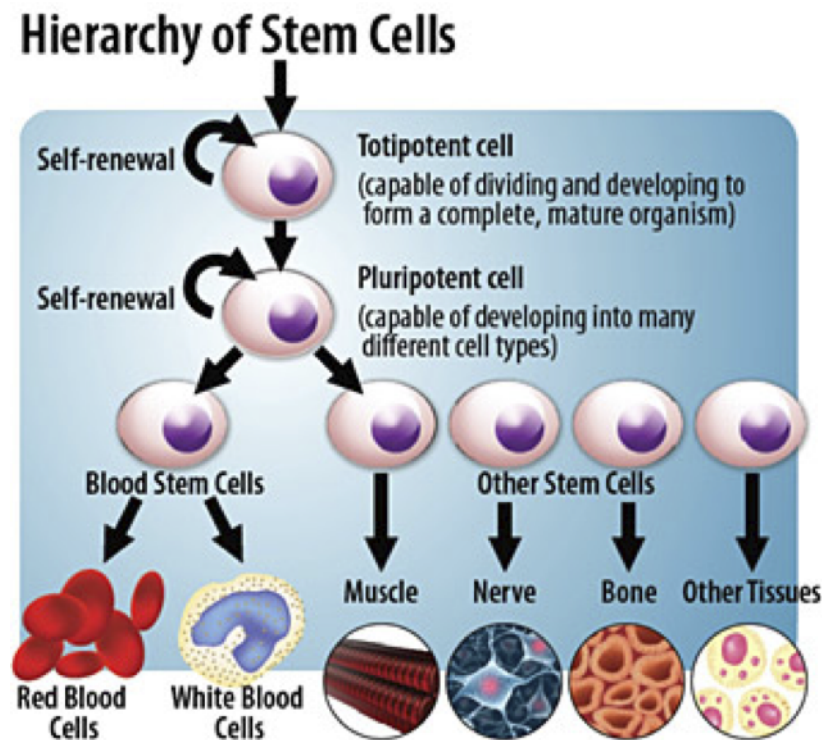


Figure 1.1: Cell potency chart reproduced from [1]

portant and would allow for the development of more effective therapeutic strategies.

Furthermore, since our technique identifies single VSELs, it can be used to determine the concentration of VSELs circulating in peripheral blood. Ratajczak and others reported that VSELs are mobilised into peripheral blood during organ injuries such as heart infarction and stroke [8, 9, 10, 11, 12, 13, 14]. The number of VSEL stem cells as also been observed to increase in peripheral blood of cancer patients [8], thus being a potential early indication of cancer.

1.1.2 Screening of pathogens in blood

Another proposition for the label-free cytometer is the detection of bacterium from human cells in cases of infection. *Escherichia coli* (*E. coli*) is a bacterium that can cause gastroenteritis, urinary tract infections, and neonatal meningitis in humans. Current detection and identification of *E. Coli* from patient samples can take up to two days [15]. Thus, a faster method is required to prevent the spread of infection.

The label-free cytometer would also be useful to detect blood plasma from pathogens at plasma collection centres, where donor screening and sample collection and analysis is required. According to Dr. Leyla Soleymani (personal communication, 24th Aug 2012), our collaborator in McMaster University, the plasma collection procedure is as follows. Prior to collection, the donor is first screened for physiological suitability with a set of haematological tests, such as measuring the concentration of red blood cells, white blood cells and platelets. In addition, the collected plasma must also be free of transmittable disease, requiring sample testing for viral (HIV, HAV, HBs, HCV, HTLV-I/II, WNV, Parvovirus B19), bacterial (syphilis), and parasitic (Chagas disease) disease markers. This sample testing is performed post-collection by shipping samples from each donation centre to outsourced centralised diagnostic

laboratories. This results in additional costs (\$20 per sample contributing to a third of total production cost) and delays of up to two weeks before the collected sample can be released for use. There arises a need for POC rapid, inexpensive, and easy-to-use infectious disease screening methods.

Blood cells have a eukaryotic internal structure with organelles, as discussed in Chapter 2, whereas bacteria have a prokaryotic structure lacking membrane bound organelles i.e. mitochondria. Eukaryotic blood cells (with the exception of platelets) are also much larger than prokaryotic cells. These two main differences should result in weaker light scatter intensity and less complex scatter patterns for the prokaryotic pathogenic cell.

The concentration of pathogen in blood from a healthy person is expected to be low, approximately 1 pathogen cell in 1 ml of blood [16]. The problem of sorting pathogens in blood is very similar to that of sorting VSEL stem cells in blood and thus a similar strategy for complete label free sorting of VSEL stem cells can be used for the sorting of pathogens as well.

1.1.3 Other Applications

Another good example for the application of a label-free cytometer would be the need for a portable POC cytometer in resource-limited countries for the testing of the human immunodeficiency virus (HIV), which results in acquired immunodeficiency syndrome (AIDs), malaria, and tuberculosis. Current cytometers designed for this purpose, such as the BD FACS counter, require prior preparation of the whole blood sample to label the cells of interest. This involves inserting whole blood into a pre-filled cartridge, incubating it for some time, pipetting in buffer solution, before inserting the sample into the cytometer [17]. Although these steps seem trivial in

a laboratory environment, in a resource limited facility where clean running water, reliable electricity, and well-trained technicians are often not available, these steps pose a larger challenge. Supplying and transporting the reagents and buffer solution is also an issue [18]. In such situations, a miniature label-free cytometer would be the perfect match. It would eliminate the need for supplemental ingredients such as reagents and buffer solution, and make complex technical steps such as pipetting and incubation redundant. This speeds up the testing and makes the label-free cytometer a truly stand-alone POC instrument with minimal supplies required for function.

Another advantage of label-free cytometry over conventional FACS is that we are able to preserve cell viability by not fixing the cell with fluorescent labels. This enables scientists to study how the same batch of cells evolves over time. As Fang [19] insightfully states, optical techniques involving visible and near-infrared light have become popular due to their relatively benign effect on living cells. Some optical techniques (such as the light scattering technique we use) can allow researchers to follow living cells in their own environment and observe their dynamics to determine cell function. Fang believes that such techniques will dramatically advance the understanding of diseases and lead to earlier diagnosis [19].

1.2 Outline

This dissertation details some of problems faced in the device design of a label-free cytometer and their solutions. The design improvements focus on two main aspects (i) optimisation of the microfluidic chip design (ii) the integration of a customised flow control system with cell sorting.

Chapter 2 presents background material on current cytometric techniques and light scattering spectroscopy. Mie Theory, a mathematical model for calculating light

scatter, is also briefly discussed and this is used to explain the importance of organelles in a cell. Key findings of previous work are summarised in the process.

A background of microfluidics as it pertains to flow cytometry is set forth in Chapter 3. Effects unique to miniaturised flow systems are explored together with practical solutions. This ties into a discussion on suitable pump systems for microfluidic systems and their availability.

The design and fabrication improvements made to the microfluidic chip in the label-free cytometer can be found in Chapter 4. This chapter touches on past designs, as well as other chip materials that were considered before settling on a $200\mu\text{m}$ wide channel on a PDMS chip. Chapter 5 follows with cell scattering experiments performed using the chip presented at the end of Chapter 4. These were done to evaluate the chip design and to determine if light scatter patterns and intensity can indeed be collected with this setup.

Moving on to the second design improvement, Chapter 6 presents the prototype of a low-cost pressure driven pump with a cell-sorting feature. The pump is calibrated for the present system with suggestions for improvement. Chapter 7 closes this dissertation with a set of concluding remarks and a look at ongoing work and future directions.

Chapter 2

Background on label-free cell imaging

Cytometers function as a characterisation tool for biological cells and are widely used in clinical laboratories for cell identification and sorting. Current methods stain cells with fluorescent antigens or fluorescent labels for detection in a cytometer [20]. However, cell staining is laborious and time consuming. Therefore, there arises a need for a physically non-invasive cytometer where unadulterated living cells can be studied.

One such alternative to conventional flow cytometry is to characterise biological cells based on two-dimensional (2D) scattered light patterns from label-free cells as shown in [23, 27, 21, 25, 26, 24, 22]. This approach yields detailed information on the cells size, shape, and most importantly, spatial distributions of organelles within a biological cell [28], which can potentially be used for the diagnosis of cancers and other diseases [29, 30, 31, 32].

To gather more information about biological cells without labelling, we want to examine its intracellular structures (organelles) and the distribution of these organelles

within the cell. Unfortunately, such organelles are often smaller than the diffraction limit and cannot be imaged directly using visible light (420 to 700 nm) in optical microscopy. But when illuminated with light in the visible range, the cell scatters light in meaningful spatial patterns that carry information about the cell size, shape, refraction index, density, and internal morphology [33, 21, 26]. The spatial distribution of light is significant and the intensity of detected signals are angularly dependant. Looking at different angular ranges provides particular types of information about the cell. All this can be used to characterise and differentiate between different cell lines in a mixed sample and also to differentiate between different cell states such as apoptosis, mitosis, and more. This method, called Light Scattering Spectroscopy (LSS), will be discussed in detail, followed by the importance of organelles to create meaningful scatter patterns. But before we get to this, current cytometric technologies and the basic components of a flow cytometer are briefly explored.

2.1 Current cytometric technologies and their basic components

By definition, a cytometer is a device that analyses a biological cell by its physical and/or chemical characteristics. Conventional cytometers often integrate this with flow cytometry and flow sorting where measurements are made as a single stream of cells suspended in fluid is passed through the optical instrument; then, cells that fall within a set range of variables set by the user are diverted from the main population and sorted. Typically, cell identification and sorting are enabled through the introduction of fluorescent labels. In fluorescent-activated cell sorting (FACS), a laser beam is directed at part of the flow, exciting the fluorescent-label attached to the cell

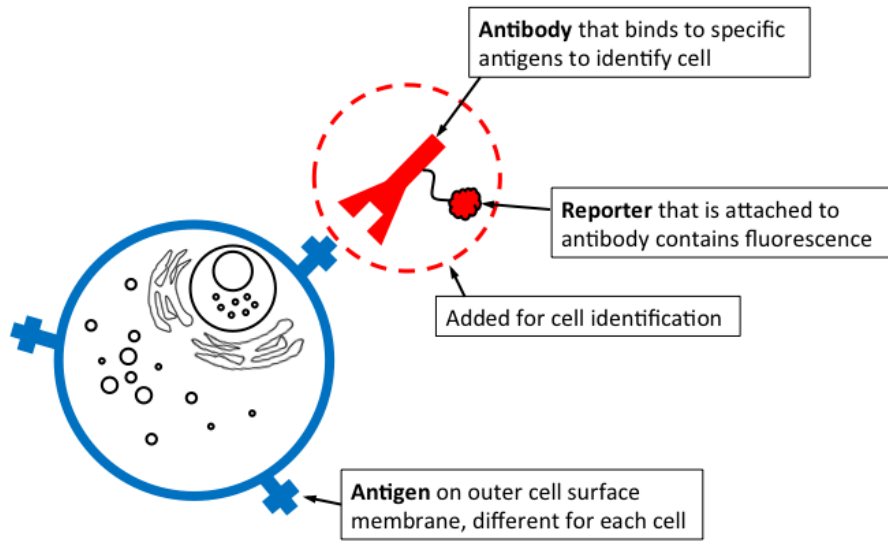


Figure 2.1: Fluorescently labelled cell, adapted from [35]

and causing it to emit light at a different wavelength. In some cases, the intensity of light from small-angle forward scatter at a cone angle of 5° and side scatter at a cone angle of 10° is collected and used in characterisation analysis. After this, the cells are immediately sorted into different bins so individual cells with selected characteristics can be isolated for further study.

Thus, a generic flow cytometer can be broken down into three main parts (i) injection, (ii) detection, and (iii) sorting. Injection of cells and sorting of desired cell from a batch essentially boils down to the microfluidics of the device; how the cell flows in relation to the channel. This is an engineering challenge that can be solved once the method of detection is settled upon and will be discussed in more detail in Chapter 3.

Most important is the the detection region of a cytometer. Here, cells are detected and analysed most popularly via labelled means such as fluorescence, or unlabelled means such as electrical impedance, light absorption, and light scattering.

In labelling, specific antibodies, each carrying a fluorescence reporter, bind to matching antigens located on the outer surface of the cell membrane as shown in Figure 2.1. Since different type of cells have different antigens and corresponding antibodies, the detected fluorescence is used to characterise the cells [35].

According to Cheung, although some leukocytes can be sorted without the use of labels by using just forward and side scatter information about their size and granularity, fluorescent labelling is still preferred due to its efficiency and reliability [36]. However, the use of such cell markers, or fluorescent labels, inherently alters the makeup of the cell [23]. The labelling process is also time-consuming and expensive, proving unfavourable for point-of-care (POC) situations where speed, simplicity, and low cost are important.

Therefore, this thesis builds upon previous work done on the detection of cells via the unlabelled means of light scattering.

2.2 Light scattering spectroscopy

LSS is a well-known optical technique that takes advantage of Mie scattering theory, described in more detail in Section 2.3. With LSS, we are able to obtain information about internal cell structures that are much smaller than the diffraction limit [23, 33, 26, 37, 27, 38]. The different biochemical makeup of organelles within a cell creates a spatially varying index of refraction, which influences the amplitude of scattered light. This means that a larger difference in index of refraction creates increased scatter.

On the other hand, the relative size of the cell and its organelles in relation to the wavelength of light, affects the angular distribution of scatter. To break it down, the forward scatter in the small angle region of 0.2° to 2.0° is primarily dependent on the cell's size and overall refractive index, whereas forward scatter at larger angles of

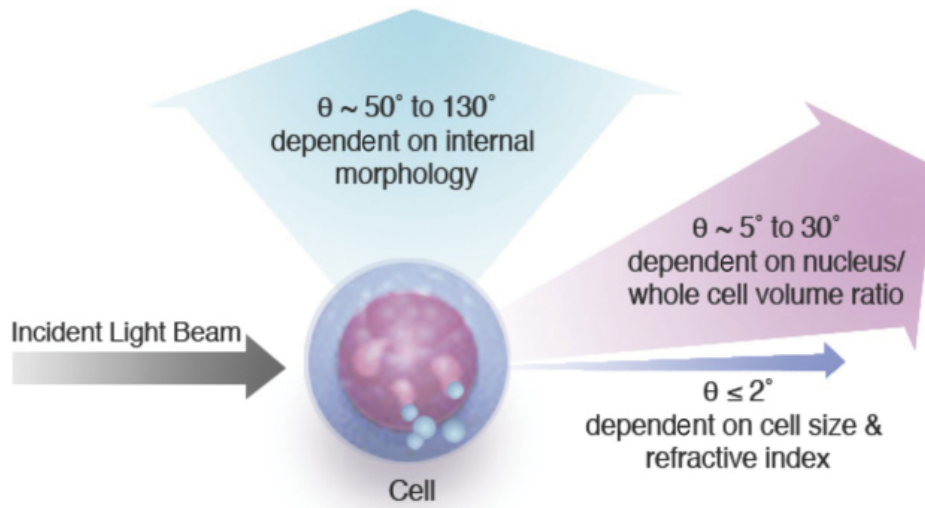


Figure 2.2: Information contained in angular light scattering, adapted from [20, 33].

5.0° to 30° is largely dependent on the fractional volume of the nucleus with respect to the rest of the cell. Information on the cells internal morphology is contained in the side scatter data between 50° to 130° . [20, 33] This is shown in Figure 2.2.

This method is currently used in biomedical science for cell analysis and sorting but is mostly concentrated on collecting one-dimensional (1D) scattered light intensity of forward and side scatter for cell size detection [20]. The information that can be gathered from 1D scatter is limited since cell morphology and orientation can cause dramatic variations in the intensity of the scatter. Compared with 1D scatter spectra, 2D scatter patterns contain more information about a three-dimensional (3D) biological cell. By imaging the scatter with a charge-coupled device (CCD) into a 2D picture, small morphological changes within the cell can be detected. This ability to obtain and analyse 2D scattered light over a wide angular range can therefore enable us to characterise cells by their internal morphology. [23, 24]

2.3 Mie scattering theory

Mie theory is used to solve Maxwell's electromagnetic equations in the particular instance where an incident plane wave scatters off an isotropic homogeneous sphere. The formal solution takes the form of an infinite series. Mie theory applies when the scatterer is of a similar size to the wavelength of the incident beam and its scatter is mostly independent of wavelength. For scatterers smaller than the wavelength, they fall within the Rayleigh scattering regime instead.

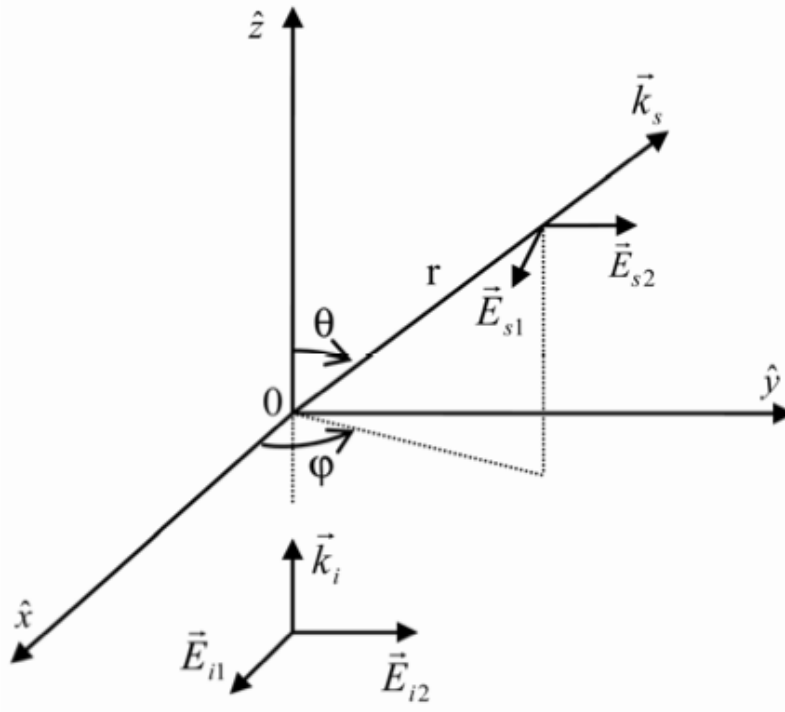


Figure 2.3: Light scattering geometry for a single scatterer centred at the origin. The incident wave propagates along the $+z$ direction and the scattered wave has a polar angle of θ , and an azimuthal angle of ϕ . [39]

The light scattering geometry is shown in Figure 2.3 with \vec{k}_i and \vec{k}_s defining the incident and scattering plane. Polarization of the incident beam is maintained in the

scattered beams. The expression for the scattered electric field from a homogeneous sphere can be written in matrix form as

$$\begin{pmatrix} \vec{E}_{||s} \\ \vec{E}_{\perp s} \end{pmatrix} = \frac{e^{ik(r-z)}}{-ikr} \begin{bmatrix} S_2 & 0 \\ 0 & S_1 \end{bmatrix} \begin{pmatrix} \vec{E}_{||i} \\ \vec{E}_{\perp i} \end{pmatrix}. \quad (2.1)$$

The scattered polarised intensity are $i_1 = |S_1|^2$ for perpendicular polarisation, and $i_2 = |S_2|^2$ for parallel polarisation. In order to find the scatter matrix elements S_1 and S_2 , the scattering cross sections, we begin with the wave equation for a time-harmonic electromagnetic field (\vec{E}, \vec{H}) propagating in a linear, isotropic homogeneous medium,

$$\nabla^2 \vec{E} + k^2 \vec{E} = 0 \quad (2.2)$$

$$\nabla^2 \vec{H} + k^2 \vec{H} = 0. \quad (2.3)$$

The solution is found using separation of variables, then making use of the expansion of a plane wave solution into vector spherical harmonics. Next, we apply the boundary condition, ensuring that the tangential components are continuous at the boundary of the cell. The scattering matrix elements, S_1 and S_2 , can now be written as

$$S_1 = \sum_{n=1}^{\infty} \frac{2n+1}{n(n+1)} (a_n \pi_n + b_n \tau_n) \quad (2.4)$$

$$S_2 = \sum_{n=1}^{\infty} \frac{2n+1}{n(n+1)} (a_n \tau_n + b_n \pi_n), \quad (2.5)$$

where the scattering coefficients are:

$$a_n = \frac{m\Psi_n(mx)\Psi'_n(x) - \Psi_n(x)\Psi'_n(mx)}{m\Psi_n(mx)\xi'_n(x) - \xi_n(x)\Psi'_n(mx)} \quad (2.6)$$

$$b_n = \frac{\Psi_n(mx)\Psi'_n(x) - m\Psi_n(x)\Psi'_n(mx)}{\Psi_n(mx)\xi'_n(x) - m\xi_n(x)\Psi'_n(mx)}. \quad (2.7)$$

Here, x is the size parameter and m is the relative refractive index ($x = ka = \frac{2\pi Na}{\lambda}$, $m = k_1/k = N_1/N$, and N_1 and N are the refractive indices of scatterer and surrounding medium, respectively). λ corresponds to the vacuum wavelength of the incident beam. The Riccati-Bessel functions were used to simplify the expression:

$$\Psi(\rho) = \rho j_n(\rho) \quad (2.8)$$

$$\xi(\rho) = \rho h_n^{(1)}(\rho) . \quad (2.9)$$

Here, j_n is the n th-order Bessel function of the first kind, and $h_n^{(1)}$ is the n th-order Hankel function of the first kind. Finally, π_n and τ_n are angle-dependent functions:

$$\pi_n = \frac{P_n^1(\cos \theta)}{\sin \theta} \quad (2.10)$$

$$\tau_n = \frac{dP_n^1(\cos \theta)}{d\theta} , \quad (2.11)$$

where P_n^1 are n th-order Legendre polynomials of the first kind. The solution for the electric field is thus completely defined and can be calculated given a set of input parameters.

These Mie derivations are paraphrased from Su's thesis [39], which was based upon initial work by Bohren and Huffman [40] and Grandy [41]. For a full and complete formulation of this theory, please refer to the classic texts on light scattering by Hulst [42], or Bohren and Huffman [40]. There are also many publicly available codes, in a variety of programming languages, available to implement the Mie scattering algorithm for given inputs. The C version of this code will be used in Chapter 5 and in-depth information about the code used can be found in Appendix A.2.

As the size of organelles in cells are similar to that of visible light, Mie theory has been used to approximate light scattering from biological cells [43, 44]. The solutions

attained are merely approximations though, as the scatterers (cells or organelles) are assumed to be spherical and homogeneous. As Mie theory involves strict boundary conditions, it is unable to cope with the non-uniform shapes and complex inner structures of real biological cells. Moreover, Mie theory cannot account for the contribution of several different types of organelles in a cell, each with a specific orientation, location, and density.

For simulations that are true to the structure of a real biological cell, more complex models have been used. One such example is the finite-difference time-domain (FDTD) method that is far more powerful, and described in papers by Su [21, 24, 25, 39]. The FDTD method is also used in many of the figures in the next section.

2.4 Importance of organelles

Although 2D light scattering enables us to determine the internal morphology of the cell, this is also a limitation for the label-free cytometer. Unlike FACS, which relies on antigens on the cells surface to characterise cells, this label-free technique is limited to cells that have different internal morphologies, such as the distributions of organelles, or the dominance of one organelle over the entire cell volume. Some significant organelles in an animal cells is illustrated in Figure 2.4.

By collecting scatter at large side angles, Su et al. [21, 24], has found that micro-scale cellular components, such as the nucleus and cytoplasm, contribute to band structures in the 2D scatter pattern seen in Figure 2.5(b). Conversely, smaller sub-micron organelles, such as the mitochondria, peroxisomes, lysosomes, microtubules, etc., are similar in size to the wavelength of the incident beam (532nm) and dominate the scatter, generating 2D blobs of light spots in a darker background as seen in

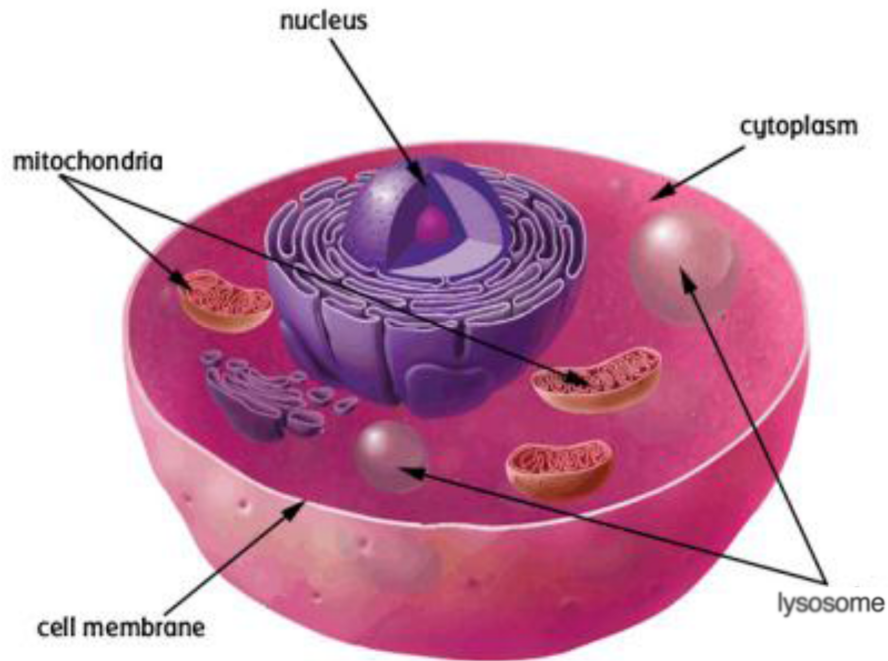


Figure 2.4: Illustration of an animal cell showing some organelles [45].

Figure 2.5(a). Since mitochondria make up a larger fractional volume than other sub-micron organelles and also has the largest refractive index (as shown in Table 2.1), it is safe to assume that mitochondria (or the lack of) is the main contributor to the 2D scatter pattern shown in Figure 2.5 [46, 47, 48].

Furthermore, looking at the internal structure of mitochondria, it is composed of many folded internal lipid membranes called cristae, as shown in Figure 2.6. Firstly the refractive index mismatch between the 9nm thick basic lipid bilayer membrane and the surrounding aqueous medium causes strong scatter [49]. Folding of lipid membranes within the outer membrane presents even more lipid to water interfaces, making them especially strong scatterers of light.

The dominance of mitochondria in scattered light from biological cells have also been simulated by numerically solving Maxwells equations using the FDTD method

Table 2.1: Properties of organelles within a biological cell [46, 47, 48]

Cell Component	Diameter (μm)	Refractive Index	% of Cell By Volume
Cytoplasm	10 - 30	1.38	50 - 80 %
Nucleus	3 - 10	1.39	5 - 10 %
Mitochondria	0.3 - 0.7	1.42	5 - 15 %
Lysosome	0.2 - 0.5	1.3785	1 - 10 % *

* Includes other remaining organelles

based on Yeess algorithm [28]. The cell is modelled as a spherical object with a large spherical nucleus surrounded by smaller spherical mitochondria as shown in Figure 2.7. Su et al. [21] reported that mitochondria dominate the 2D light scatter patterns from human Raji cells and the experimental results were compared with FDTD simulations further supporting the claim.

Being able to detect mitochondria in a cell is significant as it can be used as an intrinsic biological marker for single cells. There are a number of potential clinical applications, namely the detection of mitochondria related conditions such as cancer [29, 30], ageing [31], and Parkinsons and Alzheimers disease [32]. A label-free cytometer would enable the early detection of these diseases and also fast detection of relapse after remission. For example, Yu et al. [30] was able to differentiate between healthy and cancerous colon tissue using 2D scattered light spectra. The cancerous tissue exhibited much greater asymmetry in the azimuthal dependence of the scattered pattern as compared to the healthy tissue. In another study, Gourley [50] has shown that mitochondria tend to cluster close to the nucleus of a normal cell but is randomly distributed in cancerous cells. This was recently tested in a 2D microfluidic cytometer by Su et al.[26], who demonstrated that experimental 2D light scattering

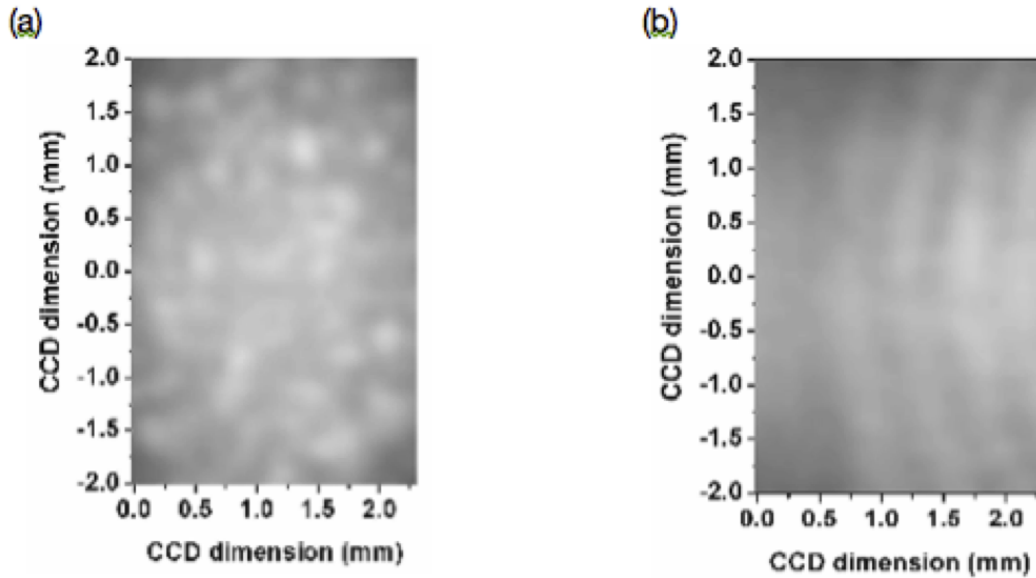


Figure 2.5: Experimental 2D scatter pattern of (a) Sparse distribution of blobs from a human Raji cell that has mitochondria (b) Light and dark bands from a yeast cell that does not have mitochondria [21]

from malignant lymphoid cells (Jurkat cell line) and normal hematopoietic stem cells (cord blood CD34+ cells) corresponded with FDTD simulations, where the mitochondria in Jurkat cells were randomly distributed but aggregated in a CD34+ cell. This observation was then confirmed by conventional confocal fluorescence microscopy. Results are shown in Figure 2.8.

Furthermore, this label-free technique has been used to study the mitochondria for hematopoietic stem cells at different stages of differentiation, see Figure 2.9. This is significant as hematopoietic stem cells have the potential to mature into blood cells of all lineages (erythroid, myeloid, lymphoid, etc.) while maintaining their ability to self-renew. This gives the patient's body the flexibility to replenish required cells as needed. Therefore, in the study of stem cells, a label-free technique is preferred so as not to disturb their biological functions. [27]

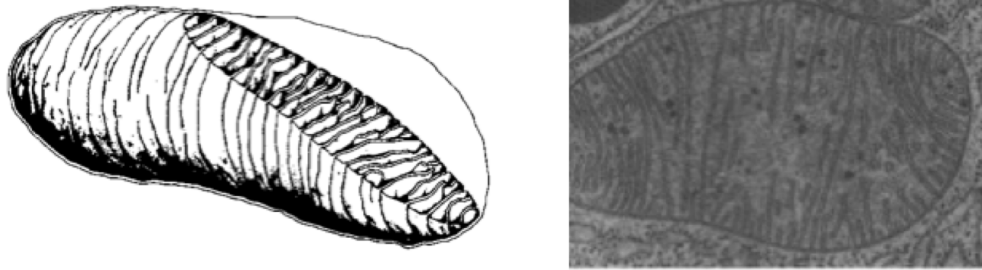


Figure 2.6: Drawing and micrograph of a mitochondria [49]

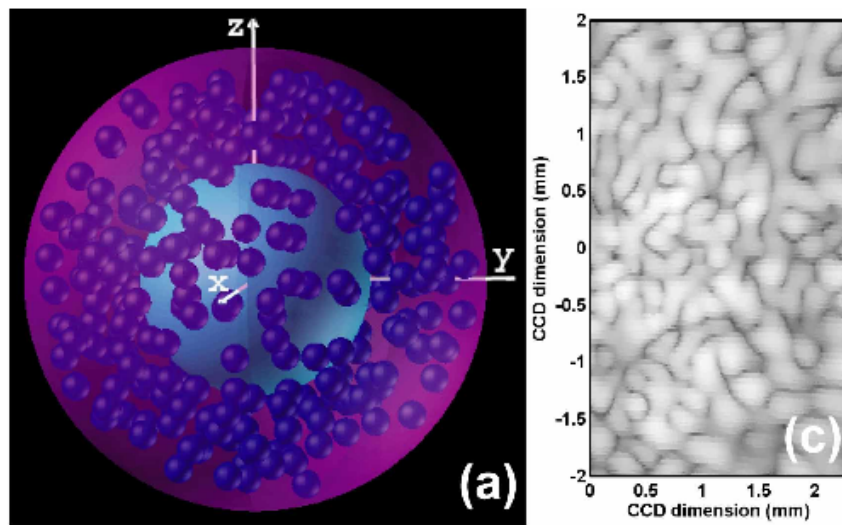


Figure 2.7: (a) Human Raji cell model with 300 randomly distributed mitochondria, nucleus, and cytoplasm (b) corresponding 2D FDTD simulated scatter pattern [21]

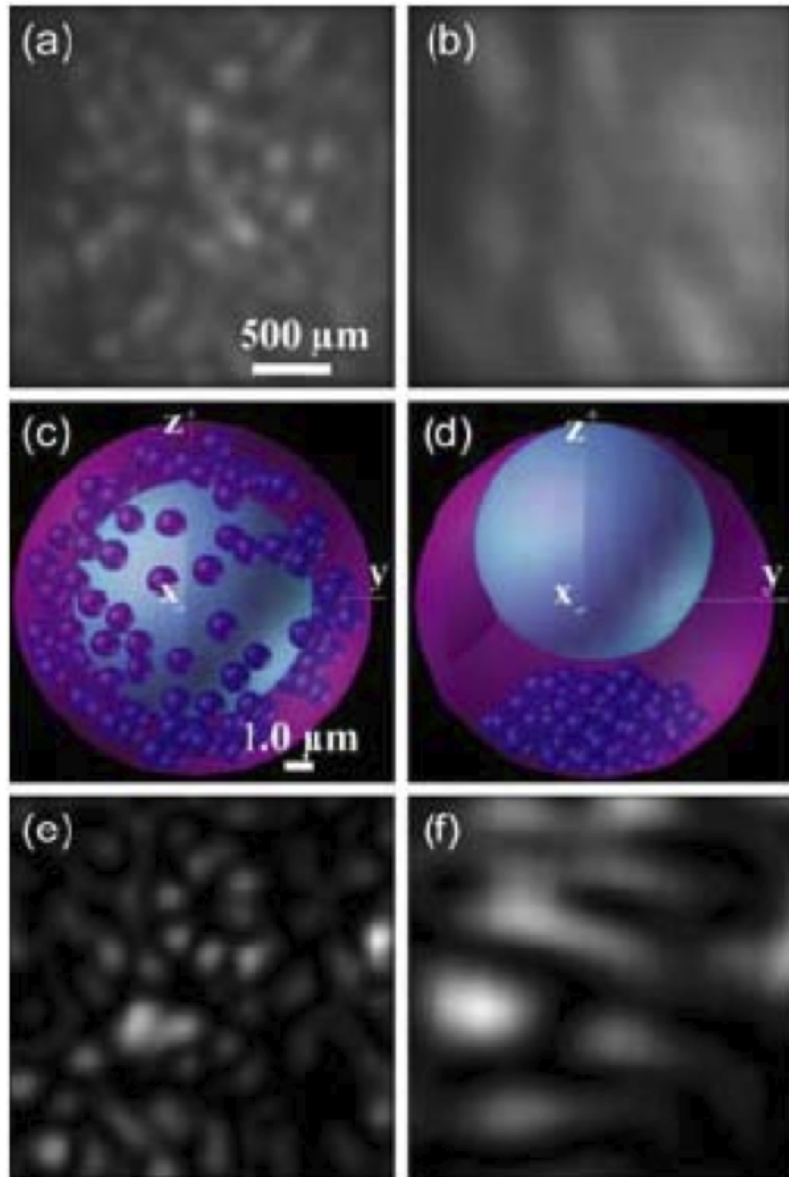


Figure 2.8: Comparisons between the experimental and simulated 2D light scatter patterns from Jurkat and CD34+ cells; (a) Experimental scatter from a Jurkat cell; (b) Experimental scatter from a CD34+ cell; (c) and (e) Simulated Jurkat model and corresponding scatter; (d) and (f) Simulated CD34+ model and corresponding scatter [26]

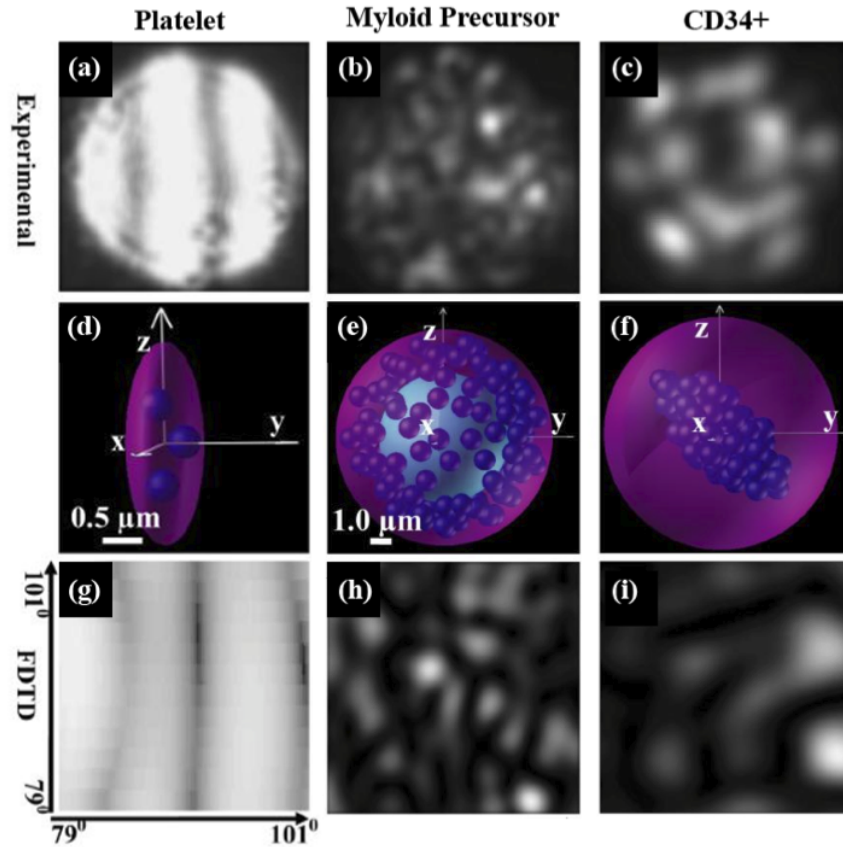


Figure 2.9: 2D scatter patterns displaying the ability to distinguish between different stages of maturities of the haemopoetic cell. (a) (d) (g) experimental, simulated model, simulated scatter for a platelet; (b) (e) (h) experimental, simulated model, simulated scatter for a myeloid precursor cell; (c) (f) (i) experimental, simulated model, simulated scatter for a CD34+ cord blood cell [27]

Chapter 3

Microfluidics background

Microfluidics is a growing field with many applications in sensors, consumer electronics, clinical diagnosis equipment, surgical tools, and microbiology applications. These microfluidic chips can be designed to handle off-chip fluidics in the form of micro-electro-mechanical (MEMs) liquid pumps or gas valves, or are also capable of flowing minute volumes of liquid directly on-chip. There is also the added possibility of integrating sensing capabilities and an entire assay operation, such as sample preparation, detection, diagnosis, and sorting, all on one chip, essentially creating a self-contained lab-on-chip (LOC) package.

The field is defined concisely by Herold et al. as fluid flow in small channels (e.g. sub-millimetre diameter) with flow control devices (e.g. channels, pumps, mixers, and valves.) [51]. At the most basic, it consists of a simple channel etched out of the bottom layer with a top layer to keep the fluid in the channel. Two inlets on either end of the channel allow flow control devices to interact with the fluid and create a flow through the chip. More complex microfluidic designs consist of multiple intersecting channels for sorting, directing flow, mixing and more. Additional access inlets can also be inserted for sensing capabilities, such as electrical contacts or for

guiding light into the channel for analysis of the fluids optical properties.

Microfluidics integrated with optics enables the integration of cell injection and sorting with cell detection, and has great potential in flow cytometry. As compared to conventional flow cytometers, these microfluidic flow cytometers require only small sample volumes due to their small cross-sectional areas that are often significantly less than a square millimetre [27]. Furthermore, since the same micro and nano-fabrication techniques that are used to manufacture microelectronics are also used to create microfluidic structures, fabrication methods are well established and scalable. Depending on the cost of the material, processing and yield times, a microfluidic chip has the potential to be disposable, perfect for use with biological cells where cross contamination of samples is of great concern. A microfluidics chip is also more spatially economical as components for characterisation and sorting can be integrated into the same chip, with no need for bulky connectors. This coupled with recent developments of LOC techniques can push microfluidic cytometers to become the next generation of commercially available diagnostic tools [27].

However, with the miniturisation that microfluidics brings, there are unique aspects that affect fluid flow that are usually considered negligible in macrofluidics. In this section, I will explain laminar flow in a microfluidic channel, and pressure driven flow and the concerns that it brings (velocity profile, hydrodynamic focusing, shear force). I will then explore current solutions on the market for types of flow control systems (pumps) available for microfluidic systems as well as their applicability for cell sorting applications.

3.1 Laminar flow

Large surface-area-to-volume ratios of microfluidic channels result in systems that are dominated by fluid interactions with the surface of the channel. These viscous interactions can hinder fluid flow and cause large pressure drops for even modest flow velocities. Due to these surface forces, turbulent flow can be ignored and most flows in a microfluidic channel are assumed to be laminar. This means that the fluid moves along organised layers (lamina) without mixing and maintain their relationship to adjacent layers throughout the flow.

The type of flow in a channel can be determined by the channels Reynolds number (Re), the ratio of inertial to viscous forces:

$$Re = \frac{\rho V D}{\mu}, \quad (3.1)$$

where ρ is the fluid density, V is velocity, D is the characteristic length, and μ is the dynamic viscosity of the fluid [51].

Characteristic length is considered the diameter of the circular tube. But in microfluidics where channels usually have trapezoidal cross sections, the characteristic length or hydraulic diameter of a non-circular cross section is

$$D_h = \frac{4A}{P_w}, \quad (3.2)$$

where A is the cross sectional area of the channel and P_w is the perimeter of the channel, also known as the wetted perimeter [51].

For Re between 1 and 2300, flow is considered laminar. Above that, turbulent flows have to be taken into account and below that, it falls into the regime of Stokes flow, where fluid velocities are very slow, viscosities are very large, turbulent flow is

negligible, and flow can be modelled with Stoke's Law.

3.2 Pressure-driven flow

Pressure-driven flow is of primary interest in this thesis. It is also the simplest to implement by connecting a pump or a syringe to a channel inlet, and works regardless of channel design. One other method of flow is electro-osmotic flow, where the sample fluid is moved through the channel due to an externally applied electric field. This field induces the movement of ions in the passing sample fluid from the surface charges on the channel walls and due to the lack of resistance, the rest of the fluid in the middle of the channel is also moved along. However, electroosmotic flow requires specific channel surface properties [52, 53] that sometimes restricts its use in biomedical applications. Electro-osmotic flow is suppressed by the coatings often applied to channel walls to prevent the adhesion of cells, as the net electrical charge of the channel surface is reduced [54]. Furthermore, a strong electric field is undesirable for use with biological cells, especially if they are still viable, as it may affect the cell's function and properties. Chang et al. and McCain et al. also state that small or modest electrical fields encourage the transport of ionic species across the cell membrane while high fields can completely rupture the cell [55, 56].

In pressure-driven flow, as its name suggests, a pump or syringe creates an increase of pressure at the inlet and this pressure difference drives the fluid through the channel. This pressure drop can be described by the fluidic equivalent of Ohm's law:

$$\Delta P = RQ , \tag{3.3}$$

where P is the pressure, R is the flow resistance, and Q is the volumetric flowrate[51].

Fluid tends to cling to channel walls and maximum velocity occurs at the centre of the channel with velocity along the walls essentially being zero due to friction between the walls and the fluid. This results in a parabolic velocity profile for a circular channel and something similar for a rectangular or square channel as shown in Figure 3.1 [57, 51].

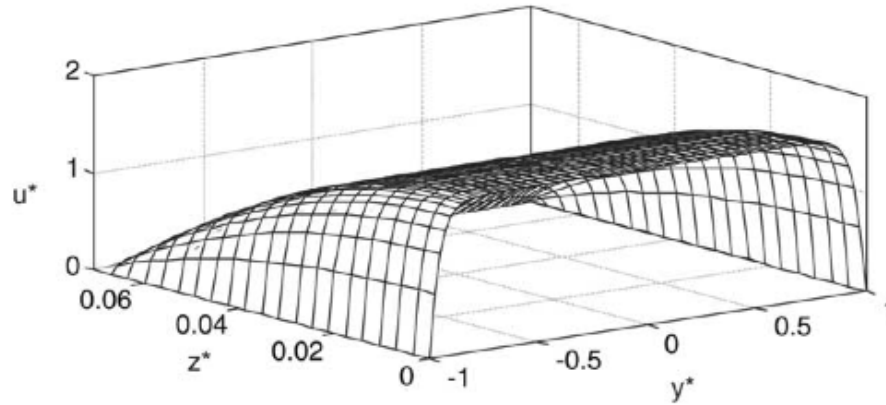


Figure 3.1: Dimensionless velocity profile in a rectangular channel as a result of pressure-driven flow.[58]

Unfortunately, this means that cells travelling in the flow will have different velocities depending on their position in the flow channel. But this problem can be mitigated through the use of hydrodynamic focusing, which limits a cell to travel in the central region of a microfluidic channel, and uses this non-uniform velocity profile to our advantage.

3.2.1 Hydrodynamic focusing

In hydrodynamic focusing, sheath flow is introduced around the main flow carrying the suspended cells as seen in Figure 3.2. Stream width is reduced and the cells are confined to the middle of the channel making its position predictable and its speed

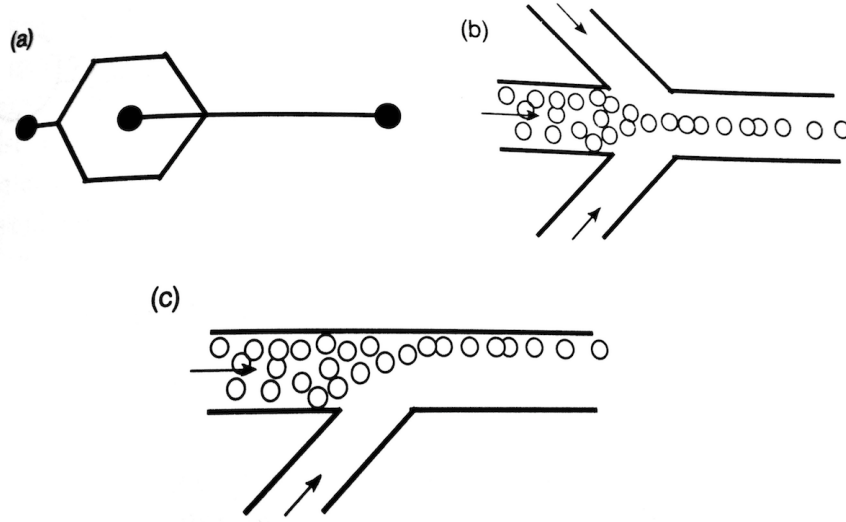


Figure 3.2: Hydrodynamic focusing in a microfluidics chip (a) Two inlets can be used to merge sheath fluid and sample fluid (b) Two side channels introduce sheath fluid and cells are focused two-dimensionally in the centre of the stream (c) One sheath channel can also be used to focus cells to a wall. [57]

more constant.

For the flat channel shown in Figure 3.3, the position of the interface between the sample and sheath flow can be estimated as:

$$w_f = \frac{1}{1 + 2\beta\kappa}, \quad (3.4)$$

where $\beta = \nu_s/\nu_i$, the ratio of sheath fluid viscosity to sample fluid viscosity, and $\kappa = Q_s/Q_i$, the flow rate ratio of sheath to sample. Hence, both viscosity ratio and flow rate ratio determine the width of the focused stream [58].

By keeping the flow ratio (velocity of sheath flow to that of main flow) constant and varying the viscosity ratio of the two flows, Wu et al. has demonstrated that it is possible to achieve various velocity profiles [58]. As seen in Figure 3.4(a) if the sample flow is more viscous, sample velocity is slower. In Figure 3.4(b) When the viscosities

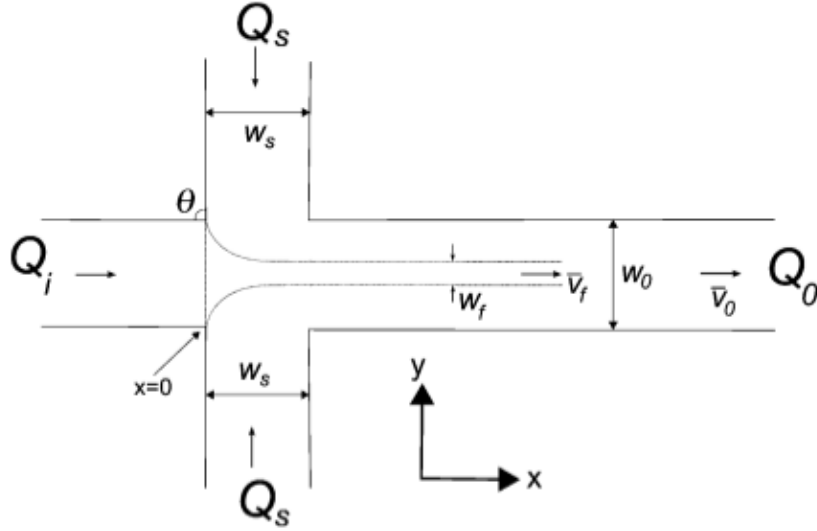


Figure 3.3: Schematic of the top view of a symmetric 2D hydrodynamic focusing in a square channel. [59]

for sample and sheath are the same, the velocity profile is the same as the one shown in Figure 3.2 with no hydrodynamic focusing. If the sheath flows are more viscous, sample flow is faster, Figure 3.4(c). Conversely, keeping the ratio of viscosities, β , constant, Equation 3.4 was verified experimentally by Kunstmann-Olsen et al. [59], results are shown in Figure 3.5.

It is also useful to note that focusing rapidly decreased in width along the width of the channel with a stabilisation effect after 150 to 200 μm shown in Figure 3.6. [59]

Exceptions to Equation 3.4 occur when the Reynolds number is drastically changed even within the laminar flow range. Blonski et al. [60], showed that the Reynolds number for the sample flow should be kept less than 10 with the optimal focusing being $\text{Re} = 4$, as illustrated in Figure 3.7. Anything above $\text{Re} = 0$, destroys the flow focusing mechanism.

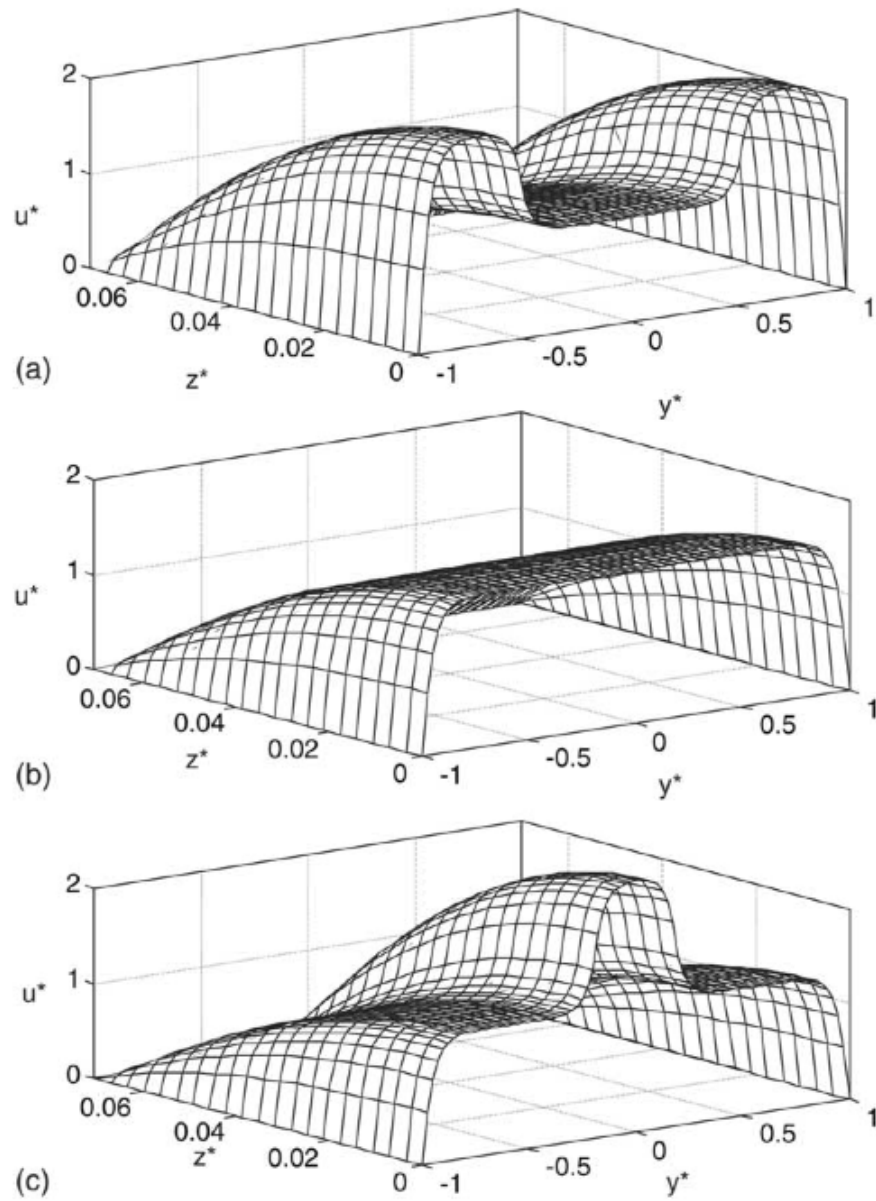


Figure 3.4: Dimensionless velocity profile when the viscosity of sheath fluid and sample fluid ratio is varied. (a) $\beta = 0.5$ (b) $\beta = 1$ (c) $\beta = 2$ [58]

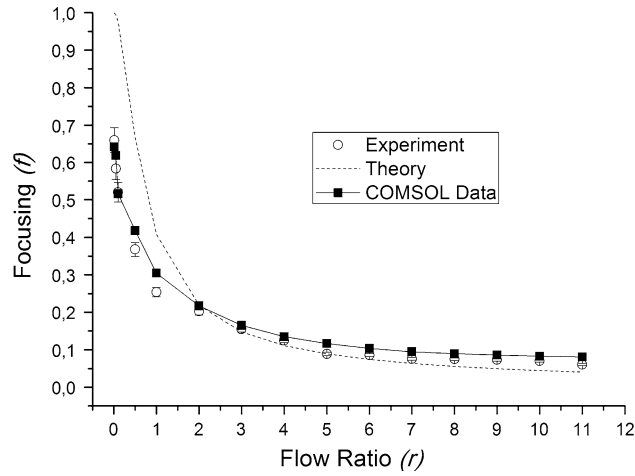


Figure 3.5: Focusing sample to sheath width ratio as a function of increasing flow ratios for a sheath channel that is 90° from the main channel, where f is the focusing ratio of focusing width to channel width, and r is the volumetric flow ratio of sheath volume to sample volume[59].

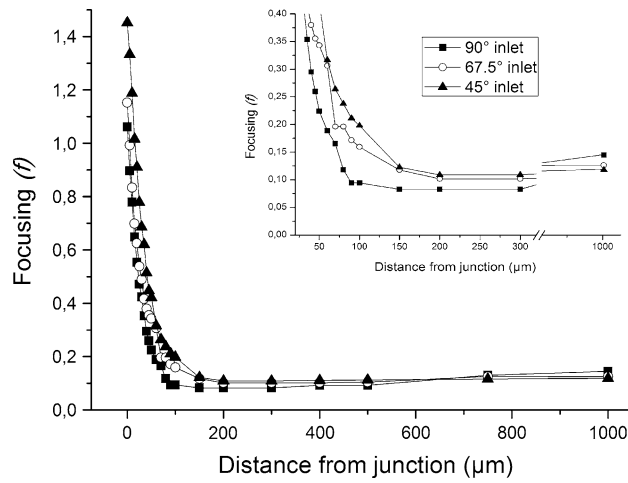


Figure 3.6: Focusing fraction as a function of distance from the junction for $\kappa = 6$ [59]

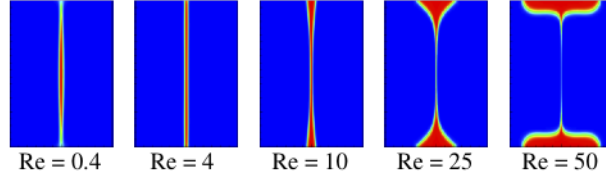


Figure 3.7: Mass fraction distribution of the focused fluid in the channel cross-section calculated when $\kappa = 20$ [60]

3.2.2 Shear force

The parabolic velocity profile due to pressure-driven flow introduces a shear force on cells in the fluid medium. Shear force is good for preventing cells from sticking to channel walls but could limit viability due to the stress on the cells [57, 61, 62]. Fluid shear in a square/rectangular channel is calculated as

$$\tau_w = \frac{6\mu Q}{h^2 w} \quad (3.5)$$

and in a circular channel is

$$\tau_w = \frac{4\mu Q}{\pi r^3} \quad (3.6)$$

where μ is fluid viscosity, Q is the volumetric flow, h and w are the channel height and width for square/rectangular channels, and r is the radius of the cylindrical channel.

In addition to the shear that is present within the channel, extensional or elongation flow, increasing shear stress, occurs whenever the cross-sectional area of the flow channel reduces [62]. In microfluidics, this would be the inlet junction when the tubing connects to the microfluidic chip. When shear stress is too high, suspended particles experience elongational forces in the direction of flow and compression perpendicular to the flow streamlines shown in Figure 3.8 [62]. There exists a bursting membrane tension for each cell type and when the shear force exceeds this, the cell

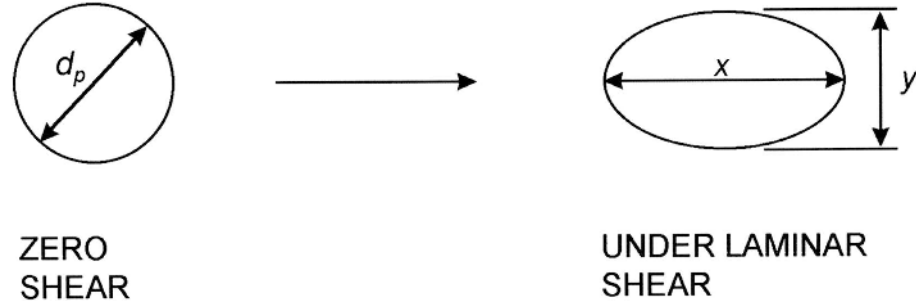


Figure 3.8: Deformation of a spherical cell when exposed to laminar shear stress. [62]

will be destroyed or damaged [61, 62]. Born et al. [61] has developed a model predicting cell damage in laminar flow and is updated by Christi [62]. As the computation of this model is quite lengthy, the consideration of shear force and its affect on cells will be ignored in this thesis. However, tube sizes similar to the channel size were selected to reduce extensional or elongational flow at the inlets.

It is also interesting to note that shear stress and other types of mechanical forces (e.g. stretch, strain, and compression) have been shown to mechanically-induce stem cell differentiation [63]. In her review paper, Stolberg et al. concludes that cells have a number of potential mechano-sensing mechanisms that allow it to sense and respond to shear stress. Similarly, ESCs also have some of the necessary equipment for sensing shear stress [63]. Although amazing, this induced differentiation is undesirable for the purposes of a cytometer.

Therefore, shear force has to be kept in mind when determining the design of the microfluidic system. Thankfully, for a ready-made chip, the shear force can simply be minimised by reducing the flow rate and thus the volumetric flow rate Q .

3.3 Available pressure driven flow systems

The ability to reliably control the pressure and speed of flow in the channel is important for a microfluidic system. It is required for both the injection of cells into the device, and the sorting of desired cells after detection. The flow control requirements for a microfluidic cytometer is the ability to supply a steady source of pressure to the channel, resulting in a constant flow velocity, if hydrodynamic focusing is used. The flow should also be able to reach low speeds, compatible with the response time of the detection camera. Low speed also avoids shear force.

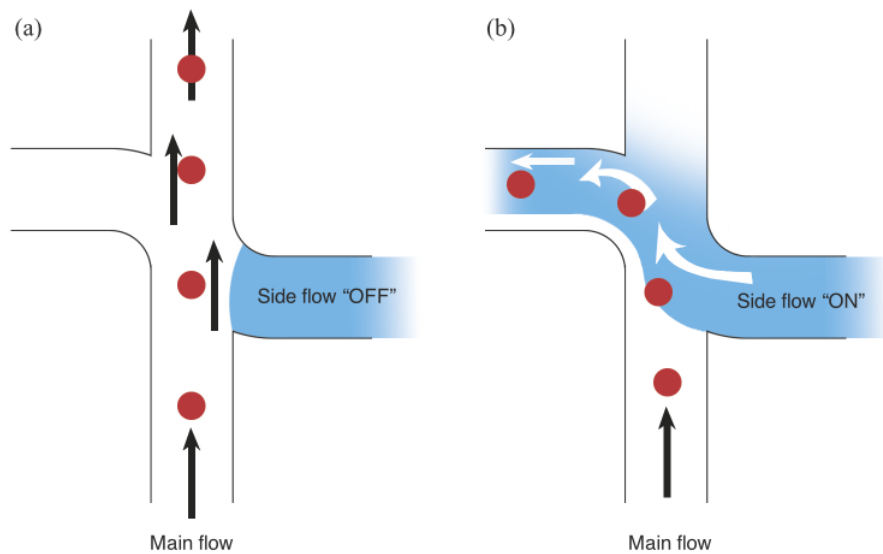


Figure 3.9: Sorting of cells when (a) side flow is turned 'OFF' (b) side flow is turned 'ON'

For hydrodynamic sorting of cells, a cell flows past a detection region and the detection camera or photomultiplier tube (PMT) sends a signal that triggers the side sorting pump. Cells will be pushed from the main channel into a side bin when the side flow is activated, as shown in Figure 3.9. One key factor that affects the rate of sorting is the switching time of the pump system used. A shorter switching time

means that there is less delay between the moment of detection and sorting. To account for pumps with low response times, a delay is usually introduced by either slowing down flow speed or by designing a longer channel between the detection area and the sorting intersection. This increases processing times. With a faster response, the process can be sped up and the device could experience a higher throughput. Table 3.1 presents a summary of several commercially available pump systems.

Table 3.1: Pressure driven flow system characteristics

Technology	Type of Flow	Response Time	Cost
Peristaltic Pump: Dolomite 3200243	pulsed	< 1s*	approx. \$190**
Syringe Pump: Norgren Kloehn 50300	continuous	seconds	approx. \$140***
Pressure Generated Flow: Fluigent MFCS-FLEX Elveflow AF1P200	continuous continuous	<200ms 80ms	approx. \$17,000** approx. \$2,500**

* Estimation of the peristaltic system's response time was given by Richard Grey, Head of Sales, Blacktrace Inc the US office for Dolomite Microfluidics (Charleston, MA, USA).

** Information was gathered from manufacturer's website or from email quotations.

***Cost is based off an ebay sale price as manufacturer states that this particular model is obsolete due to component availability.

To create a pressure driven flow, the pump can take the form of a macro pump located externally or an integrated MEMs pump that can operate on a variety of principles. MEMs pumps offer a form of flow control that are able to handle small

amounts of liquid with dynamic and precise switching [68]. However, they are still under research and have not been used commercially yet. Using a MEMs pump with the flow cytometer has potential but at this stage, it would be a new project in of itself.

Peristaltic pumps run on low DC voltages and work by running rollers in the pump head, called the cam, over a flexible tubing. The alternating compression and relaxation of the tube draws fluid through the pump and into the channel. A peristaltic pump is an accurate dosing pump as an equal amount of liquid is pushed through the channel at each pulse. Increasing the voltage of the pump increases the speed of the rollers and the flow rate. The main advantage is that since the pump only has contact with the outer surface of the tubing, thus reducing contamination between the pump and the sample fluid to essentially zero. When switching samples, all one has to do is to switch the tubing. A peristaltic pump is also non-siphoning which means that they prevent back-flow from the system. This promotes even more accuracy in fluid flow. However, the peristaltic action means that flow is pulsed rather than continuous resulting in oscillations in flow rate and pressure pulsations. This means that hydrodynamic focusing will not work as the pressure between the sheath and sample stream will periodically fall to zero, encouraging mixing of the streams. It is interesting to note that pulsed flow has high efficacy as a cleaning method due to high wall shear forces. This has been demonstrated experimentally[69, 70, 71] and theoretically via models [72, 73]. Thus, if microfluidic chips are to be reused, the peristaltic pump works well to clean out the channel. A peristaltic pump also has the potential to drive a hydrodynamic side flow for the sorting of cells. The response time was estimated by Richard Grey from Dolomite Microfluidics (personal communication, 26th March 2013) to be less than 1 second. This number depends on the inertia of the internal motor, elasticity effects as the tubing is squeezed by the cam,

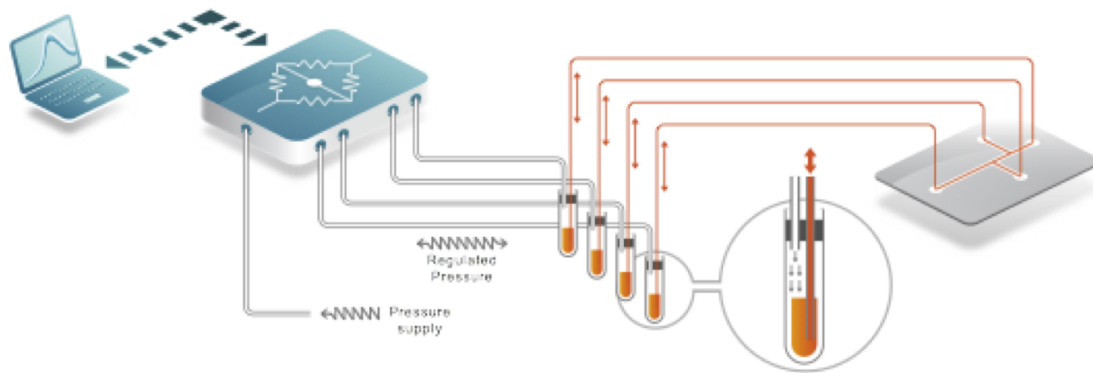


Figure 3.10: Schematic for a pressure generated pump, Fluigent MFCS-FLEX system. [74]

the fluid response as a result of the cam starting to move and back-pressure builds up, any compressibility effects due to air bubbles in the system, and the elasticity of the tubing between pump and the point at which the fluid flow needs to be controlled. Furthermore, since the pump is periodic, the system's response time will also depend on the position of the cam at the starting point. More work has to be done to determine the feasibility of using a peristaltic pump to drive a hydrodynamic side flow for sorting.

High precision syringe pumps are used widely in microfluidics. It consists of a piston that is pushed or pulled by a drive screw operated by a motor, resulting in smooth flow. While this arrangement allows the realisation of steady pressure gradients, the dynamic control over the flow rates in such systems is poor. Flow response is often in the seconds or minutes.

As for pressure generated pumps, it works on simple mechanical principles. A micro-controller controlled airflow pump is connected to a sealed container containing the liquid that is to be pumped into the channel. As the air pressure is increased, the contained liquid is forced up a tube connected to the microfluidic channel. For a flow

cytometer, this method of pressure driven flow is by far the most suitable providing a faster response time and no flow oscillation whatsoever. Our group previously used the microfluidic flow control system Fluigent MFCS-FLEX system with FLUIWELL. The system setup is shown in Figure 3.10. According to Fluigents specification sheets, the MFCS-FLEX system provides a flow stability of 0.1%, a response time of less than 200ms on average and a flow rates from 0 to 1000mbar depending on the model chosen. Another flow control system is the Elveflow AF1 P 200, with a response time of 80ms.

There is a need to develop a low-cost, fast-response flow control system. In Chapter 6 of this thesis, the details of a low-cost fast-response flow control system will be discussed.

Chapter 4

Microfluidic chip design for laser light scattering of cells

The label-free cytometer has gone through many chip revisions. Each time we try different materials or procedures to reduce the noise level, improve the coupling of light into the channel, streamline the fabrication process, and introduce other features such as cell sorting and hydrodynamic focusing. This section outlines the factors considered to create a microfluidic chip specifically for laser light scattering experiments. This includes a discussion on various chip materials, optical guiding of light into the channel, and main channel width. Lastly, I introduce the PDMS microfluidic chip that was chosen and its fabrication process.

4.1 Choice of materials

There are a wide range of materials used in microfluidics, spanning from glass and silicon to thermoplastic and thermoset polymers. For laser light scattering experiments, the material must first meet the following requirements:

1. Good optical transparency in the visible range (approx. 90% Transmission)
2. Free from internal micro-structural defects to reduce subsurface scattering
3. Smooth channel walls and channel floor to reduce surface scattering
4. Hydrophilic surface properties (or treatable) for low flow resistivity
5. Channel walls perpendicular to channel floor (for easy comparison to the computational model presented in Islam's thesis [75])
6. Leak-free bonding
7. Safe for biological cells

This can be summarised into the optical properties of the material, reduction of background scattering noise, surface properties, bonding, and biological compatibility. Three materials (glass, PMMA, PDMS) have been investigated in this thesis.

4.1.1 Optical properties

Optical transparency of various materials can be determined from transmission spectra as shown in Figure 4.1. Setting Borofloat glass as our optical transparency standard, at a wavelength of 532nm, PDMS is the closest contender. In second place would be 0.25mm of PMMA, followed by 0.25mm of PC.

We can also analyse the index of refraction (n) of the material to see how well it matches with that of DI water ($n=1.33336$ at 20°C , 589nm [77]) and phosphate buffered saline (PBS) ($n=1.335$ at 20°C , 589nm) [78] that cells are usually suspended in. When the indexes of refraction match, there is less scatter on the fluid-solid interface, potentially cutting down the noise. Indexes of refraction and the percent transmission (due to fresnel equations) of typical microfluidic chip materials are shown

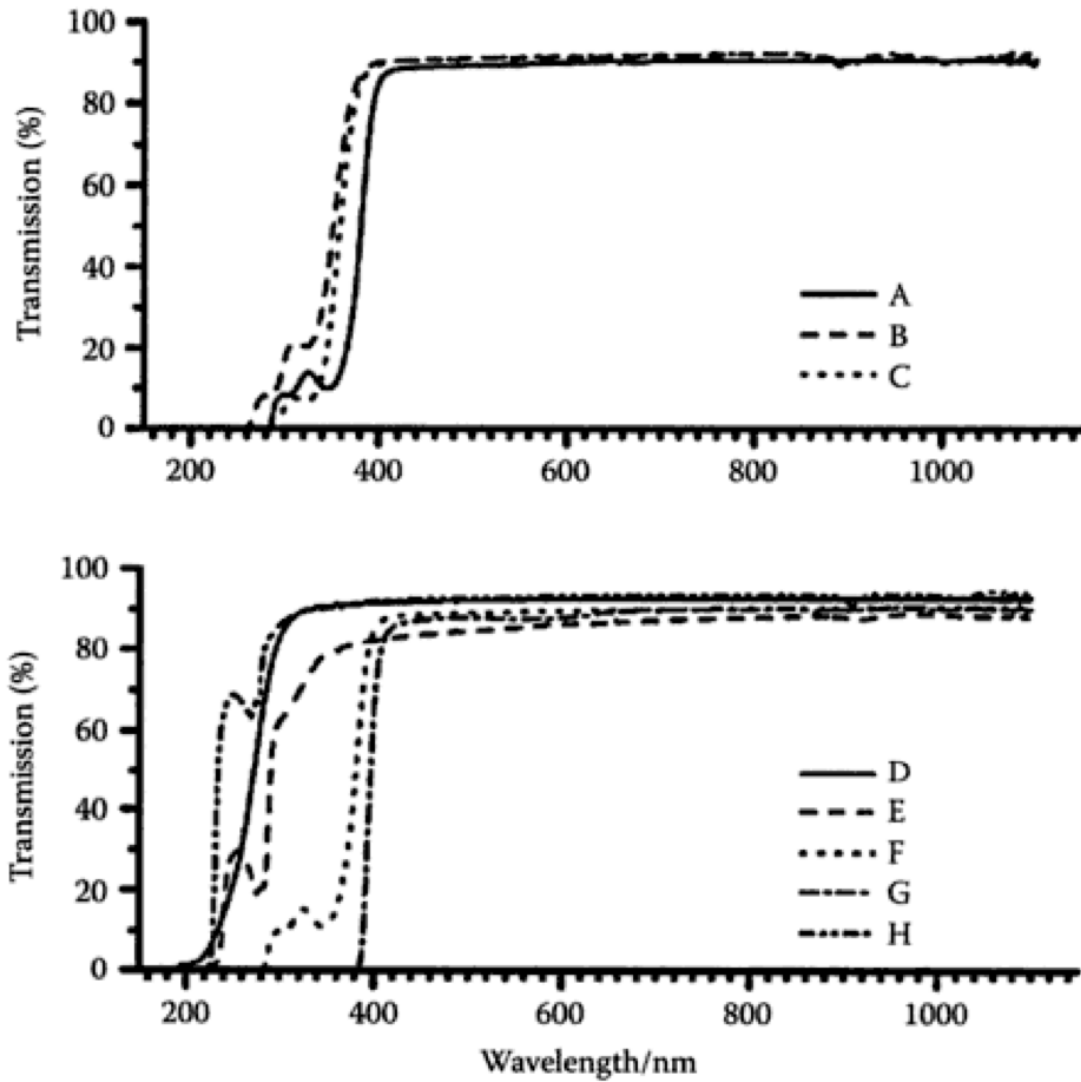


Figure 4.1: Transmission spectra taken at normal incidence of the plastic materials. Top panel: (A) 0.25 mm, (B) 3.0 mm, and (C) 5.0 mm PMMA. Bottom panel: (D) Borofloat, (E) COC, (F) 0.25 mm, and (G) 2.0 mm PC, (H) PDMS. [76]

Table 4.1: Comparison of the optical properties [79]

	Glass	Quartz	PDMS	PMMA	PS	PC	COC
Index of Refraction(n)	1.46	1.544	1.4118	1.491	1.59	1.586	1.53
Transmittance at 589nm *	93%	92%	94%	92%	91%	88%	92%

*Includes losses due to fresnel reflection

in Table 4.1. PDMS has the closest index of refraction match to DI water and PBS. Glass is a good second choice.

4.1.2 Reducing background noise level

When a laser is incident on an optically transparent material with a large surface roughness and internal non-uniformities, it results in large amounts of scatter within the chip that when imaged with a CCD creates large background noise. The large background light level makes it difficult to detect weakly scattering cells such as platelets and embryonic-like stem cells, because their small sizes causes the scattered light to be indistinguishable from the background noise [27]. Thus, to reduce the background noise level, one must eliminate any internal micro-structural defects and reduce the surface roughness of the material. This unfortunately is dependant on the manufacturing process and will differ not only from material to material, but also from batch to batch.

In a 2009 paper looking at scattering characteristics of PDMS, Santiago-Alvarado [80] found that the PDMS sample studied had a average roughness of 550.87 nm and a maximum pore size of 80 x 80 μm . The pore size is cause for concern considering

that the walls of our waveguide ($20\ \mu\text{m}$ width) is on the same factor as the maximum pore size reported in [80].

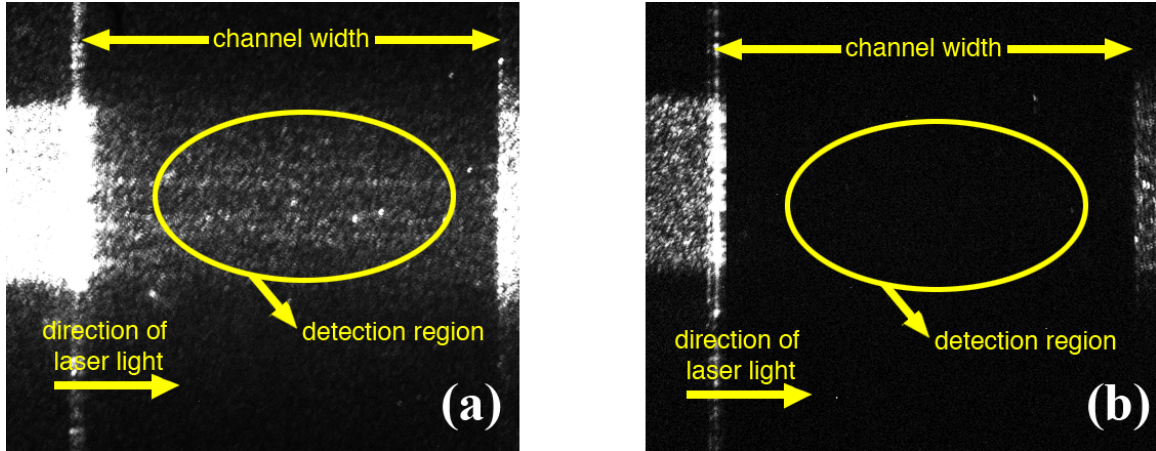


Figure 4.2: Scattering due to surface roughness and internal impurities such as micro-bubbles or dust particles for (i) PDMS to PDMS chip (ii) Borosilicate glass to PDMS chip.

A simple qualitative experiment was carried out by shining green laser light (532nm) into (i) a PDMS chip with a water-filled micro-channel and (ii) a PDMS layer with a water-filled micro-channel bonded to a featureless borosilicate microscope glass slide. As seen from Figure 4.2, there is much more internal scattering in the detection region from the PDMS-PDMS chip as compared to the PDMS-glass chip. This is assumed to be due to the reduction of pores by replacing one of the PDMS layers with glass. More quantitative work has to be done to determine the pore size and uniformity of the PDMS chips used in this thesis. Further work is also required to adjust the fabrication recipe to minimise these internal non-uniformities in the PDMS.

As seen from the glass-PDMS chip, the microscope slide glass used is of optical quality with low surface roughness and internal non-uniformities. Xu [21, 25, 26, 27] used a microscope glass based chip in his label-free cell experiments successfully. Un-

fortunately, the fabrication of channels in glass is more complex and time consuming as compared to polymers.

Another possibility is the use of an opaque material for one layer of the microfluidic chip, ideally the layer that the channel is etched into. This would eliminate the scattering of light on the fluid-solid interface and decrease some of the background noise that results from this effect. Internal non-uniformities would be a non-issue but surface roughness will still have to be taken into account. This is feasible in PMMA as it is available in a range of colours including opaque black.

4.1.3 Surface properties

For micro-channels because the surface-area-to-volume ratio is high, the surface properties play an important role on the resistivity of the flow through the channel. For most flow systems, the channels need to be hydrophilic to allow repeatable filling and flowing of the system. A hydrophilic channel also reduces the pressure required initially to fill the channel and the driving force in moving the liquid [64]. Thus, hydrophobic surfaces require a surface treatment implemented during the chip fabrication process or prior to use to promote wetting. There are a variety of treatments that are easily implemented and range from plasma oxidation, ultraviolet (UV) exposure, and chemical modification [51].

Glass is hydrophilic and so is silicon and poses no problems. On the other hand, naturally hydrophobic PDMS (Poly dimethylsiloxane) and PMMA (Poly methyl methacrylate) are difficult to wet with aqueous solutions, prone to the adsorption of other hydrophobic species, and easily nucleates bubbles [51, 65]. When exposed to plasma oxidation, the treated surface becomes hydrophilic due to the presence of silanol groups. However, this oxidised surface of PDMS is unstable in air and reverts to be-

ing hydrophobic in approximately 30 minutes. Keeping the oxidised PDMS in contact with a polar liquid, however, protects the surface although the long-term stability of the oxidised layer is unknown. [66, 65] This can be done by pumping the PDMS channel with de-ionised (DI) water (a polar liquid) and immersing it in a DI water bath. Pumping the channel full of water and sealing it off with tape is not a viable option as the silicone material itself can exchange gases [57] and evaporation would occur. Another option would be to treat the surface with UV-ozone treatment as the hydrophilicity of the surface was more stable after this treatment than after oxygen-plasma treatment [67]. Bonding PDMS to a hydrophilic material, such as glass, can also reduce the resistivity of fluid flow in the channel.

4.1.4 Bonding

A leak-free bond is important due to biological safety issues and so none of the sample is lost. Bond strength is also important since the main channel experiences large pressures which the bond should be able to withstand.

In the previous microfluidic chip design described in [22, 23, 27], an adherent bond was used to glue glass slides to a polymer sheet with the channel cut out. UV epoxy (Optical adhesive 81, Norland Products Inc., NJ, USA) was applied to the edges and cured with UV light for approximately 2 minutes.

A similar process was attempted with a PMMA chip and proved to be the only method of effectively bonding PMMA to glass. Although this design does not require nano-fabrication facilities, the chip tends to leak as the seal degrades with exposure to fluid. Furthermore, capillary action tends to pull the glue into the microfluidic channel, filling it. When the glue is rinsed off with isopropyl alcohol (IPA) to attempt bonding a second time, some of the glue remains in the channel dominating the scatter

patterns as shown in Figure 4.3. Other failed attempts to bond PMMA to glass can be found in Appendix A.1.3.

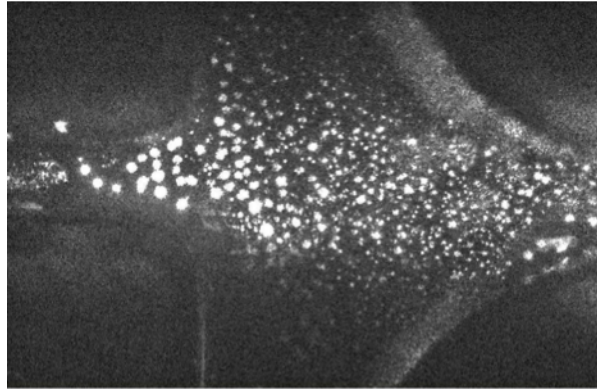


Figure 4.3: PMMA chip with speckles caused by glue falling in the channel

Adherent bonding aside, other methods of bonding are less likely to fail and often form permanent bonds. There are many established methods for glass to glass bonding and polymer to polymer bonding.

Glass to glass bonding can be done via thermocompression bonding or annotated bonding. Thermocompression bonding, as the name suggests, involves subjecting the sample to high temperatures of up to 900°C while maintaining it under high pressure [94]. After time has elapsed, the two substrates would have formed a strong irreversible direct bond. This method also works for most thermoplastic polymers, also called thermosoftening plastics, which turn into a malleable solid or liquid when heated and hardens to a smooth glassy state when cooled [96, 97]. Examples include PMMA, PET, and COP. Unlike thermoset polymers (e.g. PDMS), thermoplastic polymers can also be resoftened and reshaped upon heating, remaining chemically and dimensionally stable over a wide range of operational temperatures and pressures [96].

In annotated bonding, a high voltage is applied across the glass to creating a polar-

isation and electrostatic attraction between the two surfaces as the Na^+ ions in the glass move away from the interface [94]. In both cases, since it is a bond between two similar materials, glass-to-glass, a direct Si-O-Si bond is created which is virtually irreversible even when the bond is subjected to high stress or pressure. Since no additional materials are used, as long as care is taken to clean the surfaces beforehand and prevent particulates from falling in the microfluidic channel, blockage of the channel is not a concern.

To bond PDMS to PDMS, PDMS layers are exposed to oxygen plasma for surface activation. Both substrates are brought in to immediate contact and gently pressed together to form an irreversible chemical bond. Similarly to bond PDMS to glass, oxygen plasma can be used to activate the surface of the PDMS layer. When the PDMS and glass layers are pressed together, van der waals forces ensure a tight, albeit reversible, bond.

4.1.5 Biological compatibility

Glass is the standard material for use with biological samples as it is a stable, inert material that does not interfere with viability or growth. Similarly, plastics such as PC and PS are widely used to produce culture flasks and well plates for conventional cell culture experiments.

However, not all plastics are biocompatible. Recent research by Midwoud et al. have shown that PMMA treated with UV-ozone results in a non-biocompatible surface for surface adherent liver-cell cultivation [67]. Unstable peroxides form on the surface during the UV-ozone treatment and contribute to cell toxicity [67]. We can stipulate that this would apply to suspended cells as well, making PMMA not suitable for use with live biological cells. Other tested polymers, namely PMMA, COC, PS, PC and

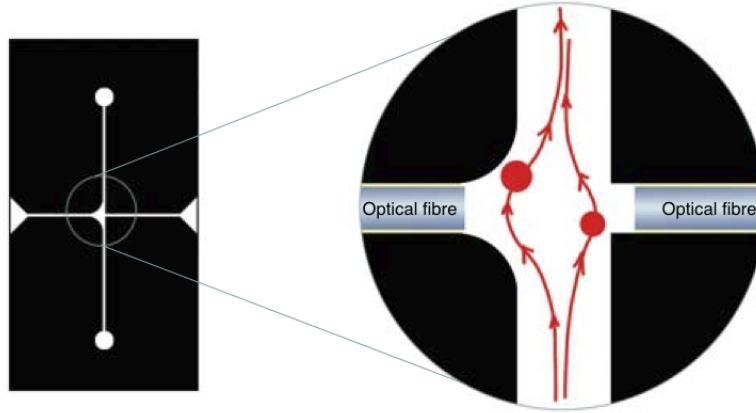


Figure 4.4: Flow pattern due to insertion of optical fibres. Cells flowing through the chip do not flow in a straight line.

PDMS, proved to be biocompatible.

4.2 Optical guiding

An important consideration is the ability of the chip to guide light into the main channel to the detection spot. To build an integrated waveguide based on the principles of total internal reflection, there has to be a way of confining light in the core material by choosing a cladding material with a lower index of refraction.

In the previous glass based microfluidic chip described in [22, 23, 27], cleaved optical fibres (105/125 μm multimode fibre, Thorlabs, NJ, USA) were inserted into the chip on both sides of the main channel prior to bonding. One optical fibre serves to guide laser light into the area of detection and the other fibre would lead excess light out of the area to reduce scatter. A similar insertion of fibres was also attempted with an opaque PMMA chip. However, this proved disadvantageous to the flow path of suspended cells in the main channel as shown in Figure 4.4. As the chip was

assembled by hand, often, the optical fibres were not aligned with the wall of the main channel. This forms a channel deformity right in the detection region. Not only is flow disrupted, making cells harder to find and their speed harder to predict, bubbles tend to nucleate between the fibre and main channel. The air-water interfaces of the bubble result in a large amount of scatter, saturating the detection region with noise. Besides not lining up with the edge of the main channel, the fibres often did not align well with each other resulting in scatter. Having a core width of only $105\ \mu\text{m}$, the optical fibres were also prone to breakage.

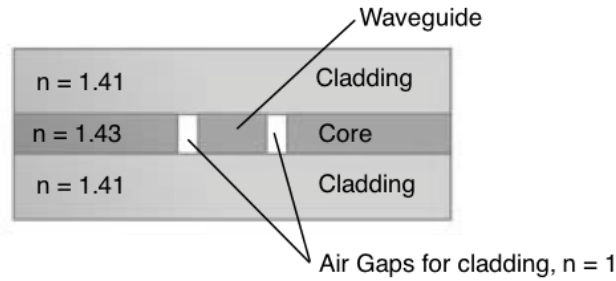


Figure 4.5: Cross-sectional view of an integrated waveguide in a PDMS chip formed using high index PDMS ($n=1.43$) as a core and air ($n=1$) and low index PDMS ($n=1.41$) as the cladding.

In the PDMS chip that was designed by our group for fluorescent bead sorting [75], an integrated waveguide was created with the use of high index and low index PDMS, eradicating the need to insert optical fibre into a chip. The waveguide, shown in Figure 4.5, consists of a central core of high index PDMS (3-6121, Dow Corning, MI, USA), $n = 1.43$, sandwiched on two sides by an air channels of $20\ \mu\text{m}$ and top and bottom with low index PDMS (Sylgard 184, Dow Corning, MI, USA), $n = 1.41$. Measured propagation losses in the waveguide are 1.6 and 1.5 dB/cm at 532 nm and 633 nm [75] which are higher than an inserted optical fibre. This seems to be a good tradeoff for a simplified fabrication process with an increased yield. However, the

light lost in these integrated waveguides might add to the internal scatter of the chip, undesirably raising the background noise level.

4.3 Channel width

Channel width is an issue as it would affect flow patterns and flow speed. This was the issue with the previous chip design described in [22, 23, 27] which has a microfluidic channel of width of $600\mu\text{m}$, height of $120\mu\text{m}$. A large (in microfluidic terms) channel width and height means that it is difficult to predict where the cell is in the channel causing varying position-dependent scatter patterns. Since the laser light diffuses in a conical angle once it leaves the optical fibre, there is also a reduction of laser light intensity (and thus scattered light intensity) across the channel width. Given a deep channel, cells also tend to drift in and out of focus, resulting in a scatter pattern that fluctuates in intensity. This can be minimised with a narrower and shallower channel. Furthermore, since this channel was cut by hand with a surgical knife, the sides were rough and caused ambient scatter. This was not an issue previously as the channels were large enough that any scatter from the rough walls was far enough that it did not interfere with a scatterer in the middle of the channel. Thus, this fabrication technique has to change once we start reducing the channel width.

On the flip side, the PDMS chip design used in [75] has a narrow channel of $60 \times 60\mu\text{m}$ (width x depth). This required high pumping pressures resulting in very high flow speed. It also creates flow memory in the channel, making sudden changes in flow speed virtually impossible. Furthermore, as the channel walls are closer to the cell, scatter from the channel walls interferes with the defocused scatter images of cells, often saturating the image making background subtraction impossible. Unfortunately, the $60\mu\text{m}$ depth is restricted by the fabrication process used to create the master

described in Section 4.4.

Thus, a middle ground has to be found between these two extremes for a channel with that has reduced scatter from side walls, controllable flow speed, and low fluctuation of scattered light.

4.4 Modified PDMS chip

PDMS has an index of refraction closest to DI water, irreversible and fast bonding, biocompatibility with cells, easy fabrication, and the ability to include a integrated waveguide. This, coupled with the fact that PDMS chips have been successfully used in particle sorting (which I want to integrate into the label-free system), make it a good choice. Furthermore, previous attempts at a PMMA-glass chip was thwarted due to issues with bonding. I decided to adapt the PDMS chip previously developed in our group for fluorescent bead sorting [75] for my purposes of laser light scattering and sorting of cells. The previous PDMS chip had many good components that I have kept in my design, namely the integrated waveguides, the implementation of hydrodynamic focusing, and the fluid sorting channels, shown in Figure 4.6. The fabrication recipe was also adopted and adapted.

I designed a chip with channel dimensions of $200 \times 60\mu\text{m}$ (width x depth), Figure 4.7. I also added more waveguides along the channel and positioned three chips on one master to increase production yield by 1.5 times. The experiments presented in this thesis was performed using this $200\mu\text{m}$ chip. However, for weakly scattering cells the $200\mu\text{m}$ chip proved to still suffer the problem where scattering from the walls still interfered with the cell's scattering pattern. Thus, a chip with a channel width of $300 \times 60\mu\text{m}$ (width x depth) was created, Figure 4.8. The design was slightly simplified by removing the waveguide dumps and the 45° waveguides as they were not being

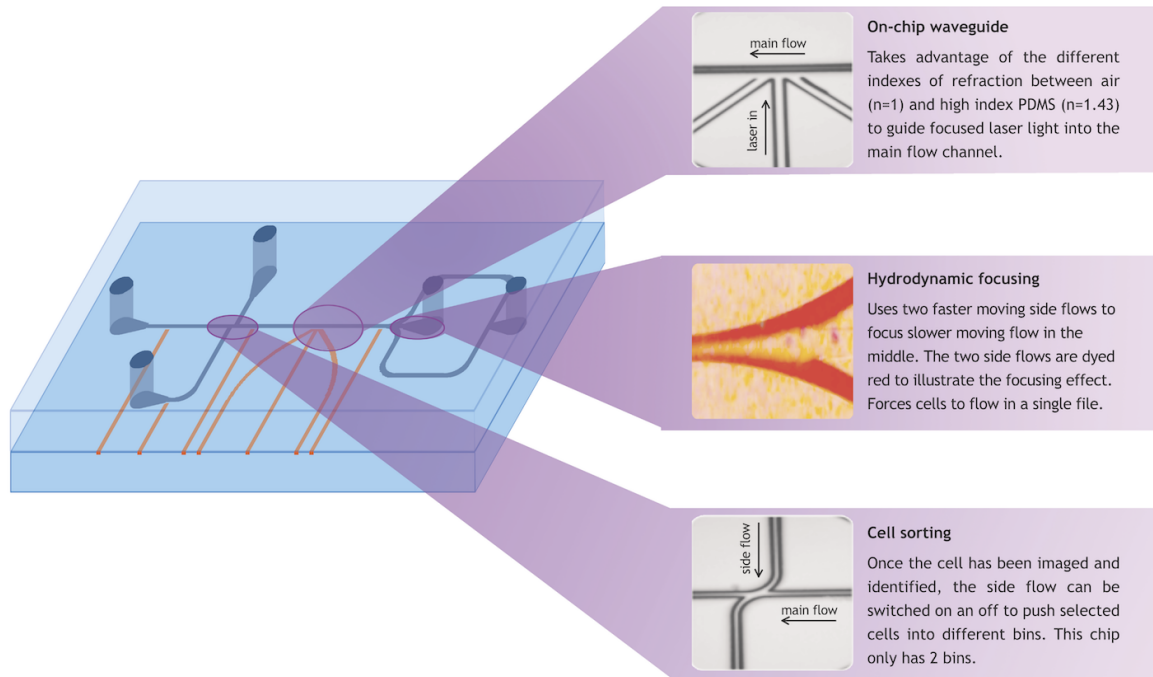


Figure 4.6: PDMS chip with integrated waveguides, implementation of hydrodynamic focusing, and fluid sorting channels. Photos taken from [75].

used and contributed to the unwanted background scatter.

4.4.1 Fabrication

PDMS fabrication begins with the creation of a silicon master, with the channels as raised features. We then form channels in PDMS by replica moulding where the PDMS is poured onto the master creating a negative imprint.

To create a silicon master, the channel design was first drafted in a layout editor, L-Edit (Tanner EDA, CA, USA). With a pattern generator (DWL 200, Heidelberg Instruments, CA, USA), the design was printed into a chromium on glass mask. Meanwhile, a SiO_2 coated Si wafer was purchased. The SiO_2 layer is approximately 500nm thick. The SiO_2 coated Si wafer is then dehydrated and coated with a mono-layer of

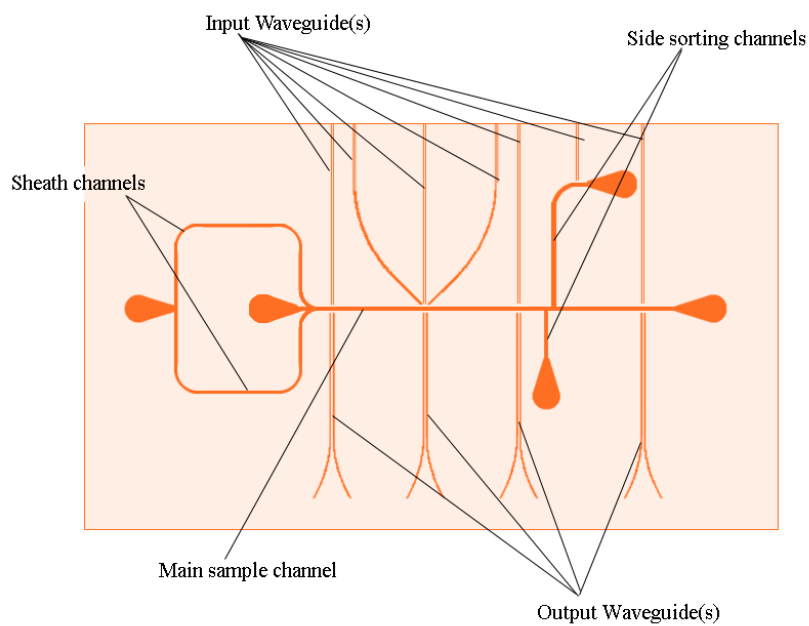


Figure 4.7: Design for the 200x60 μm chip

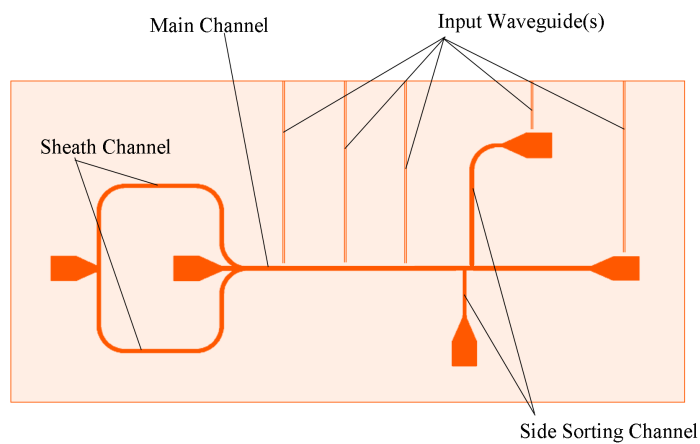


Figure 4.8: Design for the 300x60 μm chip

HDMS (hexamethyldisilazane) with a HDMS oven (YES-310TA, Yield Engineering Systems, CA, USA). Conventional photolithography and wet etching steps (HPR 504, Developer 354) were then used to transfer the pattern from the mask to the Si wafer. Exposed parts of the SiO₂ layer was then etched off to create a hard mask with STS RIE (Branson, company no longer exists). The remaining layer of photoresist was ashed off in a Branson Barrel Etcher. Finally, the Si is dry etched by a deep reactive ion etching (DRIE) process. The two available DRIE processes are via Cryogenic or Bosch. Both methods were attempted and the results are discussed in Section 4.4.2. The SiO₂ hard mask is etched away during the DRIE process, resulting in some roughness. Thus, the remaining layer is removed with STS RIE (Branson, company no longer exists) exposing the smooth Si surface. Lastly, the Si master is salinised to prevent sticking of the PDMS with trichlorosilane (HCl₃Si) in a glass desiccator for 2 hours. A pictorial methodology is shown in Figure 4.9. Although the fabrication of a Si master is tedious, once made, it can be used over and over again.

With the master made, I proceeded to create the PDMS chip. A thin layer of high index PDMS (3-6121, Dow Corning, MI, USA) premixed with its curing agent is smeared onto the waveguide structures of the master. A nitrogen gun is then used to remove bubbles and spread out the PDMS layer into a thin even layer that is flush with the protruding waveguide and channel structures on the master. This is semi-cured in an oven at 80°C for 30min under a vacuum of 5inHg. It is important to ensure that shelves in the oven are level. An O-ring and a metal ring with a diameter slightly smaller than the master is placed onto it and clamped into place, Figure 4.10. This prevents liquid PDMS from spilling out of the master and enables us to create thicker chips. Low index PDMS pre-polymer (Sylgard 184, Dow Corning, MI, USA) is mixed with its curing agent in a 10:1 ratio, degassed, and poured onto the master on top of the previous high index layer. Simultaneously, some of the low-index PDMS is

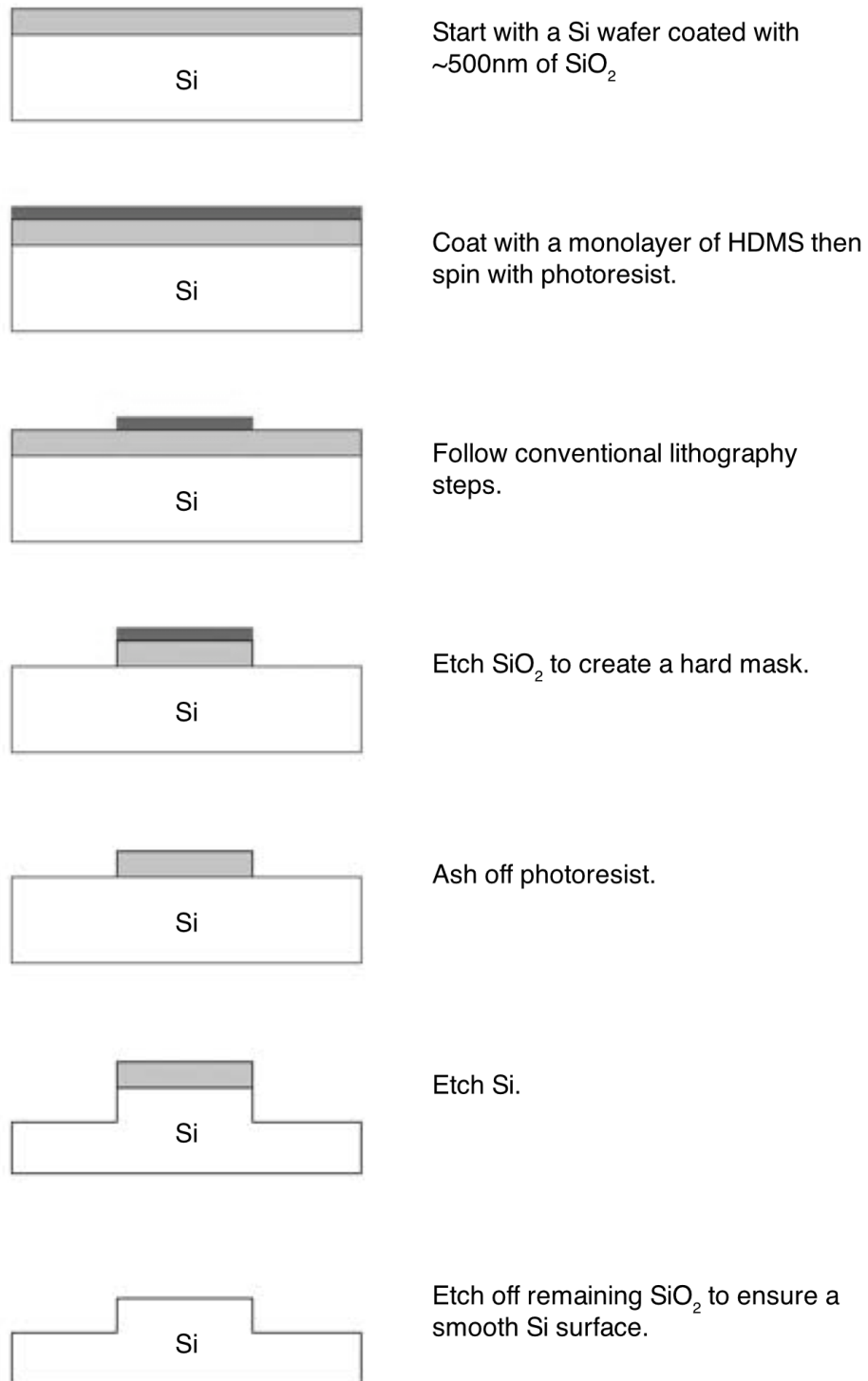


Figure 4.9: Fabrication process for Si master

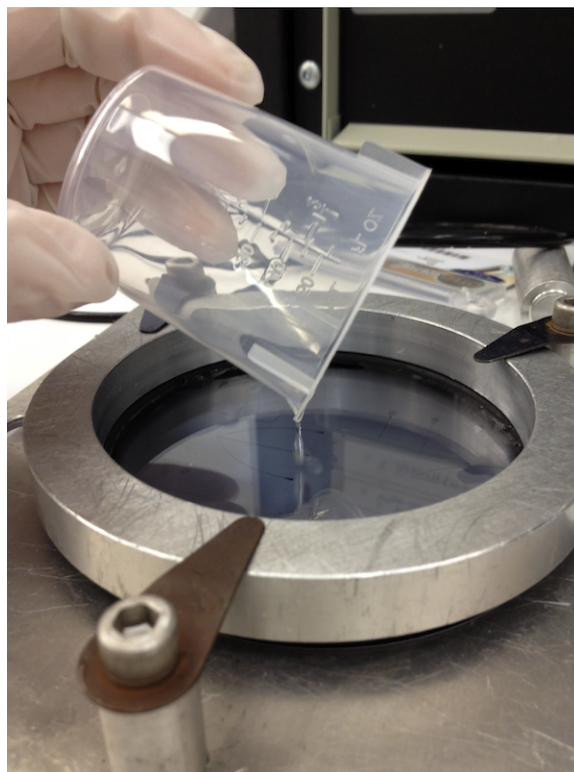
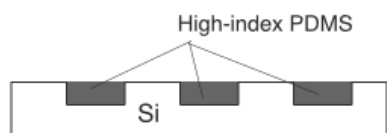


Figure 4.10: Pouring the low-index PDMS on to the Si master while in a clamp.

poured into a disposable petri dish [08-757-9B, Fisher-Scientific, ON, Canada]. This will become the featureless top layer. These are both baked in an oven at 80°C for 2 hours under a vacuum of 5 inHg. Carefully, I peeled the PDMS from the master and from the petri dish and blue taped the features to prevent contamination. Reservoir holes are punched in the featured side with a core sample cutter (1.5 mm Harris Uni-core). To bond, PDMS layers are exposed to oxygen plasma for 30 seconds for cleaning and surface activation. This process also treats the PDMS surface turning it temporarily hydrophilic. Both substrates are brought in to immediate contact and gently pressed together to promote a leak-free seal. The PDMS chip is then placed under a weight overnight, forming an irreversible bond. This process is shown in Figure 4.11.



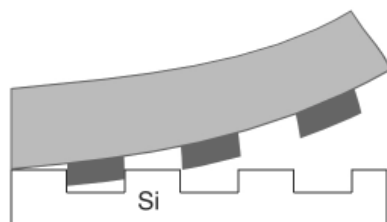
Starting with a Si master, salinise for 2 hours to prevent sticking.



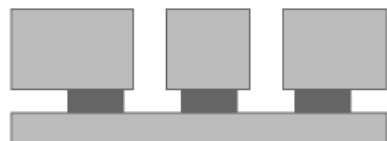
Apply a thin even layer of high-index PDMS making sure it is flushed with the features.



When the high-index PDMS has partially set, pour on the low-index PDMS and bake til set.



Peel PDMS off master.



Punch holes for the inputs and O_2 plasma bond to a plain PDMS layer or to glass. Press under a weight overnight.

Figure 4.11: Fabrication process for PDMS chip

Another option that was explored was to bond the featured PDMS layer to a glass slide in attempt to reduce background scatter noise caused by roughness from the top layer of the PDMS. The PDMS with defined features was first cut to size. Then, similar to the PDMS-to-PDMS procedure, the PDMS and standard microscope slides (12-544-1, 25mm by 75mm, Fisher Scientific Company, ON ,Canada) were exposed to oxygen plasma for 30 seconds for cleaning and surface activation. Both substrates are brought in to immediate contact and gently pressed together to promote a leak-free seal. The PDMS chip is then place under a weight overnight, forming a tight, albeit reversible, bond.

For storage, the chips (both PDMS to PDMS and PDMS to glass) were pumped with DI water, then immersed in a DI water bath to preserve the treated hydrophilic surface. The PDMS tends to turn cloudy when immersed in DI water due to it's porous nature but optical transparency can be reestablished by removing the chip from water approximately thirty minutes prior to use.

4.4.2 Reducing surface roughness

To reduce the background noise, one method is to reduce the surface scatter of the PDMS layer in the channel and outside as described in Section 4.1.2. Assuming that the PDMS surface roughness depends directly on the surface roughness of the Si master it is poured onto, I can determine the surface roughness by looking at the methods used to etch the Si master. Two methods were used for DRIE, cryogenic and Bosch; each process produces different roughness results especially for the side walls. Cryogenic ICP-RIE (Oxford instruments, UK) was favoured initially due to its ability to produce anisotropic sidewalls that are nearly vertical to match the group's computational model. It also has high selectivity requiring a SiO₂ hard mask thickness

of less than 200nm to reach an etch depth of $60\mu\text{m}$. Similarly, the Bosch process with the ICP-RIE (STS) is able to produce anisotropic side walls but alternates between an isotropic etching step and a deposition step, and is repeated until the desired depth is achieved. This results in sidewalls that have a noticeable scalloping. I was initially concerned that the scalloped sidewalls would produce large amounts of scatter in the PDMS-fluid interface. Selectivity is also low and with a SiO_2 hard mask thickness of 500nm, I was only able to reach an etch depth of $50\mu\text{m}$

Table 4.2: Roughness of Silicon Master

	Channel top surface (rms)	Not on the channel (rms)
Cryogenic process	0.598 nm	45.446 nm
Bosch process	0.983 nm	0.904 nm

However, with a wide channel and hydrodynamic focusing, the sidewalls did not contribute much to the noise. Instead, the roughness of the channel top and bottom proved to be significant contributors to the noise. The Zygo Optical Profilometer (Zygo Corporation, CT, USA) was used to determine surface roughness of silicon masters etched via Cryogenic or Bosh process. An area roughly $50 \times 50\mu\text{m}$ was selected from the scan and the Zygo software found the root-mean-square (RMS) value for each of the selected areas. A 3D map of the roughness results are shown in Figure 4.12 and Table 4.2 gives the RMS roughness value.

As shown in Table 4.2, the roughness in the channel is similar for both processes. The roughness in the channel for Cryo processing is excellent as it is the roughness

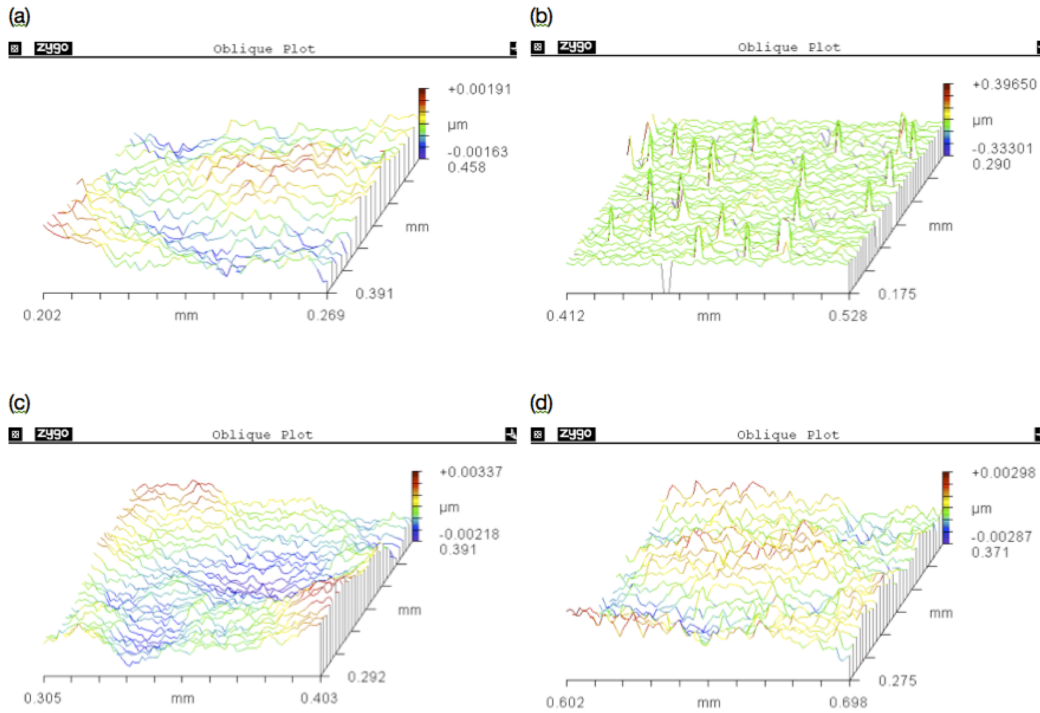


Figure 4.12: Plot of roughness on PDMS master using different DRIE processes (a) Cryo in the channel (b) Cryo not in the channel (c) Bosch in the channel (d) Bosch not in the channel

of the bare Silicon. The roughness in the channel for Bosch processing is higher than Cryo probably due to the fact that during this process, due to the low selectivity, I etched away all the SiO_2 and started etching in to the Si in the channel. For the roughness outside the channel, it is clear that Bosch gives superior results. Even though it is outside the detection area, the roughness can cause scatter within the chip that will add to the background noise level.

Chapter 5

Measurement of bead and biological cell scatter

New PDMS chips were evaluated in the label free cytometer by flowing polystyrene beads and cells through them and extracting their scatter patterns and intensities. Canadian Blood Services (CBS) provided fixed human cell lines (NC-37, HL-60, KG-1a) as well as CD34+ cells, which contain a mix of both hematopoietic stem cells (HSC) and progenitor cells. *E. coli* DH5 α cells were obtained from McMaster University.

These cells were chosen for particular reasons. As seen in Table 5.1, the cells are of different morphologies but still have the same nucleus to cytoplasm ratio. Furthermore, NC-37, HL-60, and KG-1a are of similar sizes and have smaller mitochondria as compared to CD34+ cells. *E. Coli*, being a prokaryotic cell, contains no membrane bound organelles and no mitochondria. *E. Coli* cells are also much smaller (0.5 μm by 2.5 μm) than the other cells being studied. The group of cell lines is also interesting to look at, as structurally myeloblasts are differentiated from lymphoblasts by more prominent nucleoli and less condensed nuclear chromatics. Further-

more, promyeloblasts contain many granules in their cytoplasm whereas myeloblasts have no granules. The two cells are otherwise similar structurally. I aim to see if these structural differences in the organelles contribute to a different scatter pattern.

Table 5.1: Cell characteristics

Cell	Morphology	Size	N/C Ratio*
CD34+	HSC & progenitor cells	6.5 μm [7]	0.8 [7]
NC-37	Lymphoblast	10 to 20 μm [81]	0.8 [81]
HL-60	Promyeloblast, Leukemic	15 to 20 μm [81]	0.8 [81]
KG-1a	Myeloblast, Leukemic	15 to 20 μm [81]	0.8 [81]
E.Coli DH5 α	Prokaryotic bacteria	0.5 μm by 2.5 μm [82]	N.A.

*where N/C Ratio is the ratio between nucleus and the cytoplasm.

This section describes the sample preparation procedure for these cells, the experimental setup and procedure, and experimental results.

5.1 Sample preparation

Human cells were prepared for us by the Canadian Blood Services (Edmonton, AB). According to Dr. Leah Marquez (personal communication, 18th Jan 2013), the human hematopoietic cell lines NC-37 (Burkitt's lymphoma), HL-60 (acute promyelo-

cytic leukemia), and KG-1a (acute myelogenous leukemia) were obtained from the American Type Culture Collection (Maryland, USA) and grown in RPMI medium (Invitrogen, ON, Canada) supplemented with 10% bovine growth serum (BGS, Hyclone, ThermoFisher Scientific, ON, Canada). To preserve these cells, they were fixed with freshly prepared 1% paraformaldehyde (PFA, Sigma, Oakville, ON, Canada) and diluted with 1 x PBS to a final concentration of 3,000 cells per mL. The final cell concentration was transferred to a micro-centrifuge tube (ThermoFisher Scientific, ON, Canada) and stored at -20°C until ready for use.

CD34+ cells were also prepared for us by the Canadian Blood services and according to Dr. Leah Marquez (personal communication, 18th Jan 2013), the CD34+ cells were isolated from umbilical cord blood and mobilised peripheral blood. Umbilical cord blood (CB) was collected at the Royal Alexandra Hospital (Edmonton, AB, Canada) from healthy, full-term newborn infants with the mother's informed consent, in accordance with the guidelines of the University of Alberta Health Research Ethics Board. The CB was processed within 24 hours after collection. First, the buffy coat was obtained by centrifugation of the whole blood at 1500 rpm for 7 min. When centrifuged, whole blood separates into layers of red blood cells on the bottom, a buffy coat layer containing white blood cells, and platelets, and a top layer of blood plasma. The buffy coat cells were suspended at a concentration of 7.5×10^6 cells per mL in serum-free Iscoves modified Dulbeccos medium (IMDM, Invitrogen, Burlington, ON, Canada), layered over a 60% Percoll gradient (1.077 g/ml, GE Healthcare, QC, Canada), and centrifuged at 1800 rpm for 20 min. The interphase cells or light density mononuclear cells (MNC) were collected, washed twice with IMDM, and re-suspended in phosphate-buffered saline (PBS, Invitrogen, Burlington, ON, Canada) containing 5 mM ethylenediaminetetraacetic acid (EDTA) and 0.5% bovine serum albumin (Sigma, Oakville, ON, Canada). The MNC were separated and enriched

for CD34+ cells using the Human CD34 Microbead Kit (Miltenyi Biotec, Auburn, CA, USA) according to the manufacturers instructions. Briefly, the MNC were magnetically labeled with CD34 MicroBeads. The cell suspension was then loaded onto a magnetic activated cell separation (MACS) column which was then placed in the magnetic field of a MACS Separator. The magnetically labeled CD34+ cells were retained within the column while the unlabelled cells (CD34- cells) were eluted. By removing the column from the magnetic field, the magnetically retained CD34+ cells can be eluted as the positively selected cell fraction. To preserve these cells, they were fixed with freshly prepared 1% paraformaldehyde (PFA, Sigma, Oakville, ON, Canada) and diluted with 1 x PBS to a final concentration of 3,000 cells per mL. The final cell concentration was transferred to a micro-centrifuge tube (ThermoFisher Scientific, ON, Canada) and stored at -20°C until ready for use.

Peripheral blood (PB) cells were collected by leukapheresis at the Cross Cancer Institute (Edmonton, Alberta) from patients diagnosed with malignancies without bone marrow involvement who are undergoing mobilisation using granulocyte-colony stimulating factor (G-CSF). PB samples were collected with patients informed consent and in accordance with the guidelines set by the University of Alberta Health Research Ethics Board and processed within 24 hours of collection. Light-density MNC and CD34+ cells were isolated as described above.

E. coli cells were obtained from McMaster University where according to Dr. Leyla Soleymani (personal communication, 29th May 2012), frozen stocks of *E. coli* DH5 α were streaked on to an Lysogeny broth (LB) agar plate. A single colony from the plate was used to inoculate 10 mL of LB, which was grown overnight at 37°C in a shaking incubator. The overnight culture was diluted 1 in 100 in fresh LB and grown for 4 hours, OD600 (optical density at a wavelength of 600nm) was measured to determine concentration of bacteria in the liquid. Cells were then diluted to desired

concentration of 10,000 cells per mL. Cell suspension pellets were washed twice with 1x phosphate-buffered saline (PBS) (pH 7.4) and aliquoted 1 mL per tube. Cells were frozen at -20°C . After cells had been frozen for 24 hours, a single tube was resuspended and plated onto LB agar to confirm growth. When ready for use, the E. Coil cells were reconstituted in 5 mL of PBS by vortexing (02-215-360, ThermoFisher Scientific, ON, Canada) before being drawn into a disposable syringe for pressure driven flow.

5.2 Setup and procedure

The label-free microfluidic cytometer can be broken down into (1) a coherent laser light source, (2) a fibre that couples the light into the microfluidic channel to illuminate a single cell, (3) the microfluidic chip containing a channel that propagates the cell to the illumination point, and (4) a CCD array that collects the 2D scatter pattern. Typical of a conventional bench top cytometer, the laser, fluid flow, and CCD are located orthogonal to each other. A schematic is shown in Figure 5.1, and a photograph of the final setup is shown in Figure 5.2.

Coherent light from a 532nm laser (LRS 532 TM200-5, DPSS laser, Laserglow Technologies, ON, Canada) was shone through a series of ND filters (ND 0.5, ND 1.0) that reduced the laser power from 200 mW down to 6.3 mW, so as not to saturate the CCD. The ND number represents the fractional transmittance:

$$\frac{I}{I_o} = 10^{-d}, \quad (5.1)$$

where I_o is the incident power, I is the power after the filter, and d is the optical density.

The beam was then directed through a series of apertures and mirrors placed at 45° and into a 4x microscope objective lens with a numerical aperture (NA) of 0.1. The light was focused into a approximately 3cm long multimode optical fibre (105/125 μm , Thorlabs, NJ, USA) that was mounted on a XYZ translation stage. The optical fibre, which had a NA of 0.22, was butt-coupled into the waveguide of the microfluidics chip. The light coupling, could be improved by adding a drop of glycerin at the entrance to the waveguide and by inserting the optical fibre into the glycerin drop. Glycerin ($n = 1.474$ [77]) acts as an index matching fluid, eliminating any air gaps between the fibre and the waveguide where large losses might occur. This is shown in Figure 5.3.

Cells are pressure-driven through the microfluidic channel with a disposable syringe at a concentration of roughly 3,000 to 5,000 cells/mL. The syringe is connected

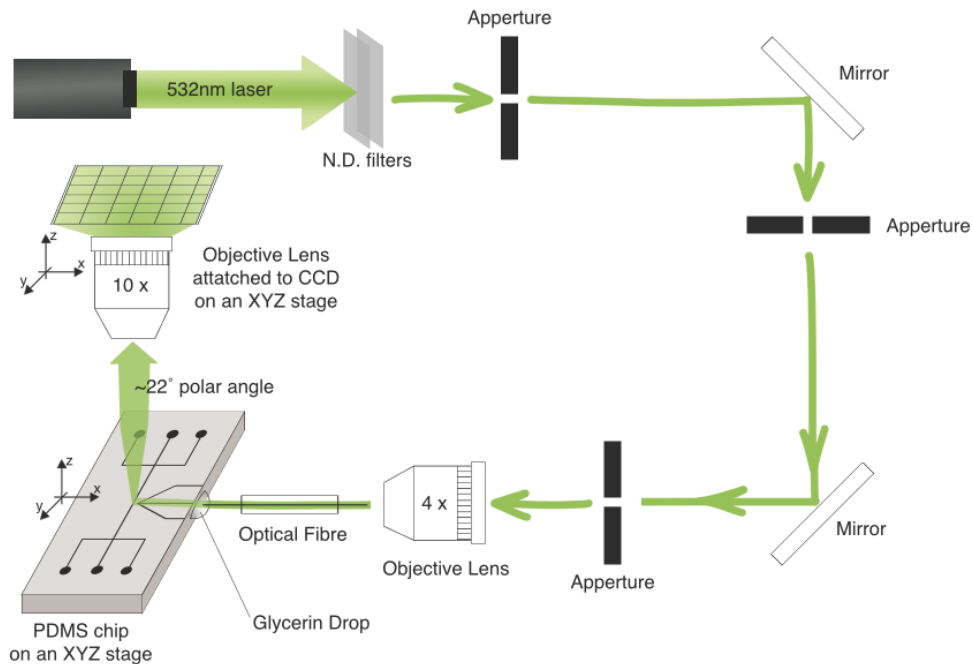


Figure 5.1: Schematic diagram for optical setup for label-free cytometer.

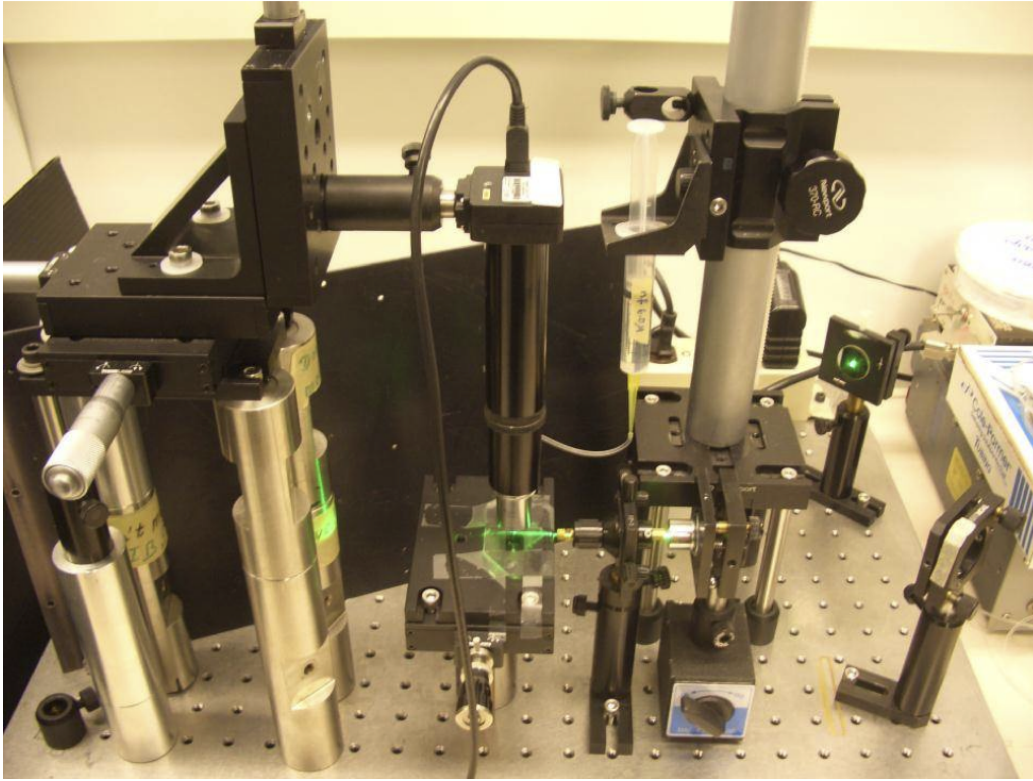


Figure 5.2: Photograph of optical setup for label-free cytometer.

to the microfluidic chip via a pressure fit pipette tip (02-707-500, Fisher Scientific, ON, Canada) to Tygon tubing (C-Flex RK-06422-00, Cole-Parmer Instrument Company, QC, Canada), to another pipette tip pushed into the inlet of the PDMS chip. To increase control over flow speed, bubble plugs were intentionally introduced to confine cells to a portion of the fluid. As a cell arrives at the observation area, it is immobilised by applying positive and negative pressures to the flow.

The side scattered light from cells were collected by a 10x microscope objective lens and onto a chameleon CCD array (CMLN-1352 M/C, Point Grey, BC, Canada) located above the chip. The CCD and objective lens combination was mounted on a XYZ translation stage enabling adjustment of the image focus. For the optimal cell scatter, the focused saturated image of the cell was found before defocusing by

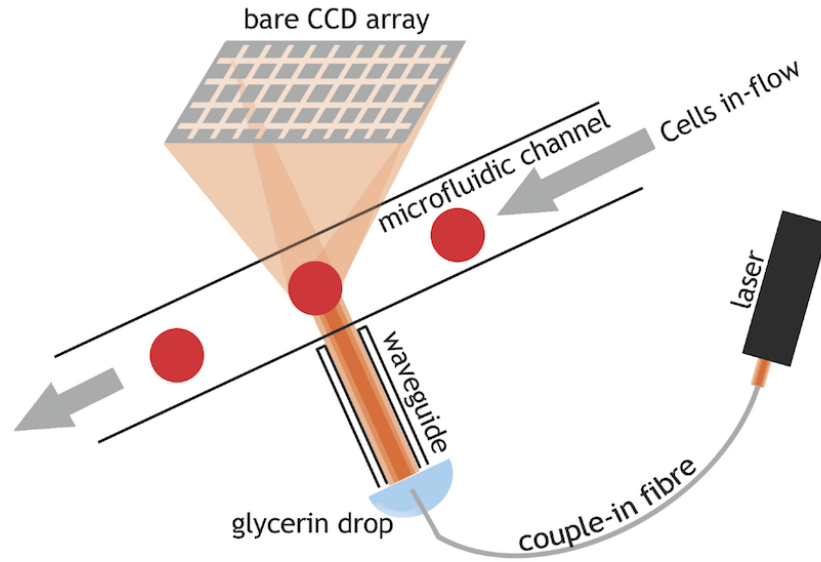


Figure 5.3: Schematic of the laser entering the chip via an integrated waveguide perpendicular to the microfluidic channel, hitting a cell, and scattering upwards into a CCD.

approximately $200\mu\text{m}$ to obtain a larger, more meaningful, scatter pattern. Videos captured at a resolution of 648×482 pixels and 30 fps were collected and processed with Point Grey Fly Capture software that was provided with the CCD. Scatter pattern images were manually extracted from the video post-experiment and image-processing techniques such as background subtraction was applied.

5.3 Scatter collection angle

The scattered light path for the label-free microfluidic cytometer is shown in Figure 5.4(left). Referring to Figure 5.4(right), previously shown in Chapter 2, the incident beam (\vec{k}_i) travels across the channel in the z-direction and hits the cell or bead. Light scattered (\vec{k}_s) from a cell or bead propagates through layers of liquid, chip material,

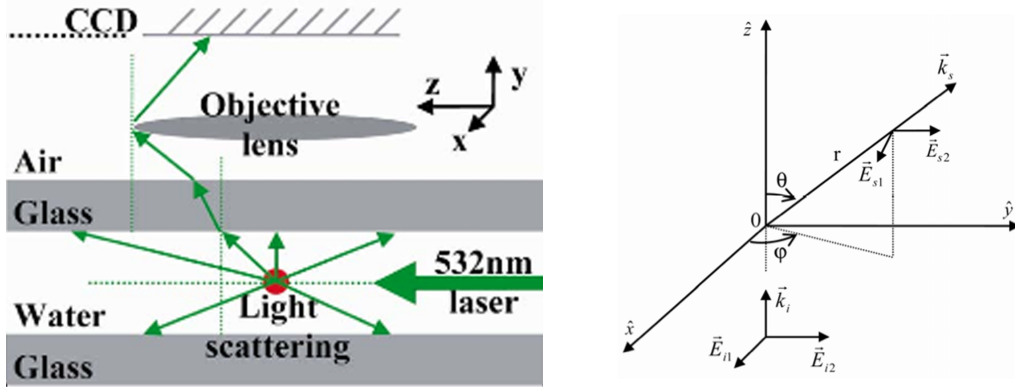


Figure 5.4: Left: A schematic diagram of the scattered light path in the microscope-based label-free microfluidic cytometer [27]. Right: Light scattering geometry for a single scatterer centred at the origin. The incident wave propagates along the $+z$ direction and the scattered wave has a polar angle of θ , and an azimuthal angle of ϕ . [39]

and air, before being collected by the CCD that is imaging light in the x - y plane at a cone angle centred around 90° from the incident beam.

Collected angular range can be calculated using the numerical aperture (NA) of the objective lens, and the index of refraction of the different media the beam penetrates. The 10x microscope objective attached to the CCD has a numerical aperture (NA) of 0.25 and this can be used to determine the collection angle, θ , to be 14.5° using the following equation:

$$NA = n \sin \theta, \quad (5.2)$$

where n is the index of refraction of the medium the objective or lens is used, in this case, air ($n = 1.0$).

However, this angle only applies when there is no change of medium from the cell being imaged and the objective. Unfortunately, in this case, scattered light has to pass through DI water, PDMS, and air, with the collection angle changing at each

interface due to Snell's law. Snell's law relates the angles of incidence and refraction when a wave passes through a boundary between two mediums with different indexes of refraction and is as follows:

$$\frac{\sin\theta_1}{\sin\theta_2} = \frac{n_2}{n_1}, \quad (5.3)$$

where θ_1 is the angle of incidence, θ_2 is the angle of refraction, and n_1 and n_2 are their corresponding indexes of refraction.

Working backwards, using Snell's law at each boundary gives me a final collection angle of 22° , centered around 90° (79° to 101° in the polar angle). Su also found a similar collection cone angle [27].

5.4 Bead scatter

Non-fluorescent polystyrene beads (F-13838, Molecular probes, Eugene, OR, USA) were used to mimic simple eukaryotic cells with no nucleus (e.g. red blood cells and platelets), or ones that have few mitochondria (yeast cell and platelets). Since there is a lack of interfaces, these beads, and the cells that they approximate, are weak scatterers with a prominent band structure. Because of their simplistic structure, beads are useful for visually relating 2D light scatter to Mie theory.

To attain scatter patterns from beads, the PDMS chip with the $200 \times 60\mu\text{m}$ (width \times depth) channel, Figure 4.7, was used. Other than the input and output from the main channel, all other inlets were sealed off with scotch tape. Flow speed varied and was controlled by hand with a disposable syringe. Laser light also varied depending on alignment and coupling into the waveguide. Gain settings were optimised for each cell so as not to saturate the image. Note that even though the laser has a TM or transverse magnetic mode, the incident light is not necessarily perpendicularly

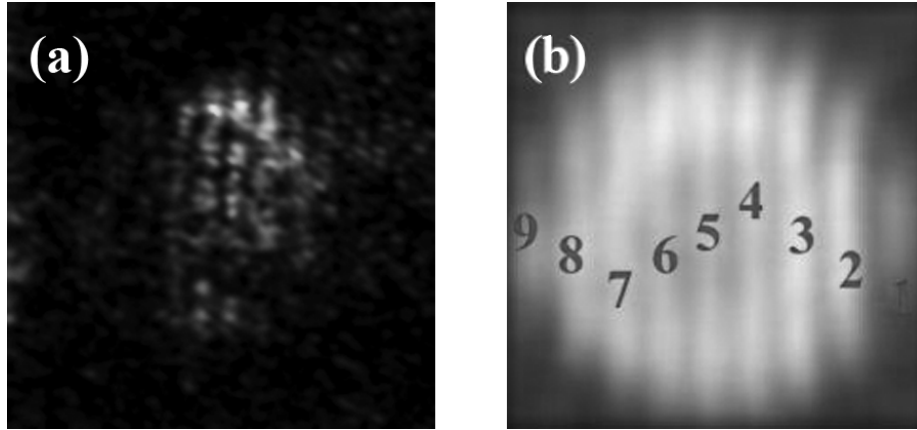


Figure 5.5: Comparison of polystyrene bead scatter patterns from (a) original data, diameter $15\ \mu\text{m}$, (b) Su's 2011 paper [27], diameter $9.6\ \mu\text{m}$.

polarised as it has to pass through a fibre and a rectangular PDMS waveguide. Thus, for Figure 5.6 and Figure 5.7 below, I assumed that there was a partial perpendicular and partial parallel component to the polarisation of the beam by taking the average of the two intensity plots. However, this assumption is very crude and detailed analysis should be performed in the future. A good starting point would be papers by Marcatili [83] and Renner [84], who both supply useful information regarding changes in polarisation for rectangular and optical waveguides.

The scatter from a polystyrene bead is shown in Figure 5.5. The band structure seen here can be related back to Mie theory described in Chapter 2.3. Here, I have modified the Bohren-Huffman C code to compute the angular scatter intensity using Mie theory. This code is a translation of the originally published Bohren and Huffman's Fortran code [40] and the modifications that I made to it is documented in Appendix A.2. The Mie scatter solution from a 532nm incident beam on a $9.6\ \mu\text{m}$ polystyrene bead ($n=1.59$) in PBS ($n=1.334$) is shown in Figure 5.6, where the scattered intensity is plotted in arbitrary units over the angular range of 0° to 180° . This graph would be comparable to a 1D line plot profile of the collected scatter image

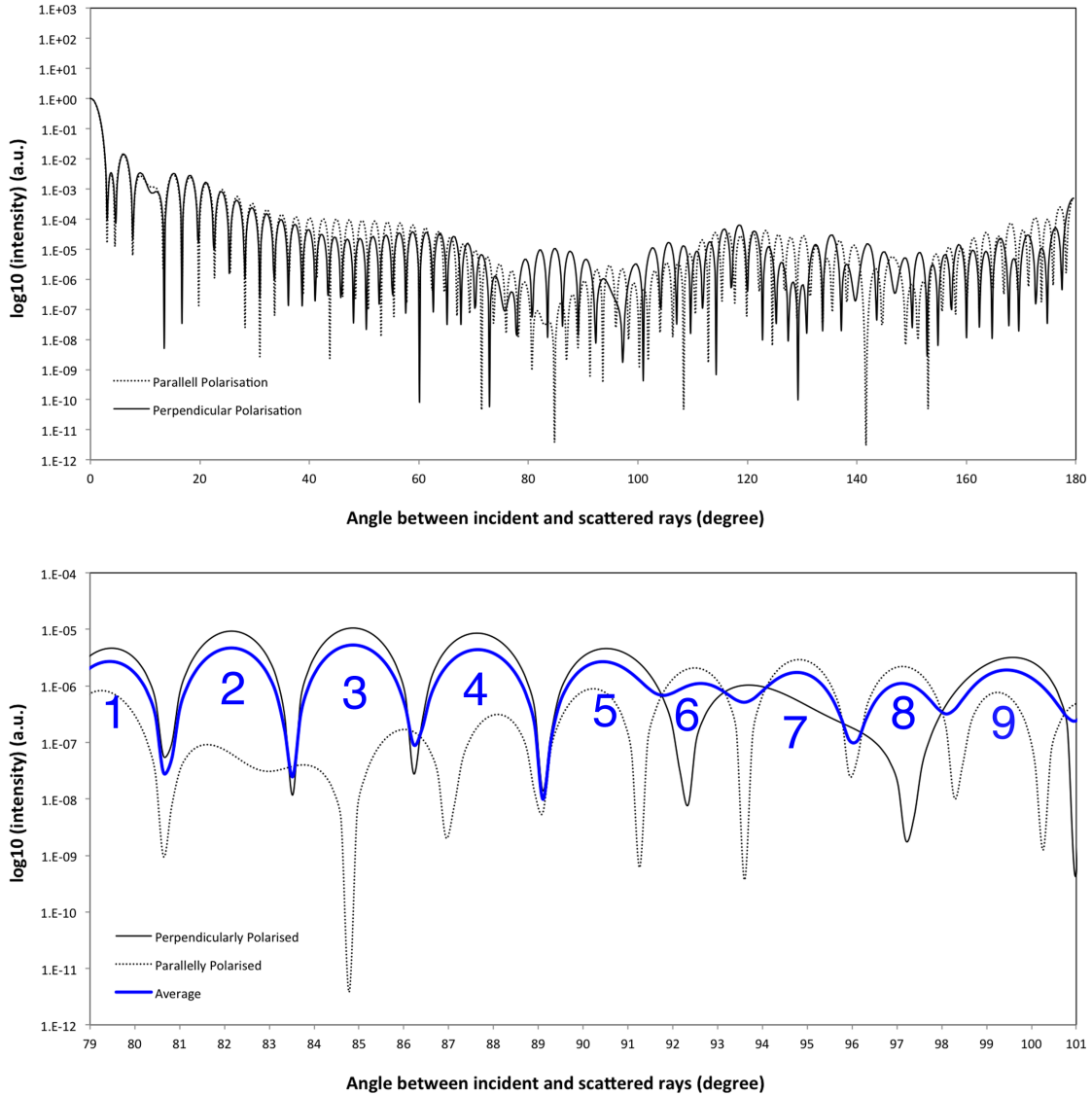


Figure 5.6: Mie solution to scatter from a 532nm incident beam on a $9.6\mu\text{m}$ polystyrene bead ($n=1.59$) in PBS ($n=1.334$). For both perpendicular and parallel polarization. Top: For angles 1 to 180° . Bottom: For angles 79 to 101° (22° cone angle), with average polarization showing 9 peaks.

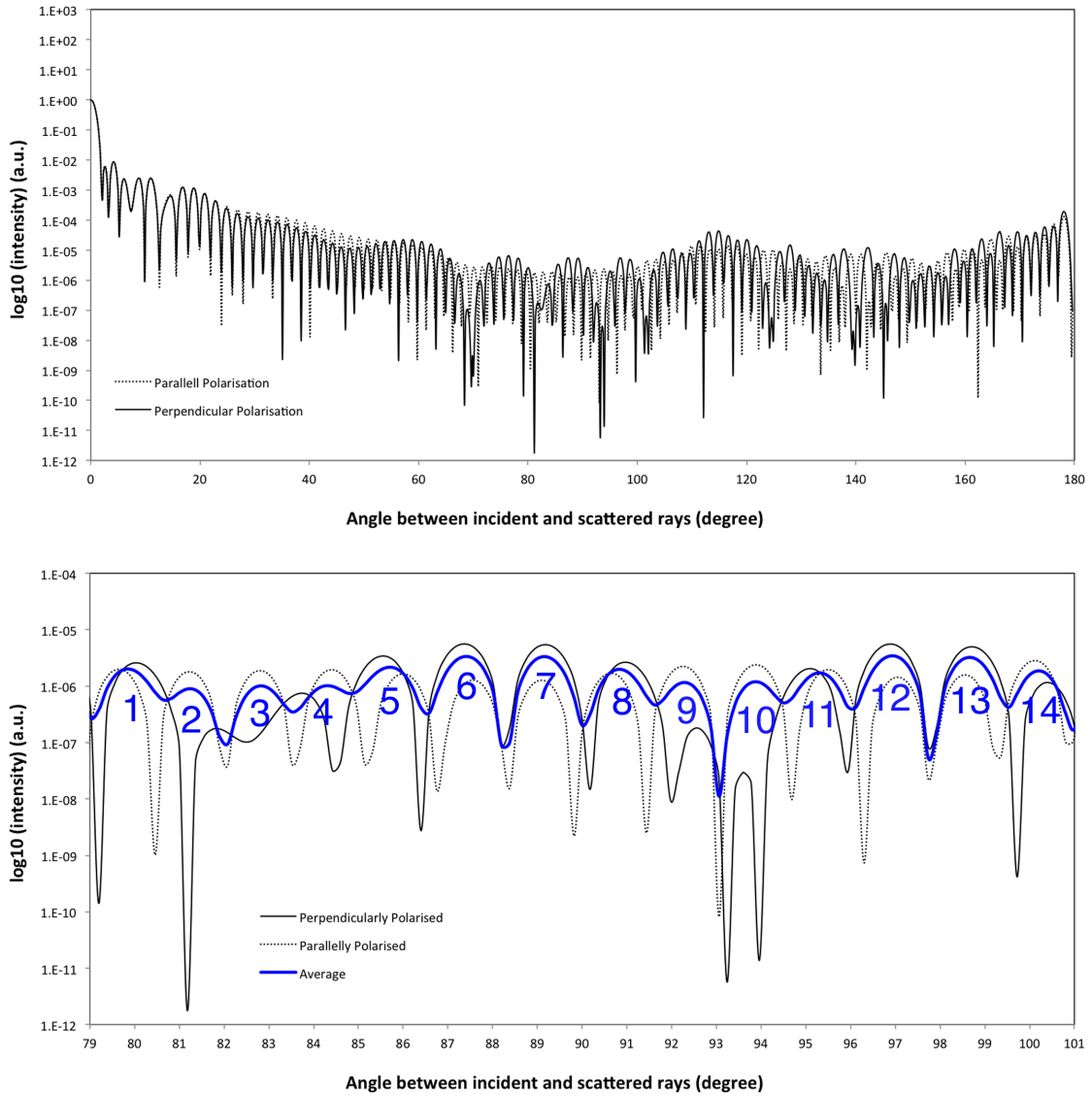


Figure 5.7: Mie solution to scatter from a 532nm incident beam on a $15\mu\text{m}$ polystyrene bead ($n=1.59$) in PBS ($n=1.334$). For both perpendicular and parallel polarization. Top: For angles 1 to 180° . Bottom: For angles 79 to 101° (22° cone angle), with average polarization showing 14 peaks.

along the x-axis. In the collected cone angle of 79° to 101° , there are 9 observable bands in the experimental data collected by Su in Figure 5.5(b). Correspondingly, there are also 9 maximums (or peaks) in the Mie scattering graph when an average of the perpendicular and parallel polarised intensities were taken. Su [39, 27] found that there was a correlation between the size of the bead and the number of bands seen. The exact number of bands depends on the cone angle of scatter being collected.

For a $15\mu\text{m}$ bead, we expect a larger number of bands than the $9.6\mu\text{m}$ bead. Mie scatter intensity plots for a $15\mu\text{m}$ bead, plotted in Figure 5.7, show that for a mixed polarisation (50% parallel and 50% perpendicular), we should expect 14 bands. Unfortunately, as seen from the scatter of a $15\mu\text{m}$ bead in Figure 5.5(a), the SNR is too large to view all the bands and count them; the resolution of the image is also lacking.

This low resolution and high SNR is due to the chip design. The current PDMS chip scatters internally as mentioned previously in Section 4.1.2, raising the background and drowning out scatter from the cell or bead. Furthermore, the image could not be sufficiently defocused due to scatter from the channel walls, which overlaps and saturates the cell or bead scatter previously mentioned in Section 4.3. This is a recurring problem that is evident in the following biological cell scatter data.

5.5 Biological cell scatter

Scatter patterns are shown below for normal cell lines CD34+, leukemic cell lines NC-37, HL-60, and KG-1a, as well as *E. coli* DH5 α . A similar setup and procedure as Section 5.4 was used. For biological cells, the mitochondria dominates the band pattern. Thus, we see speckles instead of bands. Therefore, a simplistic 1D line profile plot of the intensities over a range of angles ceases to give meaningful data.

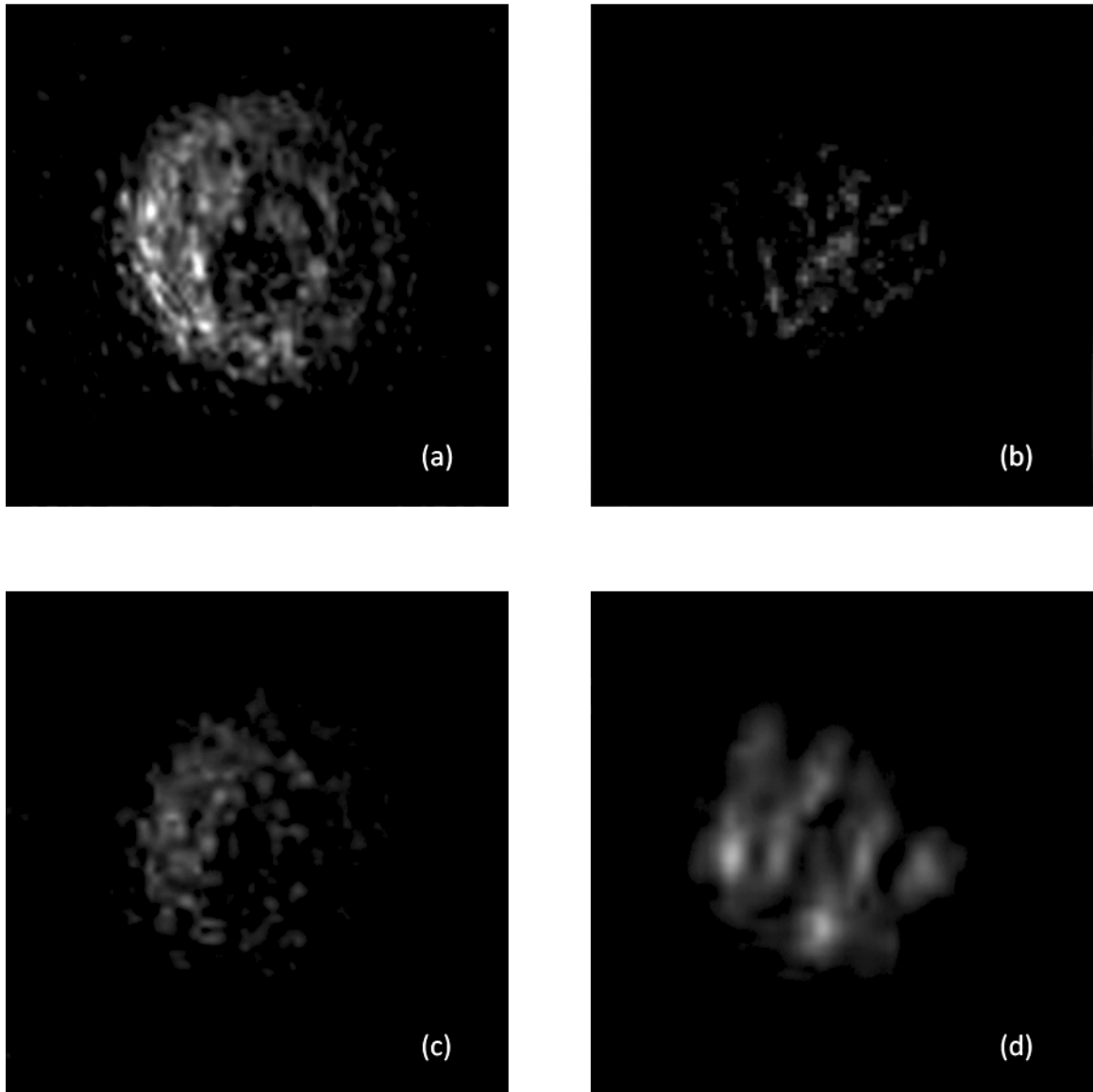


Figure 5.8: Scatter patterns from (a) CD34+ (b) NC-37 (c) HL-60 (d) Kg-1a.

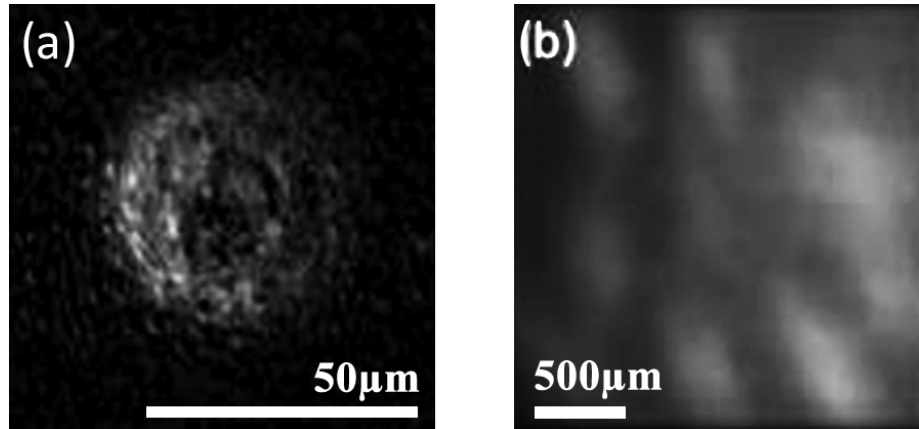


Figure 5.9: Comparison of CD34+ scatter patterns from (a) original data (b) Su's 2011 paper [26]

Scatter for CD34+, Figure 5.8(a), was strong and easy to see. It was also dominated by small scale 2D structures, indicating strong mitochondria presence in the cell. However, these results show a slight ring structure, which suggests that the image had not been defocused enough for us to only see Mie scattering. Comparing this data to the CD34+ scatter attained by Su [26], shown side-by-side with the data presented in this thesis in Figure 5.9, we can clearly see by the 500μ size marker on the image that we have not defocused enough. This was due to the constraints of the microfluidics chip and high background scatter. In fact, 500μ exceeds the width of the PDMS chip used and it is unlikely that I will be able to attain similar defocused data with the current chip as scatter from the channel walls would saturate any scatter from the cell. However, the slightly elongated speckles seem consistent with Su's data.

NC-37, Figure 5.8(b), was not as easy to see. This large lymphoblast is a weak scatterer that showed a prominent band structure. This can probably be explained by its simple internal structure with smaller or less mitochondria [81] as compared to CD34+. I was unable to find previously published data on this cell for comparison.

HL-60 in Figure 5.8(c) has a scatter pattern consisting of numerous small speckles. As it is a leukemic cell this discovery is consistent with the findings in [26], where malignant Jurkat (acute T-cell leukemia) cells had a large speckle number and small average cross sectional area of each speckle, in contrast to the healthy CD34+ cells with a small speckle number and large cross sectional area. This difference in scatter pattern was attributed to the distribution of mitochondria within the cell, which is aggregated in normal cells but randomly distributed in malignant cells. In another paper, Su [27] attained scatter from a healthy myeloid precursor cell and this is shown in Figure 5.10. Note that it was not specified which stage of differentiation the cell was at (promyeloblast, myeloblast, or something else) only that it expressed the CD33 marker. With numerous small speckles, this myeloid precursor cell is similar to the HL-60 scatter patterns found in this thesis and was shown to be distinguishable from CD34+ scatter. Similar to the Jurkat cells, the mitochondria distribution in the myeloid precursor cell was assumed to be randomly distributed. This begs the question: is it possible to distinguish between a leukemic myeloid precursor and a normal myeloid precursor? More work has to be done to determine this.

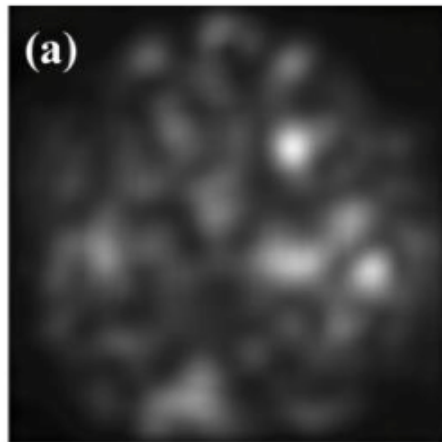


Figure 5.10: Scatter pattern from a healthy myeloid precursor from [27].

Figure 5.8(d) shows Kg-1a, which like HL-60 is also a myeloid precursor cell that is leukemic. However, being a myeloblast, it is slightly more mature than promyeloblast HL-60. The scatter from Kg-1a looks very different from HL-60, with a small number of large speckles as opposed to numerous small speckles. This goes against the assumption that leukemic cells would all have randomly distributed mitochondria resulting in a large number of small speckles. This change in pattern could be caused by the granules in the cytoplasm of myeloblasts (i.e. Kg-1a), which is lacking in promyeloblasts (i.e. HL-60). It might be interesting to find out the index of refraction of these granules and see how they compare to the impact of mitochondria distribution on a cells scatter pattern. It would also be useful to study non-leukemic, or healthy, versions of a promyeloblast and a myeloblast. Unfortunately, no previous study has been done on the scatter patterns of this type of cell.

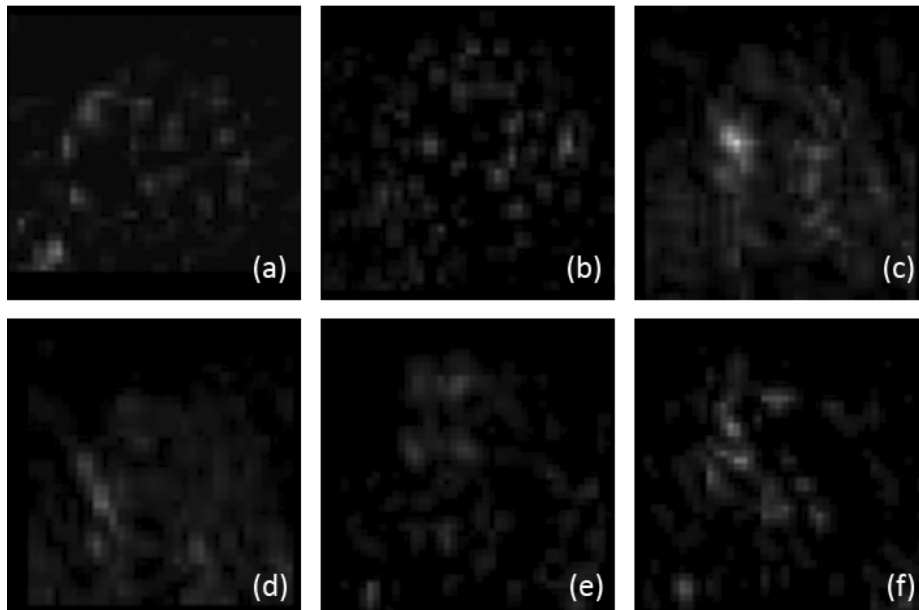


Figure 5.11: Scatter patterns from *E. coli* DH5 α .

Scatter from *E. Coli* was extremely difficult to attain with the current setup due to their small size and lack a strongly scattering internal structure. When the image

is defocused, much of the scatter is smeared out giving me data that is less than ideal, Figure 5.11. Since E. Coli has a rod like shape, its scatter will also depend on the orientation of the cell. In Figure 5.11(c) and (d), as the image was not defocused enough, there are concentric elliptical rings that suggest the rod-shape of the bacterium. This is beneficial as one could perform two levels of defocusing to determine the shape of the cell first, then its scatter pattern second, to detect bacteria in blood.

As can be seen from the result in this section, the background noise is too high to produce good data. However, while the current scatter patterns are noisy, they do resemble previously published data (where available).

5.6 Recommendations

As seen from the comparisons of my data with that in literature, it is clear that scatter images with higher resolution and lower SNR are necessary to differentiate cells by their scatter pattern. Steps have to be made to smoothen the channel and eliminate all features that cause unnecessary scatter. The internal scatter of the PDMS also has to be dealt with by either changing the fabrication recipe or the material of the chip.

A channel width of 200 μm is still too narrow for the walls to not interfere with the cell pattern. Thus, a wider channel has to be implemented with hydrodynamic focusing to force the cells in the middle of the channel away from the walls. This realisation lead to the creation of the 300 μm chip, Figure 4.8, and the exploration of making a glass to PDMS chip. However, this chip was not tested and was thus not included in the scope of this thesis. With more changes, the PDMS chip can be improved for the label-free cytometer.

Chapter 6

Customised flow control system

One of the most integral parts of a microfluidic system is the ability to reliably control the pressure and speed of flow within the channel. This calls for a steady-flow pump system with no flow oscillation and a fast response switching system for cell sorting. However, commercial systems explored in Section 3.3 are costly and the response time typically are tens of milliseconds or longer.

In this section, I list the materials, setup, and procedure of the customised flow control system. I then calibrate it to determine the speed in the channel for a given input pressure. For cell sorting, a solenoid pump is integrated and the response time is experimentally determined and evaluated. Lastly, hydrodynamic focusing is implemented with this customised flow control system.

6.1 Materials and cost

The principle is simple. An airflow pump is connected to a sealed container containing the liquid that is to be pumped into the channel. As the air pressure is increased, the contained liquid is forced up a tube and into the microfluidic channel. To imple-

ment this I used materials that were readily available from the University of Alberta BioScience store. An ideal pump system would be smaller and more tightly sealed but this worked well as an initial prototype. The materials used are shown in Table 6.1. Table 6.2 shows the materials and costs for a fast switching side flow system that can be added to a pressure driven pump to enable cell sorting.

Table 6.1: Materials & costs for a pressure driven pump

Supplier	Part No.	Item	Qty	Cost
BioSci Store	gl0740	Filtering Flask 125mL	1	\$ 19.66
BioSci Store	st250	Rubber Stopper 5	1	\$ 0.30
BioSci Store	tp010	Tygon Tubing, ID $\frac{1}{16}$ " , OD $\frac{1}{32}$ "	1	\$ 0.13
BioSci Store	tl070	Rubber Tubing, ID $\frac{1}{4}$ " , OD $\frac{1}{16}$ "	1	\$ 0.92
Cole-Parmer	EW-68825-18	Marsh Bellofram Air regulator, $\frac{1}{4}$ " NPT(F), 0 to 2 psi	1	\$ 73.34
Cole-Parmer	EW-68930-03	Ashcroft Low pressure gauge, 0 to 60" H ₂ O	1	\$ 64.75
Swagelock	B-400-7-4	Swagelock Tube fittings, $\frac{1}{4}$ " NPT	2	\$ 14.56
			Total	\$173.66

Table 6.2: Materials & costs for a cell sorting side-flow pump

Supplier	Part No.	Item	Qty	Cost
Swagelock	B-400-7-4	Swagelock Tube fittings, $\frac{1}{4}$ " NPT	2	\$ 14.56
N.A.	V5D23130	Skinner Solenoid valve, V5 series	1	\$150.00*
Digikey	CC1001-ND	Crydom Solid state relay D1210	1	\$ 41.78
			Total	\$206.34

* Pricing for the Skinner solenoid valve is approximate as the product is no longer available on the market. However, a similar one can be purchased from Parker at the cost of \$150.

Information in both tables were gathered from manufacturers website or from email quotations and are up-to-date as of Jan 1st, 2013. A pump for one channel costs approximately \$175, and this value can be multiplied if more channels are required.

Since there are 3 distinct flows (main flow, sheath flow, and side flow), at most three pumps are used in conjunction, with one cell sorting addition. For automated functionality and integration with the CCD, the sorting system can be connected to a computer via a data acquisition device (DAQ) and LabVIEW (National Instruments, Austin, TX, USA) can be used to analyse input from the camera and trigger the pump as implemented in Section 6.5.

6.2 Setup and procedure

An overview of how the pressure driven pump connects to the existing optical system is shown as a functional block diagram in Figure 6.1. The shaded blocks are components of the pump system that will be discussed in this section.

Nitrogen gas from the lab supply was connected to a small air pressure regulator (960-115-000, Marsh Bellofram, Newell, WV, USA) and gauge (25-1490-A-02L-60iW/KP-TUZZ, Ashcroft, Stratford, CT, USA) that would step the pressure down and allow me to adjust the pressure in the range of 0 to 140 mbar. This was connected via PVC tubing to a natural rubber tubing that was stretched over the arm of a glass 125mL filtering flask (BioSci Store, University of Alberta, Edmonton, AB, Canada). The interface between the PVC tubing and rubber tubing was reinforced with zip ties and twisted wires to ensure no leaks. A hole was punched in the rubber cork of the flask and a Tygon tube (C-Flex RK-06422-00, Cole-Parmer Instrument Company, QC, Canada) was threaded through and sealed with epoxy to ensure a leak-free system. The tube was then pressure fit into a pipette tip (02-707-500, Fisher Scientific, ON, Canada) that was then connected to the PDMS chip. This setup is shown in Figure 6.2.

Note that the valve has no interaction with the liquid cell samples, thus isolating

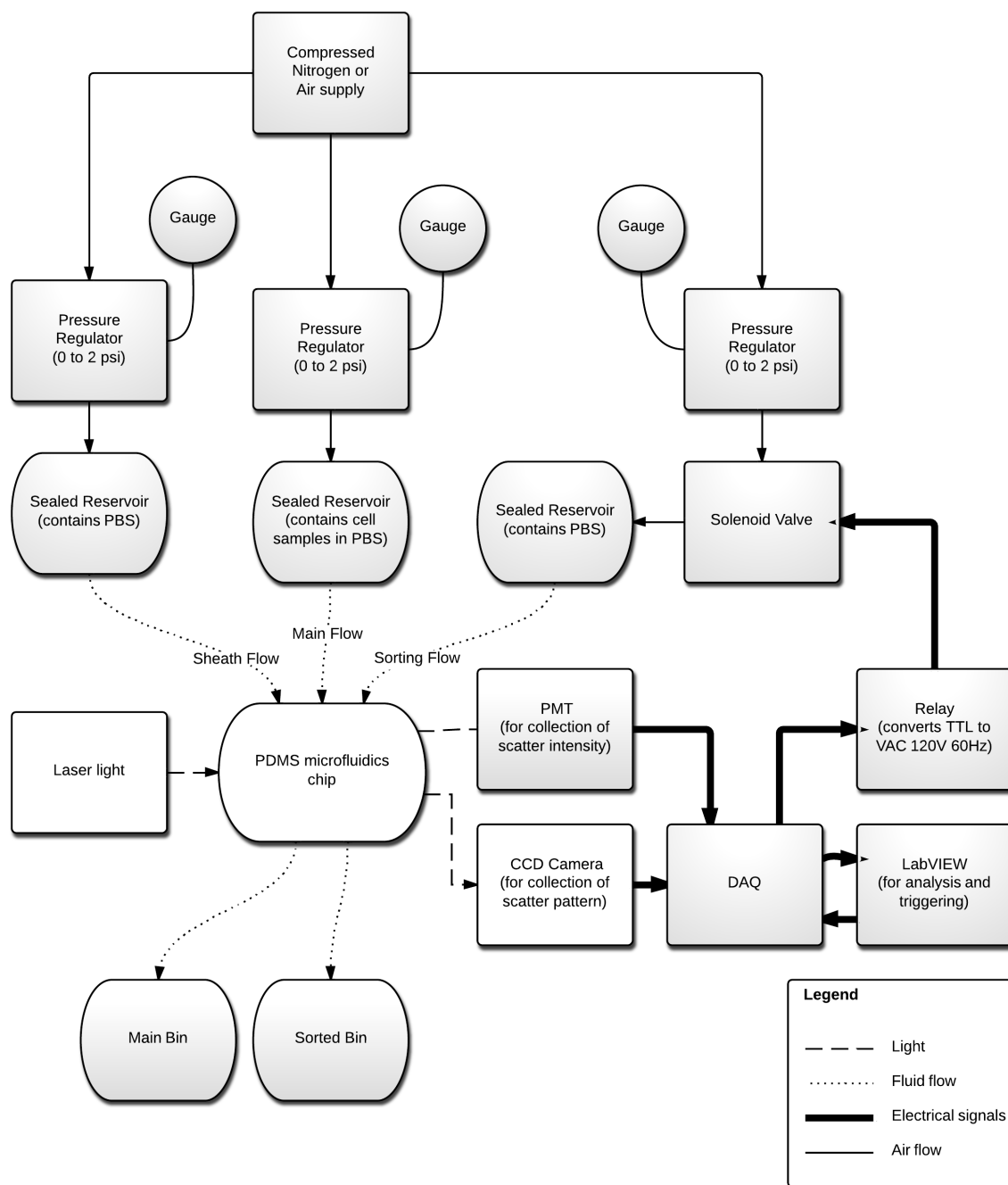


Figure 6.1: Functional block diagram for the pump system and how it interfaces with the optical system.

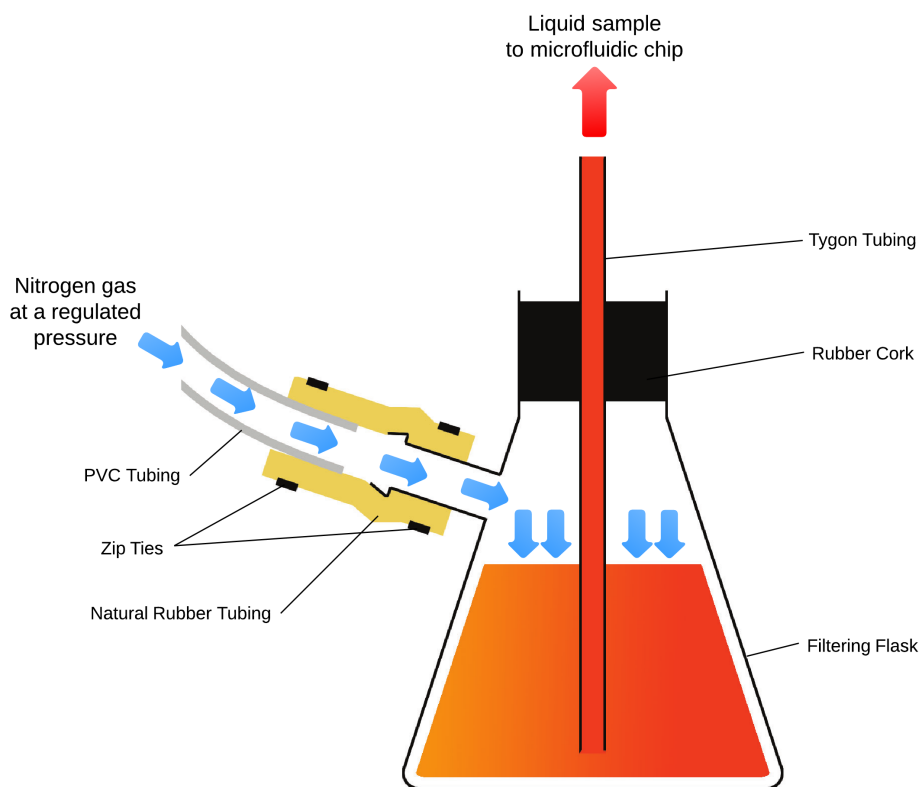


Figure 6.2: Schematic for pressure driven pump flask setup

the pump system from the samples. To be safe, an air filter could be added to the nitrogen air system to prevent back-flow of aerated sample. The gauges were calibrated by raising the Tygon tubing and measuring the difference between the height of the water in the flask and in the raised tube.

This system was duplicated two times to provide flow to the (1) Main channel, and (2) Sheath flow channels for hydrodynamic focusing or for side flow sorting.

To calibrate the pump system and determine the flow speed when the pressure is changed, Section 6.3, the fluid output of the chip was studied. Only one pump was used in this experiment. All inlets other than the main channel were sealed with scotch tape and a Tygon tube was attached to the main outlet. The tube was pressure fit into a pipette tip and this was clamped vertically into place so liquid

dripped slowly out when pressure was applied. A CCD camera (DMK31BF03, Imaging Source, Charlotte, NC USA) with a 5x microscope objective was mounted on a XYZ translation stage and used to view the droplets. The CCD was connected to a computer where videos of the drops dripping were recorded at a frame rate of 30fps. A light was placed behind the drop to provide contrast. To ensure there were no pressure differences, the height of the water in the flask was kept in line with the PDMS chip and the droplet output.

For hydrodynamic focusing tests, Section 6.4, two pumps were used. One was connected to the main inlet to provide main flow and the other to provide sheath flow. To visualise the two different flows, DI water was used in the main flow and DI water with blue food colouring was used for the hydrodynamic focusing. Instead of the CCD previously used in Chapter 5, a digital colour CCD camera (WDAC-5700C, Micro Video Products, ON, Canada) was used to view the detection area. A hole was drilled in the stage holding the PDMS chip and a white LED was used to light up the viewing area from below. It made it easier to distinguish between the green laser light, colourless main flow, and blue side flows.

For the side flow sorting system, as described previously in Section 3.3, cells would be pushed from the main channel into a side bin when the side flow is activated. A solenoid valve (V5D23130, Skinner, no longer in business) was introduced in to the system prior the filtering flask. The normally closed valve was trigger with a solid-state relay (D1210, Crydom, San Diego, CA, USA) that could open and close the nitrogen flow when +5V was applied. This relay was then fed into a DAQ (NI USB-6008, National Instruments, Austin, TX, USA) so it could be triggered by LabVIEW.

To calculate response time in Section 6.5, a PMT (R2949, Hamamatsu, Hamamatsu City, Shizuoka, Japan) was placed under the detection region of the chip and interfaced via the same DAQ. When a cell flowed past the detection region of the

microfluidics channel, it triggered the PMT, which fed a signal to LabVIEW. The software in turn sent out a +5V signal to the relay and solenoid valve. It also triggered a light emitting diode (LED) indicator light. This switched on the side flow, altering the path of the cell and sorting it out from the main population. After an adjustable delay (that depended on the speed of flow), LabVIEW switched off the solenoid valve and returned flow to normal.

When setting up the experiment, it is important to ensure that there are no bubbles trapped anywhere in the system as the pressure in the system would not match that shown at the gauge. To minimise the waste of cell samples, the following method was used to connect the pump system to the chip. Filtered DI water or PBS was placed in all the flasks. Starting with the main flow, pressure was increased to 12.5 mbar and the pipette tip was inserted into the PDMS chip. The pressure was increased to 100 mbar to quickly fill chip. When beads of water collect on the outputs of the chip, the pressure on the main channel was reduced to 0 mbar. The sheath flow (and/or side flow, if used) was increased to 12.5 mbar and the pipette tip was inserted into the chip through the collected bead of water, taking care not to introduce any air bubbles in the system. There should not be any bubbles of air in the tubing. Pressures were then adjusted and to ensure everything was flowing smoothly. At this point, I checked to make sure that the optical setup of the chip and the computer interfaces were aligned and running as planned. Main flow was turned down to 0 mbar and detached from the PDMS chip. Remaining water in the flask was replaced with suspended cell samples and the tube was reattached to the chip without bubbles using the precautions previously mentioned. Pressures were readjusted for the experiments.

6.3 Pressure to flow speed calibrations

Calibrations for the pressure driven pump system are required to determine the average speed of flow within the microfluidic channel when a particular pressure was applied. One method of attaining this data is the method used by [75], where the pump was set to a particular pressure and the output was left to drain into a beaker for a known amount of time. The volume of liquid in the beaker was then weighed. Knowing the cross-sectional area of the channel, the mass of liquid accumulated in the beaker, the density of the liquid, and the time, the average flow speed can be calculated with

$$FlowVelocity = \frac{m}{\rho At} = \frac{V}{At} \quad (6.1)$$

where m is the mass of the liquid collected, ρ is the density of the liquid, t is the time, and A is the cross-sectional area of the channel.

However, this method proved to be inconsistent at lower speeds as the pump had to be left running for a longer time to collect enough liquid volume for a measurement.

Therefore, I decided to calibrate the pressure driven pump by taking a video of the output droplets when set at a particular pressure. Since the tubing used was kept consistent, the volume of the suspended droplet right before it fell should be the same each time provided the surface tension of the liquid and the diameter of the dropping tip was not changed. With a frame rate of 30 fps, the video would give me the time taken for each drop to the closest $\frac{1}{30}$ sec. The volume of the droplets are dependant on the setup and if unmodified, should remain constant regardless of the pressure. Two different methods of calculation was used to find the volume of the droplet (1) Spherical Volume Method, and (2) Pendant Drop Method.

First, I calibrated the video with an unmounted 400 μm diameter precision pinhole aperture (39-881, Edmund Optics, Barrington, NJ, USA). This pinhole aperture was

viewed in focus with the CCD and microscope objective. A screenshot was taken and the $400 \pm 5 \mu\text{m}$ diameter was found to be $93 \text{ pixels} \pm 10 \text{ pixels}$. This number is used in the following sections.

6.3.1 Spherical volume method

The spherical volume method assumes that the drop is perfectly spherical when it is falling. Therefore the volume of the droplet can be calculated by measuring the radius of the drop as it is falling and using the volume of a sphere equation,

$$V = \frac{4}{3}\pi r^3 = \frac{\pi d^3}{6} \quad (6.2)$$

where r is the radius of the drop and d is the diameter. Flow speed can then be found using Equation 6.1.

To determine the radius of the drop, I analysed the videos to find one which contained the drop almost detached from the tube as shown in Figure 6.3. I was unable to capture a video of the drop free falling as the frame rate of the CCD was not high enough. Unfortunately, the CCD was unable to capture the entire droplet due to a magnification that was too large. Thus, the bottom quarter of the droplet is cut out of the image. To solve this, I superimposed a circle over top of the image to determine the diameter of the assumedly spherical drop as it is falling. I then took an average of collected diameters, which resulted in an average diameter of 470 pixels or $2022 \mu\text{m}$. This yields a volume of $4.3 \pm 0.5 \text{ Smm}^3$ which can then be used to find the average velocity of the liquid.

This method does not seem very accurate as it assumes that the droplet is spherical as it falls, which is not the case as droplets will be deformed by gravity as it falls. Oscillations of the "spherical" volume also prevents an accurate reading of the

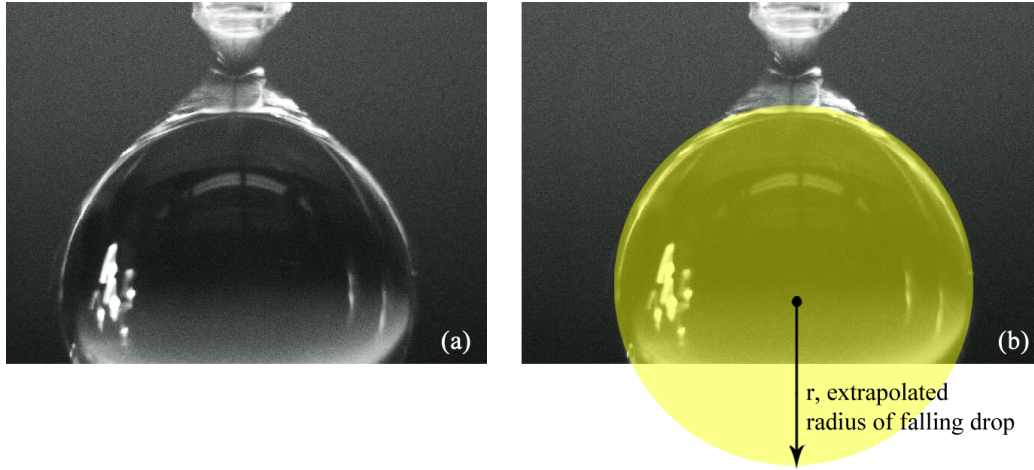


Figure 6.3: Falling droplet that we assume to be spherical (a) unmodified image (b) modified image showing the extrapolated droplet shape and length measured to determine radius.

droplet's diameter. A large error of ± 20 pixels was applied to the diameter of the falling droplet due to this reason.

6.3.2 Pendant drop method

Drop shape techniques are widely used to calculate surface tension measurements in industry. The pendant drop method makes use of Tate's Law where the droplet is assumed to be at equilibrium until it finally becomes unstable and detaches from the system. Thus, the shape of the droplet depends on equal and opposite gravity and surface tension forces,

$$F_g = F_\sigma \quad (6.3)$$

$$mg = 2\pi r_w \sigma \quad (6.4)$$

where g is gravity, m is mass of the droplet, σ is the surface tension, and r_w is either the inner or outer radius of the dropping tip depending on the wetting behaviour of

the liquid [85]. For small drops where there is no "neck" in the equilibrium shape, r_w can be assumed to equal r_0 , the smallest width of the droplet or the "neck". This also assumes that there is no excess liquid sticking to the tube when the drop has fallen.

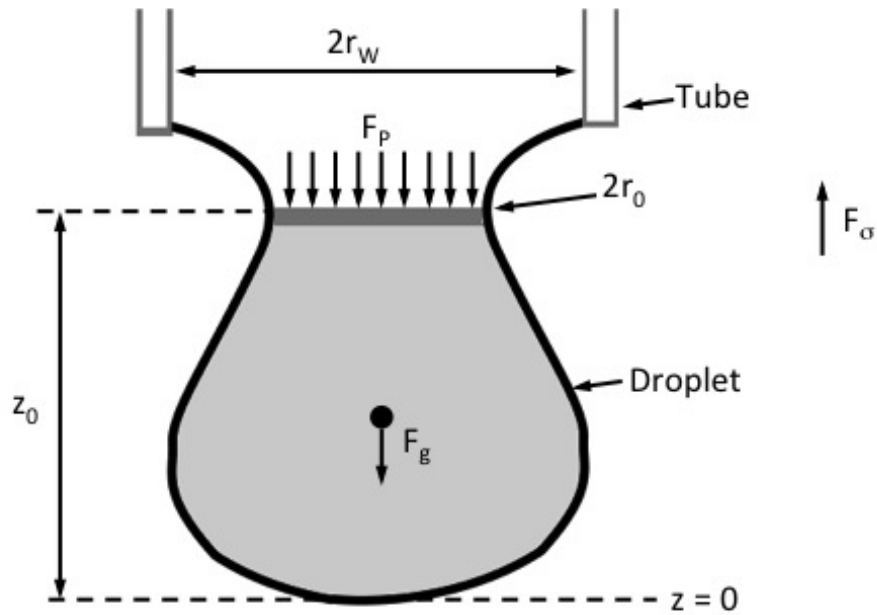


Figure 6.4: Geometry of the pendant drop, where F_g is the gravitation force, F_p is the force due to the pressure in the tube, F_σ is the force due to surface tension.

However, calculations just using Tate's law proved to be much too low compared to the spherical volume method. Garand et al. [85] explains that Harkins correction factor has to be introduced to make Tate's law more accurate. This works by introducing a third force to the equation- the pressure pushing downwards on the drop, p . Therefore, the sum of forces, illustrated in Figure 6.4 now becomes

$$F_g + F_p = F_\sigma \quad (6.5)$$

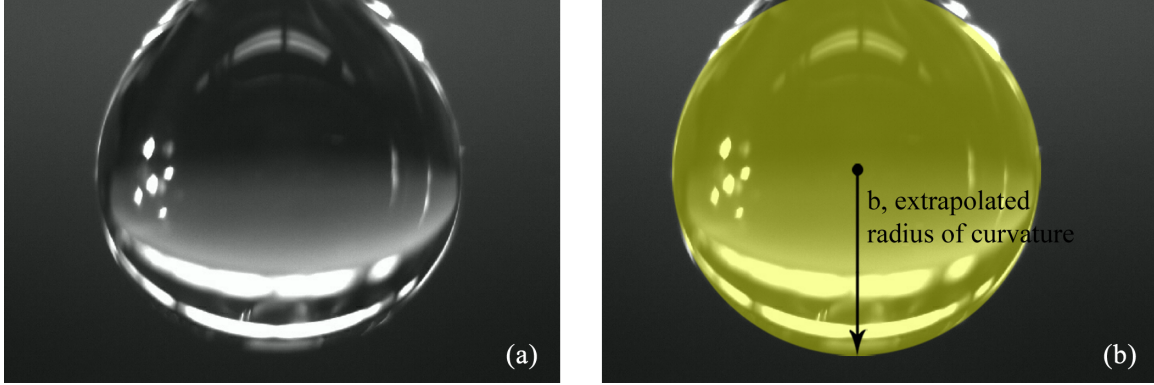


Figure 6.5: Estimating β , radius of curvature, from (a) unmodified image (b) modified image showing the extrapolated droplet shape.

The downward pressure acting on the droplet is dependant on the length of the droplet, z_0 [85]. Letting b be the radius of curvature at $z = 0$ (bottom of the drop), and ρ is the density of the liquid, it is

$$F_p(z_0) = \pi r_0^2 \left(\frac{2\sigma}{b} - \rho g z_0 \right) \quad (6.6)$$

With this, Equation 6.5 can be rewritten and solved for mass.

$$mg + \pi r_0^2 \left(\frac{2\sigma}{b} - \rho g z_0 \right) = 2\pi r_0 \sigma \quad (6.7)$$

$$m = \frac{\pi r_0}{gb} (2\sigma b - 2\sigma r_0 + \rho g z_0 r_0 b) \quad (6.8)$$

From here, the volume of the droplet can be calculated using the density of the liquid.

$$V = \frac{m}{\rho} \quad (6.9)$$

Flow speed can then be found using Equation 6.1.

Values b , z_0 , and r_0 were determined experimentally by extrapolating the droplet's

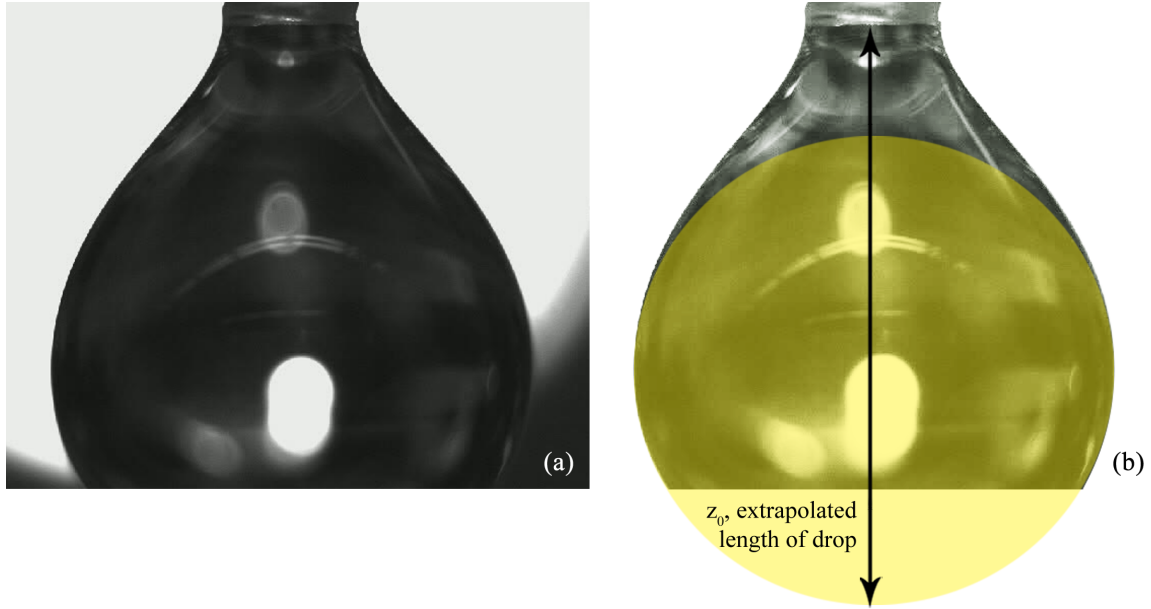


Figure 6.6: Estimating z_0 , length of droplet, from (a) unmodified image (b) modified image showing the extrapolated droplet shape.

shape from images extracted from the video the frame before the droplet falls. However, as mentioned previously, the video was unable to capture the entire droplet due to incorrect magnification. Thus, a circle is superimposed on each of the droplets to extrapolate the shape of the droplet. This is shown in Figure 6.5 and 6.6. The inside diameter of the pipette tip, $2r_0$, was found to be 99 ± 10 pixels. The raw pixel numbers and their corresponding numbers in microns for the other experimentally determined constants are recorded in Table 6.3. Since the droplets are the same size regardless of the pressure, an average number for β , z_0 , and r_0 was used to calculate a fixed mass for all points on the graph.

With a $\sigma = 7.28e - 2N/m^2$ [77], $\rho = 998kg/m^3$ [77], and $g = 9.8m/s^2$, the volume for a droplet is calculated using Equations 6.8 and 6.9 to be $8.23 \pm 1.14 mm^3$.

Table 6.3: Raw data for pressure to flow calibrations

Experimentally derived constant	Dimensions (pixel)	Dimensions (μm)
Pinhole aperture	93 ± 10	400 ± 5
b	238 ± 5	1020 ± 113
z_0	570 ± 10	2450 ± 269
r_0	49.5 ± 5	213 ± 32

6.3.3 Results

The experiment was carried out by pumping DI water through the main channel of the 200 μm PDMS to PDMS chip. Results for both methods, spherical volume and pendant drop, are plotted in Figure 6.7. Raw data can be found in the appendix. Five sets of data was collected for each pressure, and a range of pressures from 0 to 115 mbar were tested. Propagation of errors was calculated using standard deviations. As seen from Figure 6.7, the data for each pressure point almost fully overlaps, indicating high experimental precision. This test was also carried out for the 60 μm PDMS to PDMS chip, and this is plotted with modified experimental data from Islam's thesis [75] in Figure 6.8. Islam measures the average flow speed by draining the output of the chip into a beaker and finding the difference in mass after a fix amount of time. However in his experiment, Islam used both main and sheath channels, pumping the same pressure through both. Thus, to make his data accurately match the data

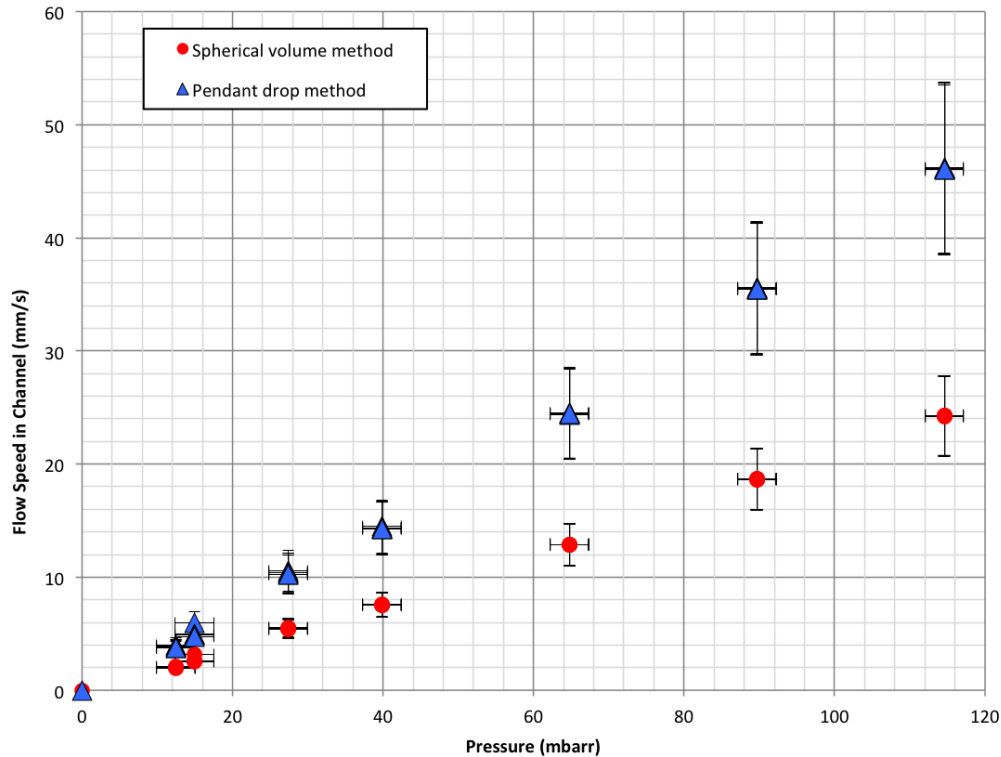


Figure 6.7: Average flow speed of DI water in the main channel of a $200\ \mu\text{m}$ wide PDMS chip as a function of the applied pressure

presented in this thesis, I modified Islam's data by taking a sum of both pressures and plotting this as the overall pressure in the channel.

Comparing the two graphs, we can see that the $200\ \mu\text{m}$ wide chip has faster flow speeds in the channel as compared to the $60\ \mu\text{m}$ wide chip. They also seem to fall along a linear trend. This is expected as a smaller surface-area-to-volume ratio would result in less reliance on fluid interactions with the hydrophobic PDMS channel surface. There is also more throughput at the same pressure, resulting in high speeds. This higher flow speeds in the $200\ \mu\text{m}$ wide chip is not ideal as (until it is optimised for faster flow) the current label-free cytometer setup requires very low speeds to detect scatter. However, the larger channel is integral for the reduction of noise and

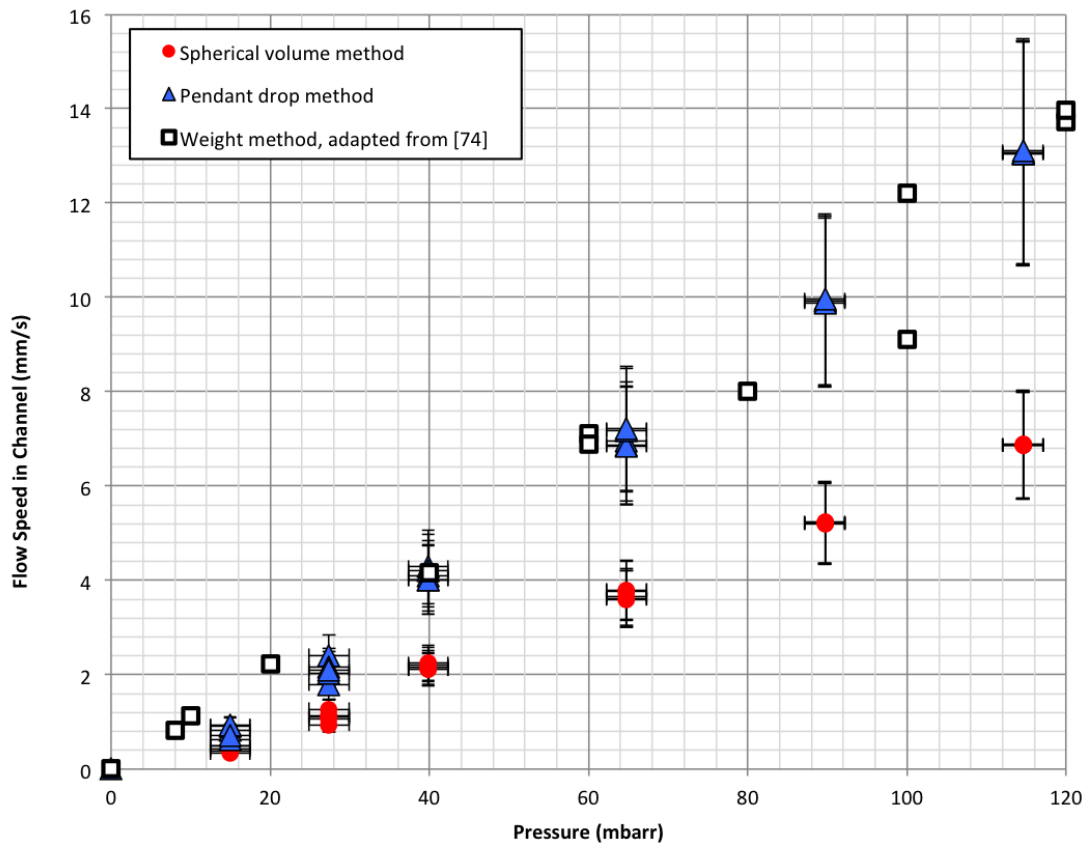


Figure 6.8: Average flow speed of DI water in the main channel of a $60 \mu\text{m}$ wide PDMS chip as a function of the applied pressure, with adapted data from [75]

thus a trade-off has to be accepted. The 200 μm wide chip is still able to reach flow speeds of 5mm/s but at a lesser resolution as compared to the 60 μm wide chip.

Looking at the different methods used to calculate the flow speed, the spherical volume method gives noticeably lower flow speeds as compared to the pendant drop method. This underestimation of volume may potentially be because there is some liquid that is left clinging to the tubing instead of falling with the droplet. Since only the spherical part of the drop is being considered, this would explain why the radius of the falling drop is less or comparable to b used in the pendant drop method as some of the liquid is not counted and left on the dropping tip. Furthermore, the droplet are moving downwards as it falls, resulting in captured images that are oscillating. When extrapolating the radius of the drop, this gives a large room for measurement error.

The data collected using the pendant drop method is consistent with the findings in [75]. In fact the data seems to overlap well showing that both the weight method and pendant drop method are comparable. This shows that evaporation can be considered negligible in this experiment since the pendant drop method involved exposing water to evaporation for relatively short periods of time (3 minutes) and the weighted method exposed water to evaporation for longer periods of up to 3.5 hours.

With the customised flow control system calibrated for flow speed, it is now easy to achieve the desired flow speed by adjusting the input gas pressure.

6.4 Hydrodynamic focusing

In this experiment, a double sheath flow that confines the main flow to the middle of the channel in one axis. Hydrodynamic focusing is used to reliability predict the position (across the width of a channel) of a flowing cell in the chip. It also moves

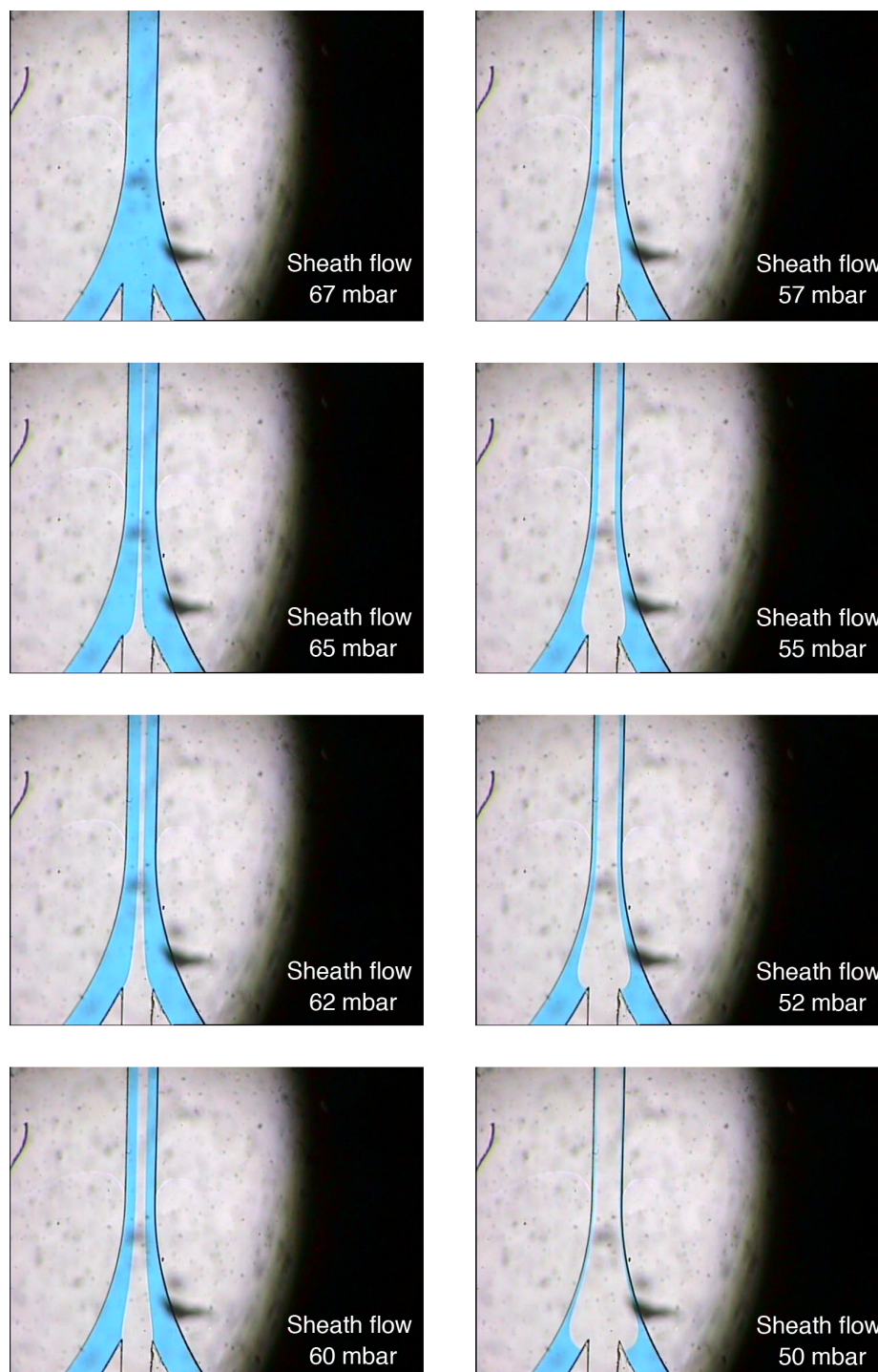


Figure 6.9: CCD images of double sheath hydrodynamic focusing in a 200 μm wide channel when main flow pressure is 44 mbar and sheath flow is varied.

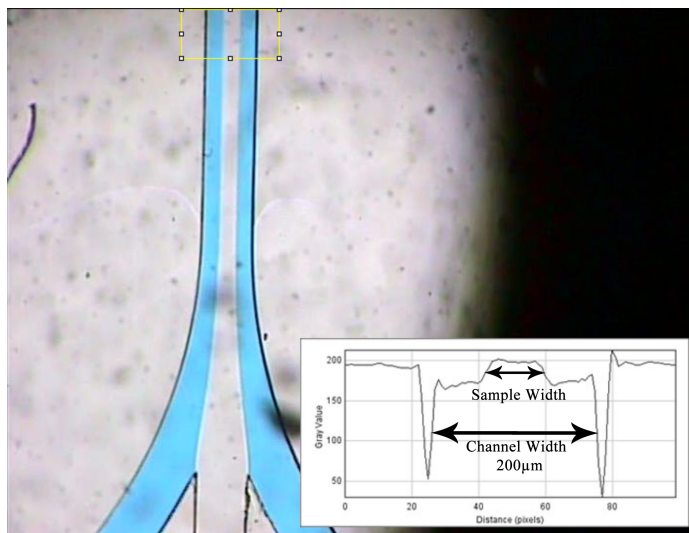


Figure 6.10: Hydrodynamic focusing in a 200 μm wide channel with line plot profile. Main sample flow had a pressure of 44 mbar and sheath flow was set to a pressure of 52 mbar.

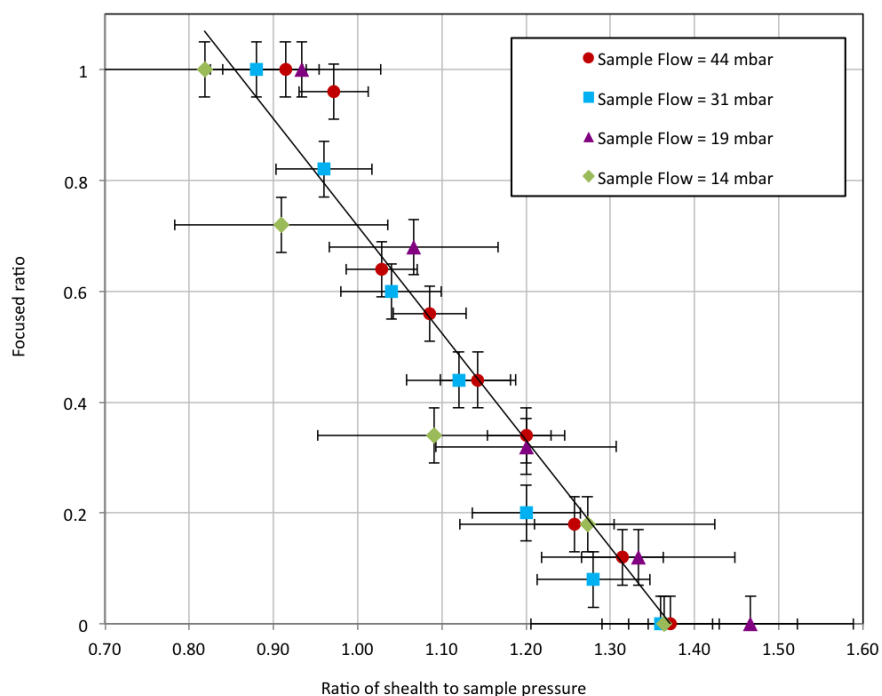


Figure 6.11: Hydrodynamic focused ratio of sheath to sample as a function of increasing flow ratios for different main flow pressures.

the cells away from the PDMS to liquid interface at the walls of the channel. This reduces the chance that scatter from the walls will interfere or overlap with that of the cell.

The aim of this section is to verify Equation 3.4 experimentally and determine the lowest pressure possible for hydrodynamic focusing to still work for the low cost pressure driven pump and the 200 μm wide PDMS chip. With the main flow kept at a constant flow rate, sheath flow pressure was adjusted and images were taken for each data point as shown in Figure 6.9. The main flow was then readjusted to a different pressure and the process was repeated. Images of the channel were attained from a colour CCD that generated separate channels for RGB (red green blue). For analysis, the R-channel proved to have the largest contrast between the blue sheath fluid and colourless main flow. The R-channel was converted to greyscale before being used to determine the line plot profile. The line plot profile was taken more than 200 μm from the junction as that was where the focusing stabilised [59]. The full width half maximum (FWHM) of the main flow was recorded and plot in Figure 6.11. Propagation of errors was calculated using standard deviations. Raw data can be found in the appendix.

The relationship between focusing width and flow ratio seems to be linear in this small range of pressure ratios. For a larger region such as the experiment conducted by Kunstmann-Olsen[59], it might not appear linear. The graph also seems relatively constant for different main sample flow pressures. The lowest attainable pressure settings for hydrodynamic focusing in this experiment is 13.7 mbarr in the main sample flow. I am limited by the ± 1.25 mbar (± 0.5 inH₂O) resolution on the gauge as the range of pressures that hydrodynamic focusing can be enabled reduces as the main sample flow pressure reduces. This can be improved with the purchase of a regulator and gauge with higher resolution.

Theoretical models are available for the hydrodynamic focusing in rectangular micro-channels comparing the focusing width to flow pressure and are used in [59] and [58] amongst other studies. However, the experiment performed in this section cannot be easily compared with the theoretical model as the model is not universal for all micro-channels. The theoretical model assumes a square channel cross section and sheath channels that are 90° to the main channel, whereas the experiment conducted in this thesis was performed with a rectangular channel of $200 \times 60 \mu\text{m}$ (width \times height) and sheath channels that are approximately 30° to the main channel. Furthermore, in this experiment when the pressure from the sheath channels were higher than the main channel, flow from the sheath channel would back flow into the main channel prematurely creating a focusing ratio of 0. This is probably due to the pump used, as the customised flow control system used in this experiment is more prone to backflow as compared to the syringe pump used to generate Figure 3.5 [59].

6.5 Integration of a solenoid valve for sorting

Solenoid valves are used in the generation of pulsed gas jets used as plasma targets for experiments on laser-plasma interactions, laser wakefield acceleration, and more. They are also used in the manufacturing industry where bursts of air are used in sorting. Here, solenoid valves are optimised for fast switching times as well as minimal impact velocities to reduce mechanical wear and extend the life of the valve; both characteristics that are desirable in the customised flow control system for the label-free cytometer.

A solenoid valve, with a fast rise time of approximately 25 ms [87, 75], was integrated into the customised flow control system to enable fast flow switching. When interfaced with the customised flow control system, I aim to find out the overall

response time of the system, and perform a simple proof-of-concept experiment to determine that the system works with fluorescence triggered sorting.

6.5.1 Experimental detection of cell sorting response time

To determine the response time of the customised flow control system, I used DI water with blue food dye for the solenoid activated side flow and colourless DI water for the main channel. Pressures for both main and side flow were set to 25 mbar. A digital colour CCD camera (WDAC-5700C, Micro Video Products, ON, Canada) was positioned over the sorting region to capture the activation of side flow. I also added an orange LED positioned in the sorting region and would light up when the solenoid valve is triggered.

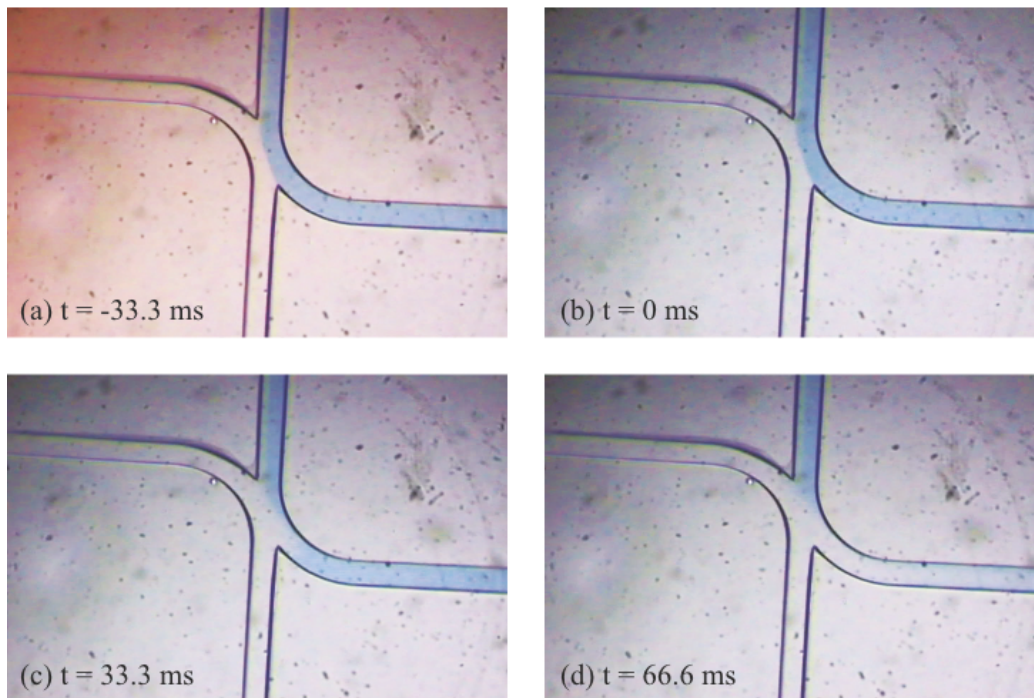


Figure 6.12: Frame by frame images of side flow switching 'off', extracted from a 30 fps video.

Figure 6.12 shows frame by frame images of the closing sequence of the side flow switch extracted from a 30 fps video. Figure 6.12 (a) shows the system when the solenoid and orange LED are still switched on, in (b) the DAQ has triggered the solenoid valve to close and the orange LED is no longer lit, in (c) we can see that there is no longer any pressure on the side flow channel, and (d) we can see the side flow fluid (blue) slowly being cleared from the sorting junction. Thus, it takes approximately 33.3 ms, or one frame, or less as I am limited by the frame rate of my video, for the DAQ to trigger the solenoid valve and for the pressure from the solenoid valve to the sorting junction to subside.

This experiment cannot be repeated for the systems rise time as it takes some time after the solenoid is triggered for the blue dye to reach the sorting junction. Thus we can assume that the system's rise time is similar to the fall time plus the difference between the rise and fall times of the solenoid valve. In his thesis, Islam determined this solenoid to have a rise time of 25 ms and a fall time of 10 ms [75], making the difference equal 15 ms. Thus, the customised flow control system with solenoid valve activated sorting has an opening response of less than 48.3 ms and a closing response of less than 33.3 ms.

The delay between the DAQ and the LED is typically on the order of nanoseconds and is assumed to be negligible in this experiment. There is however, considerable delay from the DAQ which has an analog output update rate of 150 Hz. This translates to a delay of 6.66 ms, not including the software delay within LabView itself. This can be corrected by using a digital output port or a different DAQ with a faster update rate. Or, a simple triggering circuit could be used instead of LabVIEW, further reducing the delay.

There are other solenoid valve options available on the market that give a comparable or faster response time, Table 6.4. A quick swap of the current solenoid

Table 6.4: Response Times of Various Solenoid Valves

Company	Model	Response Time	Price
Parker, OH, USA	Series 11/25/26	< 30 ms	\$40 to 69
Parker, OH, USA	001-0017-900	< 12 ms	\$125
Sizto Tech, CA, USA	2S025-050 series	< 20 ms	\$29 to 36
Cole-Parmer, QC, Canada	EW-01540-02	20 ms	\$126
ASCO, NJ, USA	188 Series 10mm	10 ms	\$65
Baccara Geva, Australia	GEVA 80 series	5 to 12 ms	-
Danfloss, Denmark	Type EV210A	7 to 10 ms	-

The information above was gathered from manufacturers website or from email quotations and are up-to-date as of Jan 1st, 2013.

valve with, for example, the GEVA 80 series solenoid valve (Baccara Geva, Australia), could potentially reduce the switching response of the system approximately 6.8 to 13.8 ms. There are other scientific systems that boasts lower response times reaching the sub-microns. For electro-pneumatic valves, Topcu et al. [88] presents a valve with theoretical and experimental opening times as fast as 3ms. Yang et al. [89] has developed a polymer micro-valve with a thermopneumatic actuator with a response time of 10 ms. Switching time is greater for valves activated by thermopneumatic actuators due to the time taken to heat the membrane, and is thus significantly influenced by the thickness of the heating membrane. Electrostatic micro-valves fare better than ones that rely on temperature gradients. Bae et al. [90] has developed an electrostatic silicon micro-valve with an opening and closing response time within 50 μ s.

However, there is a limit to the extent of which a faster valve response time will help the response time of the system since the gas is used to push the liquid into the chip. Therefore, the overall rise time of the system, ignoring effects of channel walls, is limited by the speed of pressure flow which assumed to equal the speed of sound—343 m/s in dry air and 1484 m/s in water. With the current setup, a 0.5 m air tube

and a 0.5 m liquid tube is used, plus a side flow channel length of approximately 2 cm. This contributes a time delay of 1.8 ms in the current setup. Thus, even with advances in valve response time, the switching response time is limited by the length of tubing and the speed of flow through it. This is one of the reasons why on chip micro-pumps and micro-valves have also become popular. Their reduced size and protability enables the valves and pumps to be placed close to the point of use, minimising the response delay due to tube and channel length.

6.5.2 Experimental fluorescence triggered sorting

To demonstrate the solenoid system can be used for cell sorting applications, I performed an experiment with fluorescent beads. As a bead flows past the detection area, laser light will cause the bead to fluoresce, sending a signal to the PMT located below the chip. A signal from a bead is shown in Figure 6.13. The bead signal shown is saturated but this is acceptable as it is only used for triggering purposes. This signal is then fed via the DAQ to LabVIEW that triggers the solenoid valve to open and sort the bead after a set delay depending on the flow speed of the bead. This delay gave the bead enough time to flow from the detection region to the sorting junction. The back panel of the LabVIEW program can be found in the appendix.

Figure 6.14 is comprised of superimposed frames and shows a fluorescent cell being sorted. This means that our in-house developed sorting system can indeed be used for sorting fluorescent beads. Provided that label-free cells can be effectively detected, the customised sorting system would also be able to sort label-free cells.

I did not perform an investigation on the sorting efficiency of this side flow sorter as this experiment was carried out on a similar system with results published by Islam [75]. At relatively high sheath and sample pressures ranging from 20 to 65 mbar,

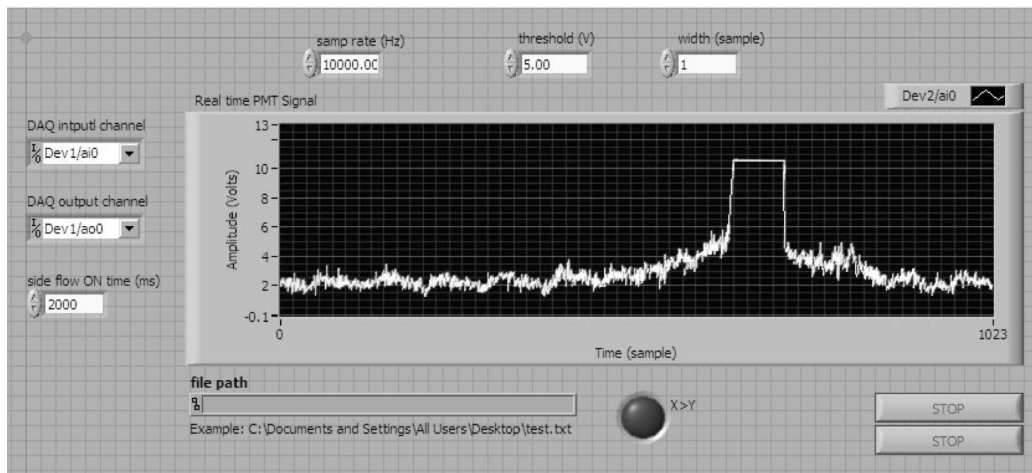


Figure 6.13: Front panel of LabVIEW showing the signal from a fluorescent bead flowing through the detection area.

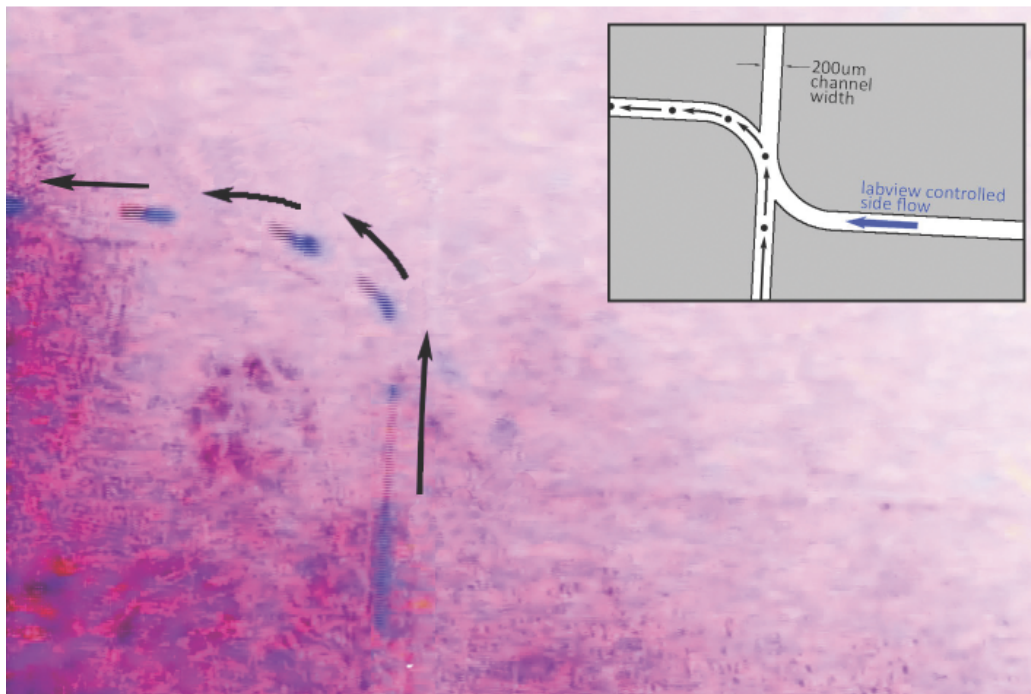


Figure 6.14: Superimposed image of a fluorescent bead being sorted. Colours have been inverted for easier viewing.

Islam [75] found a sorting efficiency of 87% to 97% sorting efficiency, with lower efficiencies at higher pressures. He predicts that for label-free cells, there would be an 11% decrease in the sorting efficiency due to false positives and missing positives. Further and more detailed work has to be done to determine the sorting efficiency for label-free cells.

Chapter 7

Conclusions

7.1 Summary

This thesis showcases an experimental approach to refine the design of the label-free cytometer, bringing it closer to a realisable device. The optimisations covered include microfluidic chip design and the development of a customised flow control and cell sorting mechanism.

Cytometry is a well established technique but conventionally uses fluorescence labelled-cells which are laborious and costly to prepare. Light scattering techniques can be used in cytometry without labels and can potentially provide much more information about the cell based on its Mie scattering pattern. Cells can be differentiated using this technique as different types of cells have different concentration, size, and shape of organelles, resulting in different scatter patterns. The scatter patterns are dominated by the mitochondria in the cell, due to its high index of refraction and many internal layers. Previous research has shown that mitochondria is the differentiating factor when distinguishing between prokaryotic and eukaryotic cells, Jurkat and CD34+ cells, and different cell maturities. Applications range from the sorting

of VSELs, to screening pathogens for early detection of bacteremia, as well as other instances where a small sample volume and specific detection is preferred over large commercial cytometers.

Microfluidics offers many advantages but also brings along unique considerations that have to be factored into the design. This includes highly laminar flow which coupled with a pressure-driven flow system, creates a velocity profile that is not uniform across the channel. Non-uniformity can be solved by hydrodynamically focusing cells into one particular laminar so the cells are always travelling along the same path and at the same speed (with a given pressure). Since surface area is much higher in microfluidics, the material chosen for the chip is of utmost importance. Many commercial flow control systems exist for microfluidic systems but many do not have the capability for pressure-driven cell sorting, while others that have this application are costly.

For microfluidic chip design, the chosen material is important. I discussed factors such as optical properties, background noise, hydrophilic or hydrophobic surface properties, bonding, and biological compatibility, with an emphasis on PMMA, PDMS, and glass. One must also consider how light will be guided into the channel as well as the size of the channel. I decided to use a PDMS chip, since: (1) previous PMMA-glass chips failed to bond well (2) an existing PDMS chip was being used in our group to successfully sort fluorescence labelled beads. Thus, the chip presented in this thesis is based on the chip in [75], but has been modified for laser light scattering and sorting of label-free cells. Fabrication involves the creation of a silicon master that can be used to create channels in PDMS by replica moulding. This negative PDMS imprint is then bonded to a featureless PDMS layer. Both Cryogenic ICP-RIE and Bosch ICP-RIE (STS) processes for etching the silicon master were tested. Despite the scalloped walls and lower selectivity, Bosh processing produced chips with visibly

lower noise.

PDMS chips with a $200\mu\text{m}$ wide channel, fabricated according to Chapter 4, were evaluated in the label free cytometer by flowing beads and cells through them and extracting their scatter patterns and intensities. Scatter patterns seem consistent with the structure of each cell. Unfortunately, high background noise interfered with many of the patterns, especially hard to image E Coil. In the future, steps have to be made to smoothen the channel and eliminate all features that cause unnecessary scatter.

Chapter 6, details the creation of a customised flow control system that can reliably control the pressure and speed of flow within a microfluidic channel. Average flow speed versus pressure applied by pump calibrations for the pressure driven pump system were performed to determine the average speed of flow within the microfluidic channel. With two different methods of calculation, spherical volume method and pendant drop method, calibrations were found to be linearly related as expected but with the spherical volume method giving much lower flow speeds due to errors with the model. Furthermore, the data presented from the pendant drop method overlaps with the data presented in [75], which used a more time consuming weighing method. Calibrations for hydrodynamic focusing for focused width versus pressure ratio, seem to follow a linear relationship over the small range of pressure ratios. The experimental data in this experiment does not provide an easy comparison to the hydrodynamic theoretical model as the theory is dependant among others on the geometry of the micro-channel. The solenoid valve that was introduced into the customised flow control system to enable fast flow switching was found to have a switching opening response of less than 48.3ms and a closing response of less than 33.3 ms. These measurements were limited by the 30fps speed of the CCD used. Other solenoid valve options available on the market give a comparable or faster response time and state of

the art scientific systems boasts responses in the sub-microseconds. Finally, I showed that our in-house developed sorting system can indeed be used for PMT triggered sorting of fluorescent beads.

In conclusion, a wide-angle label-free microfluidic flow cytometer has numerous advantages over conventional cytometry methods. But the optical technique used also imposes limitations on the device that are applicable only in certain niche markets. The current prototype has taken a step closer to a commercial product with a PDMS chip that is able to give us scatter patterns that is distinguishable between different cells, while being easy to fabricate and disposable. A prototype of the customised flow control system has proven to have a faster response time for cell sorting as compared to commercial systems. With more work, the label-free cytometer is expected to provide more information about internal structures of the biological cells without labelling, enabling us to distinguish between even more cells, especially hard to image cells such as E. Coli and VSELs. Implemented on a commercial scale, the proposed wide-angle microfluidic cytometer can prove beneficial in clinics and medical research institutions as a label-free way of characterising otherwise hard to differentiate cells.

7.2 Ongoing Work and Future Directions

This section discusses some research that is still in progress at the time of writing, and suggests ideas that could be developed the next generation of label-free cytometer.

7.2.1 Glass to PDMS chip

As suggested at the end of Section 4.4, the glass to PDMS chip with a 300 μm channel width was fabricated and is currently being tested. Initial scatter pattern data, collected by Zahurul Islam, show that the PDMS to glass chips do indeed reduce

the background noise quite significantly. Scatter patterns from CD34+ cells are shown in Figure 7.1.

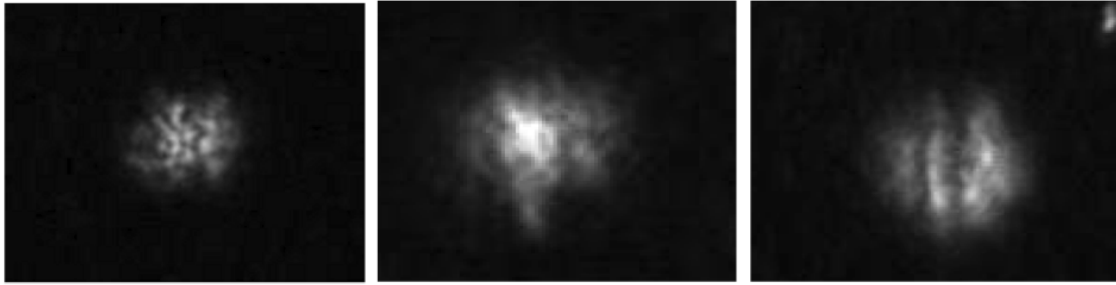


Figure 7.1: Scatter pattern of CD34+ cells with a glass to PDMS microfluidic chip with a $300\ \mu\text{m}$ channel width without background subtraction showing lower background noise.

Although background noise is predicted to be lowered drastically, it was predicted that the use of glass would reduce the efficiency of the waveguide on one wall as the index of refraction of glass is ($n=1.46$) is higher than the index of high index PDMS ($n = 1.41$). This is demonstrated in Figure 7.2.

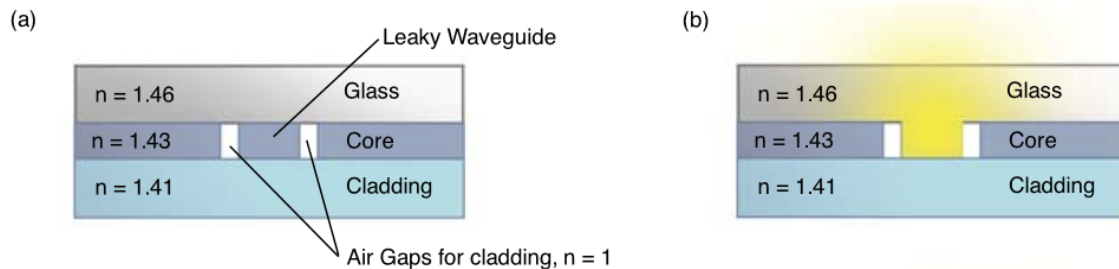


Figure 7.2: Cross-sectional view of (a) leaky waveguide in a PDMS to glass chip (b) light shining through the waveguide and leaking out through the glass.

However, this does not seem to be the case as light is still being guided into the channel. This can probably be attributed to a thin layer of air between the glass and PDMS layer that provided sufficient cladding for the waveguide core in the horizontal

direction. Experiments have to be done to determine the efficiency of this waveguide.

To further reduce background noise, it has been suggested that the chip should be flipped so that the glass layer is on top and the PDMS below. Since we are viewing from the top, light information entering the CCD will have gone through the glass instead of the PDMS. This is beneficial as glass has less internal non-uniformities as compared to PDMS, thus reducing the internal scattering that contributes to background noise.

7.2.2 Wide-angle Cytometer

One large improvement would be the integration of Sus wide angle cytometry work [28] into the current setup in attempt to collect more scatter light and information for cell identification. This involves positioning the CCD as close as possible to the fluid stream to increase angular range of collectable scatter from 11° to approximately 60° . We have suspicions that the concentric ring pattern seen in Figure 5.8 are aberrations caused by the microscope objective. Thus, implementing the wide-angle configuration would also eliminate this and increase the scatter signal.

Taking Sus wide-angle work one step further would be to increase the collection angle even more by pressing the CCD even closer to the chip. As seen in Figure 7.3(top), Sus setup has an air gap and a cover protecting the CCD. This is what limits the collection angle to 60° as the light scattered from a single scatterer has to propagate through a few different mediums before reaching the CCD detector. The interface between the different media reflects some of the larger angular scatter due to total internal reflection, thus diminishing the collection angle at each interface. As seen in Figure 7.3(bottom), Eliminating the glass cover and air gap will widen the collection angle, allowing forward and backward scatter at wider angles to propagate

to the CCD. Filling the gap with index matching fluid can further eliminate the minute air gap between the bare CCD array and the top plate of the microfluidics chip. Using this method, the collection angle will only be limited by the channel

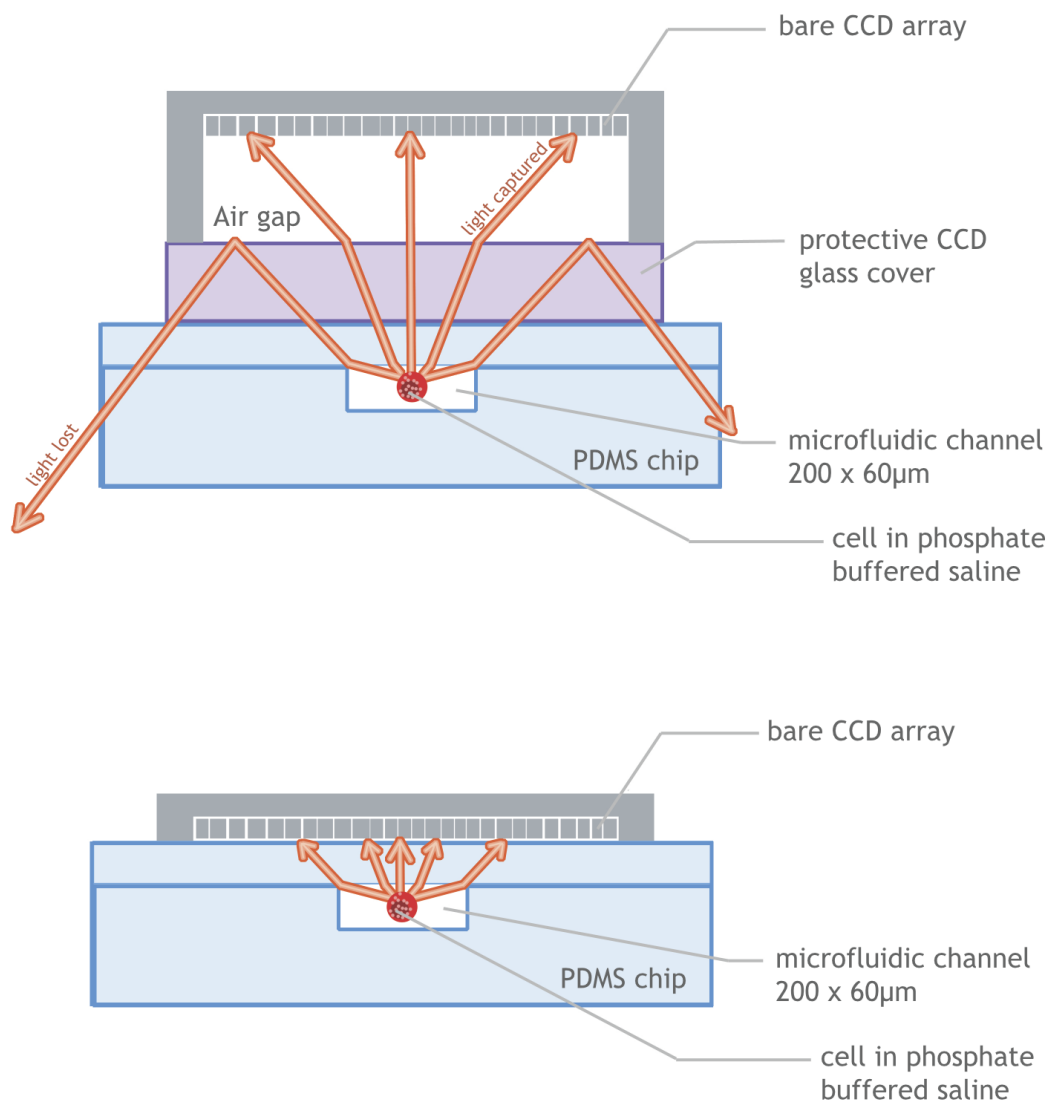


Figure 7.3: Top: Light scattered at 90° (side scatter) propagates to the CCD, while light close to 0° and 180° (forward and back scatter) light is reflected by total internal reflection at the glass-air interface. Bottom: The microfluidic chip is pressed against the CCD eliminating air gaps, creating a wider cone angle and allowing forward and back-scatter to propagate through to the CCD.

width and one might be able to attain a wide-angle collection of 160° . The scatter patterns collected with this improvement would contain much more information on not only the organelles within a cell and their distribution, but also information on the overall cell (size, shape, etc.)

7.2.3 Other suggestions

Besides implementing wide-angle viewing, one could improve the optical system with the following suggestions:

- Use a CCD camera that is faster and has a higher resolution to enable faster detection of flowing cells. Current camera speed is 30 fps and this only allows us to see cells travelling at relatively low speeds.
- The current platform is very shaky as it is located on a bench that is attached to a fume-hood with a fan that causes vibrations. This makes image subtraction unreliable in some cases and causes the image to occasionally go out of focus. This can be changed by moving the entire set up onto a solid optical table.
- Microscope objectives can be looked into to determine which types of objectives are less likely to cause interference with the scatter pattern.

The material, fabrication, and design of the microfluidic chip can be improved by:

- Glass chips could be looked into again if fabrication time and cost is not an issue. A liquid filled waveguide could replace the inserted optical fibre design.
- The chip could be made from a different polymer that does not "breathe" like PDMS does. This property allows the evaporation of sample from the channel and also means that the material is porous, affecting the optical clarity. A suggestion would be PS or PC.

- Characterisation of PDMS chips (not just the masters) made using the Cryogenic process and the Bosch process should be done to quantitatively determine which method is better.
- 3D hydrodynamic focusing at low speeds should be looked into. A single layer design that takes advantage of "microfluidic drifting" is easily implementable fabrication-wise and has been shown to work [91]. It will make the collection of scatter more reliable and comparable for multiple samples.
- Possibly integrating air-core (hollow) waveguides that can be used as optical waveguides or a microfluidic channel [92].
- The system can be miniaturised by integrating a light source (possibly LED), photodetector arrays, and other electronics onto the microfluidics chip. This would also eliminate the need for aligning.

Being only the first prototype, the pressure driven pump system with switching side flow can definitely be optimised for low cost, smaller sample size, and higher resolution, by:

- Purchasing a gauge with a higher resolution for the 0 to 2 psi gas regulator.
- Replacing current defunct solenoid valve with a newer model specially built for microfluidics with a faster rise and fall time.
- The sample reservoirs (filtering flask) should be replaced with ones that contain smaller sample volumes and vacuum seal screw-on caps (as currently the cork tends to pop off if too much pressure is applied). It would also be beneficial to make the parts of the pump that come into direct contact with the sample disposable to prevent cross-contamination.

- Integrating on chip micro-pumps and micro-valves.

One aspect of the label-free cytometer that has not been covered in this thesis is the computational image analysis of the scatter pattern. This has to be implemented real-time and has to interface with the CCD and the pump system for cell sorting. Overall, integrating all the various aspects on a fully integrated LOC can reduce the footprint of the entire device, enhancing portability.

Bibliography

- [1] Stem Cell Remedy Web Forums (n.d.). *Hierarchy of Stem Cells*. [Online] Accessed Dec 10, 2012, from <http://stemcellremedy.com/stem-cell-basics/stem-cell-and-cell-reprogramming-as-regenerative-medicine/>.
- [2] Ratajczak, M., Kucia, M., and Ratajczak, J. (2009). *Very Small Embryonic-Like (VSEL) Stem Cells & Methods of isolating and using the same*. U.S. Patent No. *US 2009/0220466A1*. US Patent and Trademark Office: Washington, DC. [Online] Retrieved April 16, 2012, from <http://www.uspto.gov>.
- [3] Zuba-Surma, E. K. and Ratajczak, M. Z. (2010). Overview of Very Small Embryonic-Like Stem Cells (VSEs) and Methodology of Their Identification and Isolation by Flow Cytometric Methods. In *Current Protocols in Cytometry*, John Wiley & Sons: Hoboken, NJ.
- [4] Ganong, W. F. (2005). *Review of Medical Physiology, 12th Ed.*, Lange Medical Publications: Los Altos, CA.
- [5] Danova-Alt, R., Heider, A., Egger, D., Cross, M., and Alt, R. (2012). Very small embryonic-like stem cells purified from umbilical cord blood lack stem cell characteristics. *PloS one*, 7(4), e34899.
- [6] Zuba-Surma, E., Klich, I., and Greco, N. (2009). Optimization of isolation and further characterization of umbilical cord blood-derived very small embryonic/epiblast-like stem cells (VSEs). *European Journal of Haematology*, 84, 34-46.
- [7] Ratajczak, M. Z., Kucia, M., Ratajczak, J., and Zuba-Surma, E. K. (2009). A multi-instrumental approach to identify and purify very small embryonic like stem cells (VSEs) from adult tissues. *Micron*, 40(3), 386393.
- [8] Ratajczak, M. Z., Liu, R., Marlicz, W., Blogowski, W., Starzynska, T., Wojakowski, W., and Zuba-Surma, E. (2011). Identification of Very Small Embryonic/Epiblast-Like Stem Cells (VSEs) Circulating in Peripheral Blood During Organ/Tissue Injuries. In *Recent advances in cytometry B, Advances in applications, 5th Ed.*, (Vol. 103, pp. 3154) Elsevier Academic Press: Oxford, UK.

- [9] Abdel-Latif, A., Zuba-Surma, E. K., Ziada, K. M., Kucia, M., Cohen, D. A., Kaplan, A. M., Van Zant, G., Selim, S., Smyth, S. S., and Ratajczak, M. Z. (2010). Evidence of mobilization of pluripotent stem cells into peripheral blood of patients with myocardial ischemia. *Experimental hematology*, 38(12), 1131-1142.
- [10] Kucia, M., Zhang, Y. P., Reza, R., Wysoczynski, M., Machalinski, B., Majka, M., Ildstad, S. T., Ratajczak, J., Shields, C. B., and Ratajczak, M. Z. (2006). Cells enriched in markers of neural tissue-committed stem cells reside in the bone marrow and are mobilized into the peripheral blood following stroke. *Leukemia*, 20(1), 18-28.
- [11] Paczkowska, E., et al. (2009). Clinical Evidence That Very Small Embryonic-Like Stem Cells Are Mobilized Into Peripheral Blood in Patients After Stroke. *Stroke*, 40(4), 1237-1244.
- [12] Wojakowski, W. (2005). Mobilization of CD34+, CD117+, CXCR4+, c-met+ stem cells is correlated with left ventricular ejection fraction and plasma NT-proBNP levels in patients with acute myocardial infarction. *European Heart Journal*, 27(3), 283289.
- [13] Wojakowski, W., et al. (2009). Mobilization of bone marrow-derived Oct-4+ SSEA-4+ very small embryonic-like stem cells in patients with acute myocardial infarction. *Journal of the American College of Cardiology*, 53(1), 1-9.
- [14] Zuba-Surma, E. K., Kucia, M., Dawn, B., Guo, Y., Ratajczak, M. Z., and Bolli, R. (2008). Bone marrow-derived pluripotent very small embryonic-like stem cells (VSELs) are mobilized after acute myocardial infarction. *Journal of molecular and cellular cardiology*, 44(5), 865-873.
- [15] Soleymani, L. (2010). Ultra sensitive Detection of Nucleic Acids using an Electronic Chip. *PhD. thesis*, University of Toronto: Toronto, ON.
- [16] Gao, B. and Gupta, R. S. (2012). Phylogenetic Framework and Molecular Signatures for the Main Clades of the Phylum Actinobacteria. *Microbiology and Molecular Biology Reviews*, 76(1), 66-112.
- [17] University of Munster, Medical Faculty. (2011). Impact of New Innovative POC diagnosis for HIV/AIDs, malaria, & tuberculosis. Presented at *XXVI Congress of the International Society for Advancement of Cytometry, Baltimore, MD, May 2011*.
- [18] Marinucci, F., University of Maryland. (2011). Low cost cytometry for infectious diseases CD4+ testing in Africa for HIV AIDs detection. Presented at *XXVI Congress of the International Society for Advancement of Cytometry, Baltimore, MD, May 2011*.

- [19] Fang, H., Qiu, L., Vitkin, E., and Zaman, M. (2007). Confocal light absorption and scattering spectroscopic microscopy. *Applied optics*, 46(10), 1760-1769.
- [20] Shapiro, H. M. (2003). *Practical Flow Cytometry, 4th Ed.* John Wiley & Sons: Hoboken, NJ.
- [21] Su, X., Capjack, C., Rozmus, W., and Backhouse, C. (2007). 2D light scattering patterns of mitochondria in single cells. *Optics Express*, 15(17), 1056210575.
- [22] Su, X., Rozmusa, W., and Capjack, C. (2007). Side scatter light for micro-size differentiation and cellular analysis. In *Proceedings of SPIE, Aug 2007*, (Vol. 6446, pp. 1-9).
- [23] Su, X., Singh, K., Capjack, C., and Petracek, J. (2008). Measurements of light scattering in an integrated microfluidic waveguide cytometer. *Journal of Biomedical Optics*, 13(2), 024024/1-024024/10.
- [24] Su, X., Singh, K., Rozmus, W., Backhouse, C., and Capjack, C. (2009). Light scattering characterization of mitochondrial aggregation in single cells. *Optics Express*, 17(16), 13381-13388.
- [25] Su, X. and Rozmus, W. (2010). A fiber-coupled microfluidic cytometer for the obtaining of nanostructural mitochondria information in single cells. In *Proceedings of SPIE, Aug 2010* (Vol. 7573, pp. K1-K8).
- [26] Su, X. T., Qiu, Y., Marquez-Curtis, L., Gupta, M., Capjack, C. E., Rozmus, W., Janowska-Wieczorek, A., and Tsui, Y. Y. (2011). Label-free and noninvasive optical detection of the distribution of nanometer-size mitochondria in single cells. *Journal of Biomedical Optics*, 16(6), 067003.
- [27] Su, X., Kirkwood, S. E., Gupta, M., Marquez-Curtis, L., Qiu, Y., Janowska-Wieczorek, A., Rozmus, W., and Tsui, Y. Y. (2011). Microscope-based label-free microfluidic cytometry. *Optics Express*, 19(1), 387-398.
- [28] Su, X., Rozmus, W., and Tsui, Y. Y. (2010). Wide-angle light-scattering differentiation of organelle-size particle distributions in whole cells. *Cytometry Part A*, 77A, 580-584.
- [29] Huang, P., Feng, L., Oldham, E. A., Keating, M. J., and Plunkett, W. (2000). Superoxide dismutase as a target for the selective killing of cancer cells. *Nature*, 407(6802), 390-395.
- [30] Yu, C.-C., Lau, C., Tunnell, J. W., Hunter, M., Kalashnikov, M., Fang-Yen, C., Fulghum, S. F., Badizadegan, K., Dasari, R. R., and Feld, M. S. (2006). Assessing epithelial cell nuclear morphology by using azimuthal light scattering spectroscopy. *Optics letters*, 31(21), 31193121.

- [31] Michikawa, Y., Mazzucchelli, F., Bresolin, N., Scarlato, G., and Attardi, G. (1999). Aging-dependent large accumulation of point mutations in the human mtDNA control region for replication. *Science*, 286(5440), 774779.
- [32] Trimmer, P. A., Swerdlow, R. H., Parks, J. K., Keeney, P., Bennett, J. P., Miller, S. W., Davis, R. E., and Parker, W. D. (2000). Abnormal mitochondrial morphology in sporadic Parkinsons and Alzheimers disease cybrid cell lines. *Experimental neurology*, 162(1), 3750.
- [33] Watson, D., Hagen, N., Diver, J., Marchand, P., and Chachisvilis, M. (2004). Elastic light scattering from single cells: orientational dynamics in optical trap. *Biophysical journal*, 87(2), 1298-1306.
- [34] Asbury, C. L., Jeanne L. Uy, and Ger van den Engh. (2000). Polarization of scatter and fluorescence signals in flow cytometry. *Cytometry*, 40(2), 88-101.
- [35] Weissmann, D., University of Medicine and Dentistry of New Jersey. (2006). *Hematopathology: Immunophenotyping Lymphomas*. [Online] Accessed Dec 05, 2011. (<http://pleiad.umdnj.edu/~dweiss/immuno/immuno.html>).
- [36] Cheung, K., Gawad, S., and Renaud, P. (2005). Impedance spectroscopy flow cytometry: On-chip label-free cell differentiation. *Cytometry Part A*, 65A, 124-132.
- [37] Itzkan, I., Qiu, L., Fang, H., and Zaman, M. (2007). Confocal light absorption and scattering spectroscopic microscopy monitors organelles in live cells with no exogenous labels. In *Proceedings of the National Academy of Sciences, October 2007* (Vol. 104(44), pp. 17255-17260).
- [38] Hsiao, A., Hunter, M., Greiner, C., Gupta, S., and Georgakoudi, I. (2011). Non-invasive identification of subcellular organization and nuclear morphology features associated with leukemic cells using light-scattering spectroscopy. *Journal of Biomedical Optics*, 16(3), 037007.
- [39] Su, X. T. (2008). Light Scattering in an Integrated Microfluidic Waveguide Cytometer. *PhD. thesis*, University of Alberta: Edmonton, AB.
- [40]] Bohren, C. F. and Huffman, D. R. (1983). *Absorption and Scattering of Light by Small Particles*. John Wiley & Sons: Hoboken, NJ.
- [41] Walter T Grandy, J. (2000). *Scattering of Waves from Large Spheres*. Cambridge University Press: Cambridge, UK.
- [42] van de Hulst, H. C. (1981). *Light scattering: by small particles*. Dover Publications, Inc: New York, NY.

- [43] Mourant, J. R., Freyer, J. P., Hielscher, A. H., Eick, A. A., Shen, D., and Johnson, T. M. (1998). Mechanisms of light scattering from biological cells relevant to noninvasive optical-tissue diagnostics. *Applied optics*, 37(16), 35863593.
- [44] Neukammer, J., Gohlke, C., Höpe, A., Wessel, T., and Rinneberg, H. (2003). Angular distribution of light scattered by single biological cells and oriented particle agglomerates. *Applied optics*, 42(31), 63886397.
- [45] (n.d.). *Illustration of an animal cell*. [Online] Accessed Dec 12, 2012, from (<http://www.rojo5th.net/2010/08/14/cells-2/>).
- [46] Cooper, G. M., and Hausman, R. (2007). *The cell: a molecular approach, 4th Ed.* ASM Press: Washington, DC.
- [47] Albertas, B., Bray, D., Lewis, J., Raff, K., Roberts, K., and Watson, J. (1994). *Molecular biology of the cell.*, Garland: New York, NY.
- [48] Dunn, A. K. (1997). Light scattering properties of cells. *PhD. thesis*, University of Texas: Austin, TX.
- [49] Lehninger, A. L. (1970). *Biochemistry:the molecular basis of cell structure and function, 1st Ed.* Worth Publishers: New York, NY.
- [50] Gourley, P. L., Hendricks, J. K., McDonald, A. E., Copeland, R. G., Barrett, K. E., Gourley, C. R., and Naviaux, R. K. (2005). Ultrafast nanolaser flow device for detecting cancer in single cells. *Biomedical microdevices*, 7(4), 331339.
- [51] Herold, K. E. and Rasooly, A. (2009). *Lab on a Chip Technologies. Volume 1: Fabrication and Microfluidics.* Caister Academic Press: Norfolk, UK.
- [52] Kirby, B. J. and Hasselbrink, E. F. (2004). Zeta potential of microfluidic substrates: 1. Theory, experimental techniques, and effects on separations. Review from *Electrophoresis*, 25(2), 187-202.
- [53] Herr, A. E., Molho, J. I., Santiago, J. G., Mungal, M. G., Kenny, T. W., and Garguilo, M. G. (2000). Electroosmotic Capillary Flow with Nonuniform Zeta Potential. *Analytical Chemistry*, 72(5), 10531057.
- [54] Dutta, D., Ramachandran, A., and Leighton, D. T., Jr (2006). Effect of channel geometry on solute dispersion in pressure-driven microfluidic systems. *Microfluidics and Nanofluidics*, 2(4), 275290.
- [55] McClain, M. A., Culbertson, C. T., Jacobson, S. C., Allbritton, N. L., Sims, C. E., and Ramsey, J. M. (2003). Microfluidic Devices for the High-Throughput Chemical Analysis of Cells. *Analytical Chemistry*, 75(21), 56465655.

- [56] Chang, D. C., Chassy, B. M., Saunders, J. A., and Sowers, A. E. (eds.) (1992). *Guide to Electroporation and Electrofusion*, Academic Press: San Diego, CA.
- [57] Pappas, D. (2010). *Practical Cell Analysis*, John Wiley & Sons: Hoboken, NJ.
- [58] Wu, Z. and Nguyen, N.T. (2005). Hydrodynamic focusing in microchannels under consideration of diffusive dispersion: theories and experiments. *Sensors and Actuators B: Chemical*, 107(2), 965-974.
- [59] Kunstmann-Olsen, C., Hoyland, J. D., and Rubahn, H.G. (2011). Influence of geometry on hydrodynamic focusing and long-range fluid behaviour in PDMS microfluidic chips. *Microfluidics and Nanofluidics*, 12(5), 795-803.
- [60] Blonski, S., Domagalski, P., and Kowalewski, T. A. (n.d.). Flow Focusing in Microfluidic Devices. [Preprint] Accessed Dec 05, 2012, from http://ippt.pan.pl/~sblonski/docs/sblonski_kkmp2010.pdf.
- [61] Born, C., Zhang, Z., Al-Rubeai, M., and Thomas, C. R. (1992). Estimation of disruption of animal cells by laminar shear stress. *Biotechnology and bioengineering*, 40(9), 10041010.
- [62] Chisti, Y. (2001). Hydrodynamic damage to animal cells. *Critical reviews in biotechnology*, 21(2), 67110.
- [63] Stolberg, S. and McCloskey, K. E. (2009). Can shear stress direct stem cell fate? *Biotechnology Progress*, 25(1), 1019.
- [64] McHale, G., Shirtcliffe, N. J., and Newton, M. I. (2004). Contact-angle hysteresis on super-hydrophobic surfaces. *Langmuir* 20(23), 1014610149.
- [65] McDonald, J. C., Duffy, D. C., Anderson, J. R., Chiu, D. T., Wu, H., Schueller, O. J., and Whitesides, G. M. (2000). Fabrication of microfluidic systems in poly(dimethylsiloxane). *Electrophoresis*, 21(1), 2740
- [66] Morra, M., Occhiello, E., and Garbassi, F. (1989). Contact angle hysteresis in oxygen plasma treated poly(tetrafluoroethylene) *Langmuir (ACS Publications)*, 5(3), 872876.
- [67] van Midwoud, P. M., Janse, A., Merema, M. T., Groothuis, G. M. M., and Verpoorte, E. (2012). Comparison of Biocompatibility and Adsorption Properties of Different Plastics for Advanced Microfluidic Cell and Tissue Culture Models. *Analytical Chemistry*, 84(9), 39383944.
- [68] Nguyen, N.T., Huang, X., and Chuan, T. K. (2002). MEMS-Micropumps: A Review. *Journal of Fluids Engineering*, 124(2), 384-392.

- [69] Augustin, W., Bohnet, M. (1999). Influence of pulsating flow on fouling behaviour. In: Proceedings of the Engineering Foundation Conference on Mitigation of Heat Exchanger Fouling and Environmental Implications, 161-168.
- [70] Gillham, C.R., Fryer, P.J., Hasting, A.P.M., Wilson, D.I. (2000). Enhanced cleaning of whey protein fouling deposits using pulsed flows. *Journal of Food Engineering* 46, 199209.
- [71] Bode, K., Hooper, R.J., Paterson, W.R., Wilson, D.I., Augustin, W., Scholl, S., 2007. Pulsed flow cleaning of whey protein fouling layers. *Heat Transfer Engineering* 28, 202209.
- [72] Qi, X. G., Scott, D. M., & Wilson, D. I. (2008). Modelling laminar pulsed flow in rectangular microchannels. *Chemical Engineering Science*, 63(10), 2682-2689.
- [73] Celnik, M. S., Patel, M. J., Pore, M., Scott, D. M., & Wilson, D. I. (2006). Modelling laminar pulsed flow for the enhancement of cleaning. *Chemical engineering science*, 61(6), 2079-2084.
- [74] Fluigent. (May 10, 2012). MFCS-FLEX Technology Presentation. [Online] Accessed Dec 5, 2012, from (<http://www.fluigent.com/>).
- [75] Islam, M. Z. (2012). Development of an Efficient Quasi-3D Microfluidic Flow Model and Fabrication and Characterization of an All-PDMS Opto-Microfluidic Flow Cytometer. *PhD. thesis*, University of Alberta: Edmonton, AB.
- [76] Piruska, A., Nikcevic, I., Lee, S. H., Ahn, C., Heineman, W. R., Limbach, P. A., and Seliskar, C. J. (2005). The autofluorescence of plastic materials and chips measured under laser irradiation. *Lab on a Chip*, 5(12), 1348-1354.
- [77] Haynes, W.M., and Lide, D. R. (1981). *CRC Handbook of Chemistry and Physics*, 62nd Ed. [Online] Accessed on August 7, 2012.
- [78] Zhernovaya, O., Sydoruk, O., Tuchin, V., and Douplik, A. (2011). The refractive index of human hemoglobin in the visible range. *Physics in Medicine and Biology*, 56(13), 4013-4021.
- [79] Naito, T., Arayanarakool, R., LeGac, S., Yasui, T., Kaji, N., Tokeshi, M., van den Berg, A., and Baba, Y. (2013). Temperature-driven self-actuated microchamber sealing system for highly integrated microfluidic devices. *Lab on a Chip*, 13(3), 452-458.
- [80] Santiago-Alvarado, A., Montiel, S. V., Munoz-Lopez, J., Castro-Ramos, J., and Atencio, J. D. (2009). Parametric and scattering characterization of PDMS membranes for optical applications. *SPIE Optical Engineering & Applications*, 742615-742615.

- [81] Rozenberg, G. (2011). *Microscope Haematology: A practical guide for the laboratory, 3rd Ed.* Elsevier: Australia.
- [82] Valkenburg, J. A. and Woldringh, C. L. (1984). Phase separation between nucleoid and cytoplasm in *Escherichia coli* as defined by immersive refractometry. *Journal of bacteriology*, 160(3), 1151-1157.
- [83] Marcatili, E. A. J. (1969). "Dielectric rectangular waveguide and directional coupler for integrated optics", *Bell System Technical Journal*, 48, 2071-2102.
- [84] Renner, Hagen. (1998). Polarization characteristics of optical waveguides with separable symmetric refractive-index profiles. *Journal of Optical Society of American A*, 15, 1401-1410.
- [85] Garandet, J.P. and Vinet, B. and Gros, P. (1994). Considerations on the pendant drop method: a new look at Tate's law and Harkins' correction factor. *Journal of colloid and interface science*, 165(2), 351-354.
- [86] Villermaux, E. and Bossa, B. (2009). Single-drop fragmentation determines size distribution of raindrops. *Nature Physics*, 5(9), 697702.
- [87] Wolterink, T. A. W. (2011). High-gradient gas-jet targets for laser wakefield acceleration. *PhD. thesis*, University of Twente: Enschede, Netherlands.
- [88] Topçu, E. E., Yüksel, İ, and Kamiş, Z. (2006). Development of electro-pneumatic fast switching valve and investigation of its characteristics. *Mechatronics*, 16(6), 365-378.
- [89] Yang, B., Wang, B., and Schomburg, W. K. (2010). A thermopneumatically actuated bistable microvalve. *Journal of Micromechanics and Microengineering*, 20(9), 095024.
- [90] Bae, B., Han, J., Masel, R. I., and Shannon, M. A. (2007). A bidirectional electrostatic microvalve with microsecond switching performance. *Microelectromechanical Systems, Journal of*, 16(6), 1461-1471.
- [91] Mao, X., Nawaz, A. A., Lin, S.-C. S., Lapsley, M. I., Zhao, Y., McCoy, J. P., El-Deiry, W. S., and Huang, T. J. (2012). An integrated, multiparametric flow cytometry chip using microfluidic drifting based three-dimensional hydrodynamic focusing. *Biomicrofluidics*, 6(2), 24113241139.
- [92] Epp, E., Ponnampalam, N., Newman, W., and Drobot, B. (2010). Hollow Bragg waveguides fabricated by controlled buckling of Si/SiO₂ multilayers. *Optics Express*, 18(24), 24917-24925.
- [93] Nanofabrication Facility. (2010). *Alcatel deep etches*. [Internal Report] University of Alberta: Edmonton, AB.

- [94] Jia, Z.-J., Fang, Q., and Fang, Z.-L. (2004). Bonding of Glass Microfluidic Chips at Room Temperatures. *Analytical Chemistry*, 76(18), 55975602.
- [95] Dang, F., Shinohara, S., Tabata, O., Yamaoka, Y., Kurokawa, M., Shinohara, Y., Ishikawa, M., and Baba, Y. (2005). Replica multichannel polymer chips with a network of sacrificial channels sealed by adhesive printing method. *Lab on a Chip*, 5(4), 472478.
- [96] Tsao, C.-W. and DeVoe, D. L. (2008). Bonding of thermoplastic polymer microfluidics. *Microfluidics and Nanofluidics*, 6(1), 116.
- [97] Baeurle, S. and Hotta, A. (2006). On the glassy state of multiphase and pure polymer materials. *Polymer*, 47, 62436253.
- [98] Zhu, X., Liu, G., and Guo, Y. (2006). Study of PMMA thermal bonding. *Microsystem Technologies*, 13, 403407.
- [99] Chow, W., Lei, K., Shi, G., and Li, W. (2006). Microfluidic channel fabrication by PDMS-interface bonding. *Smart Materials and Structures*, 15, S112S116.
- [100] Mo, M. (2011). *Summary of Calibration of Luca and Chameleon*. [Internal Report] University of Alberta: Edmonton, AB.
- [101] Prahl, S., Oregon Medical Laser Centre. (2012). *Mie Scattering Calculator*. [Online] Accessed Dec 14, 2012, from http://omlc.ogi.edu/calc/mie_calc.html.

Appendices

A.1 Failed Chip Designs

This section discusses in detail the fabrication of other chip designs that were attempted but failed to yield usable chips.

A.1.1 Previous Label-free Glass Chip Design

The previous microfluidic chip design is described in [22, 23, 27]. A microfluidic structure was first printed onto a $120\mu\text{m}$ thick polymer sheet (Cannon transparency type E, Canon USA, Inc., NY, USA) using a laser printer. The microfluidic channel was then cut out using a surgical blade as well as channels on either side of the microfluidic channel for the placement of optical fibres ($105/125\ \mu\text{m}$ multimode fibre, Thorlabs, NJ, USA). These fibres are used to guide the laser into and out of the channel. This gasket was then sandwiched between two standard microscope slides (12-544-1, 25mm by 75mm, Fisher Scientific Company, ON, Canada), of which one had pump-in and pump out holes pre-drilled into it. Lastly, the optical fibres were laid in place and UV epoxy (Optical adhesive 81, Norland Products Inc., NJ, USA) was applied to the edges and cured with UV light for approximately 2 minutes to form a strong bond. The resulting microfluidic channel has a width of $600\mu\text{m}$, height of $120\mu\text{m}$, and length of 46mm.

A.1.2 Full glass chip

We briefly explored the possibility of creating full glass chips using the equipment in the University of Albertas nano-fabrication facility. Glass chips are a good choice for microfluidic chips as both fabrication and bonding techniques are well known. It is also a stable, hydrophilic, inert material that will not interfere with biological cells. Glass microfluidic chips are fabricated by performing a wet RIE etch on glass. This can be done using a nickel (Ni) plating mask to create microfluidic channels with depths greater than a few tens of microns.

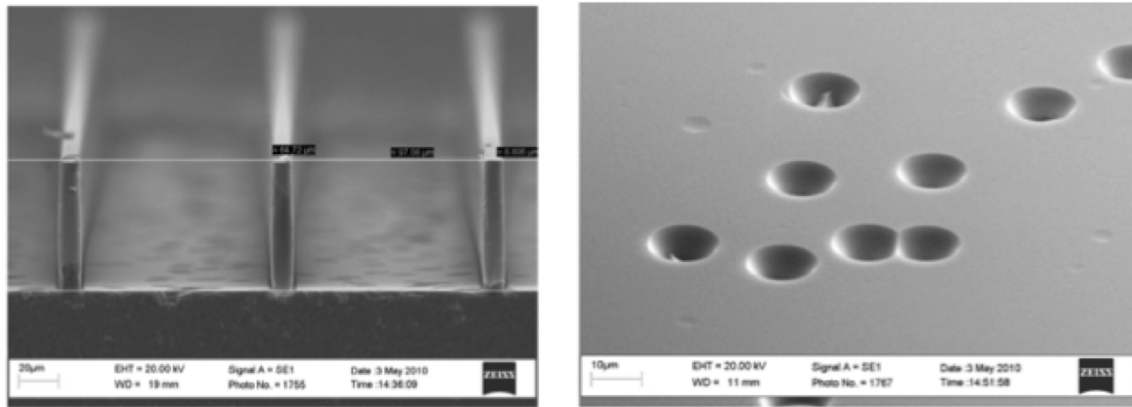


Figure 7.4: Deep etched quartz using the Alcatel Deep Etch system (a) $10\mu\text{m}$ lines, $65\mu\text{m}$ depth (b) Pitting on the etched surface [93]

Quartz was shown to give smooth anisotropic vertical walls of but displayed pitting on the bottom surface, which would interfere with scatter [93] as shown in the Figure 7.4. Pyrex, on the other hand, Figure 7.5, was shown to give smooth but slightly sloped walls (100°) with no pitting, making it the material of choice for the fabrication of a glass chip [93]. For the cover slide, I plan to use 0211 glass, with a thickness of $500\mu\text{m}$. To reduce or eliminate the ambient light entering the chip and interfering with the scatter, the 0211 glass can be coated with chrome and a small window etched

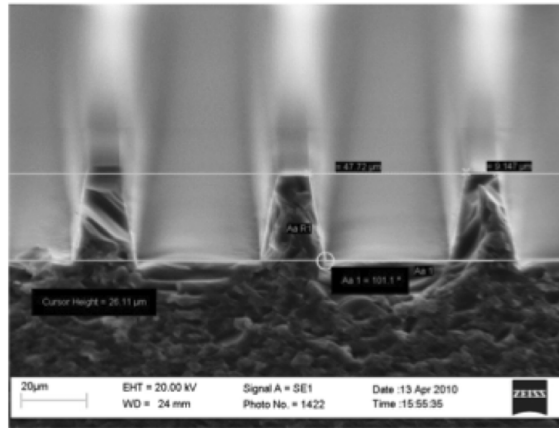


Figure 7.5: Deep etched Pyrex, $10\mu\text{m}$ lines, $26\mu\text{m}$ depth, [93]

out just at the illuminated spot so the CCD can access the scatter.

Thus, these chips have the disadvantage of a long fabrication time (wet etch and thermal bonding are time consuming processes), low yield, and expensive material cost [95]. More work has to be done to streamline the fabrication process and increase the production yield.

A.1.3 PMMA chip

Advances in creating micro-components from thermoplastic polymers have made it a viable replacement for glass-to-glass or glass-to-silicon microfluidic chips. Thermoplastic polymers, also called thermosoftening plastics, turns into a malleable solid or liquid when heated and hardens to a smooth glassy state when cooled [96, 97]. Examples include PMMA, PET, and COP. Unlike thermoset polymers (e.g. PDMS), thermoplastic polymers can also be resoftened and reshaped upon heating, remaining chemically and dimensionally stable over a wide range of operational temperatures and pressures [96]. Therefore, thermoset polymers are more likely to be used in situations where thermal stability is required, whereas thermoplastic polymers are

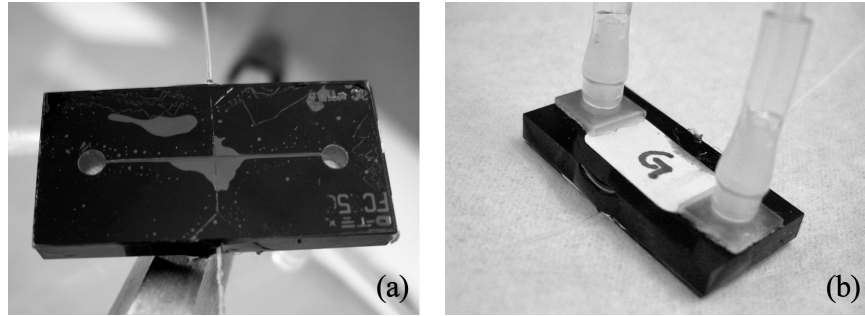


Figure 7.6: PMMA base bonded with UV epoxy to 500 μ m thick 0211 glass cover (a) bottom view showing channel (b) top view showing input and output connectors.

used when the chip will be subject to high mechanical stress and tensile strength is required. Since temperature is usually kept constant in microfluidic applications while the channel is subject to high-pressure stress, we initially chose thermoplastic polymers as our polymer of choice for moulding micro-channels.

I have started fabricating and testing a PMMA chip that was partially made for us courtesy of Kirat Singh. It consists of a black opaque PMMA base that has been bonded to a thin glass cover and is pictured in Figure 7.6. Black PMMA was used due to its availability and the fact that it is opaque, reducing scatter from room light and from stray laser light.

To make the silicon moulds for hot embossing, first, photomasks of the chip designs were submitted to and made at the Nanofabrication facility at ACAMP (ACAMP, Edmonton, AB, Canada). Photolithography was also done in the Nano-fabrication facility on silicon wafers but deep RIE etched (DRIE) at Micralyne Inc. (Edmonton, AB, Canada). The polymer used for the chips is optically opaque PMMA (ACRYLITE FF (extruded) Black 9M001 GT, Evonik Cyro LLC, ME, USA) with a thickness of 3mm. Using the silicon mold, the chips were embossed at ACAMP using a Jenoptik HEX04 Hot Embosser. The polymer sheets were heated up to 130°C and the mold was pressed into them at 14 kN for 5 min. Demolding was then done at 105°C. Holes

were then drilled (using a manual drill-press) to make the ports on the chips. The plastic sheets were then diced into individual chips using a Disco dicing saw. From here, cleaved optical fibres (105/125 μm multimode fibre, Thorlabs, NJ, USA) were laid in place and was bonded to a thin 500 μm 0211 glass surface by applying UV epoxy (Optical adhesive 68, Norland Products Inc., NJ, USA) around the channels. It was then cured under UV light for approximately 10 minutes. The last step was to attach the tube fittings to the ports on the chips. Double-sided tube fittings were purchased from McMaster-Carr (5116K16, GA, USA), cut in half and glued onto the chip (KG484 GEL, KRAZY glue, OH, USA). Tygon tubing (C-Flex RK-06422-02, Cole-Parmer Instrument Company, QC, Canada) was attached to the tube fittings to lead fluid from the syringe into the chip and from the chip to a waste receptacle. Note that no surface treatment was applied to reduce the hydrophobicity of the material. If desired, a 30 min UV ozone treatment could be implemented before bonding.

Unfortunately, the bonding of the PMMA chip posed many challenges. I found difficulties forming a permanent chemical bond between the glass and the PMMA. I tried thermocompression bonding of PMMA to glass as outlined in [98] but the bond did not hold, instead the high temperature caused deformations in the channel walls. I also tried bonding PMMA to glass via PDMS as outlined in [99]. First a thin layer of PDMS is spun on the glass and partially cured to improve viscosity. Next, the PMMA is placed on to the PDMS coated glass and the chip is placed under a weight and left to fully cure overnight. But again, the bond did not hold. Adherent bonding with UV epoxy has since proven to be the only method of effective bonding, but it too has its problems as described in Section 4.1.4. A solution would be to try to bond using a laser to melt the PMMA onto the glass. With a precision XYZ translation stage, bonding can be done very accurately without the risk of foreign particles falling into the channel and clogging it or creating speckles seen in Figure 4.3.

A.2 Mie Code Modifications

Originally published in the Appendix of [40], the Mie scattering codes used in this thesis are popularly called the 'Bohren-Huffman codes'. The original code was written in Fortran and has since been translated into C, IDL, Matlab, and Python. It is available publicly online under the GNU General Public License, at '<http://code.google.com/p/scatterlib/>'.

In this thesis, I used the C translation of the Bohren-Huffman code. Some modifications were made to 'main()' in '*bhmie.c*'. The inputs are broken down into the index of refraction of the sphere, the index of refraction of the surrounding medium, wavelength of incident light in vacuum, radius of the sphere, and resolution for the x-axis. The output has been simplified to provide only θ , the angle between the incident and scattered rays in degrees, and real outputs for scattered polarized intensity of i_1 and i_2 , in arbitrary units. The imaginary component of the index of refraction of the medium and sphere were assumed to be small and negligible. Thus, only real indexes of refractions were used, generating intensities that were also real. The function 'bhmie()', which implements the Bohren-Huffman Mie scattering algorithm from the original Fortran code, was left unchanged. Below is the modified 'main()' function.

```
int main(void)
/*-----
INPUTS: nang, n_cell, n_med, lambda, a
        Note that nang <= 500 or stack overflow will occur

OUTPUTS: theta(degrees), i_1 (a.u.), i_2 (a.u.)
-----*/
```

```

{

    float x;
    float a;
    float lambda;

    float n_cell;
    float n_med;
    fcomplex cxref;
    float nang;
    fcomplex cxs1[mxnang], cxs2[mxnang];
    float qext, qsca, qback, gsca;

    float theta;
    unsigned long i;

    void bhmie(float x, fcomplex cxref, unsigned long nang,
               fcomplex cxs1[], fcomplex cxs2[],
               float *qext, float *qsca, float *qback, float
               *gsca);

    nang=500;           //number of angles between 0 and 90 degrees
    n_cell=1.59;        //index of refraction of sphere
    n_med=1.334;        //index of refraction of surrounding medium
    cxref=Complex(n_cell/n_med,0);

    lambda = 0.532; // wavelength in um
    a = 15/2;         // radius of sphere in um

```

```
x=(2*3.14159*a*n_med)/lambda;

bhmie(x, cxref, nang, cxs1, cxs2, &qext, &q sca, &qback, &gsca);

for (i=1; i<=2*nang - 1; i++) {
    theta = 90*(i-1)/nang;           //converts i-count to
    theta in degrees
    printf("%f,%f,%f\n", theta, (cxs1[i].r)*(cxs1[i].r),
        (cxs2[i].r)*(cxs2[i].r));
}
}
```

A.3 Scatter intensity

It was noticed in Chapter 5 that some cells had an overall higher scatter intensity than others, which affected how easily their scatter patterns could be viewed. Thus, it might be a possibility that cells can not only be differentiated by their scatter patterns but also by their overall scatter intensity. This makes the analysis faster and simpler to perform. This was attempted both theoretically, using Mie theory as described in Section 2.3, and experimentally on a CD34+ cell. This was not included in the main body of work due to the study's inconclusiveness. Nevertheless, the author thinks that it is a good exercise that can be redone when images with lower SNR are attained.

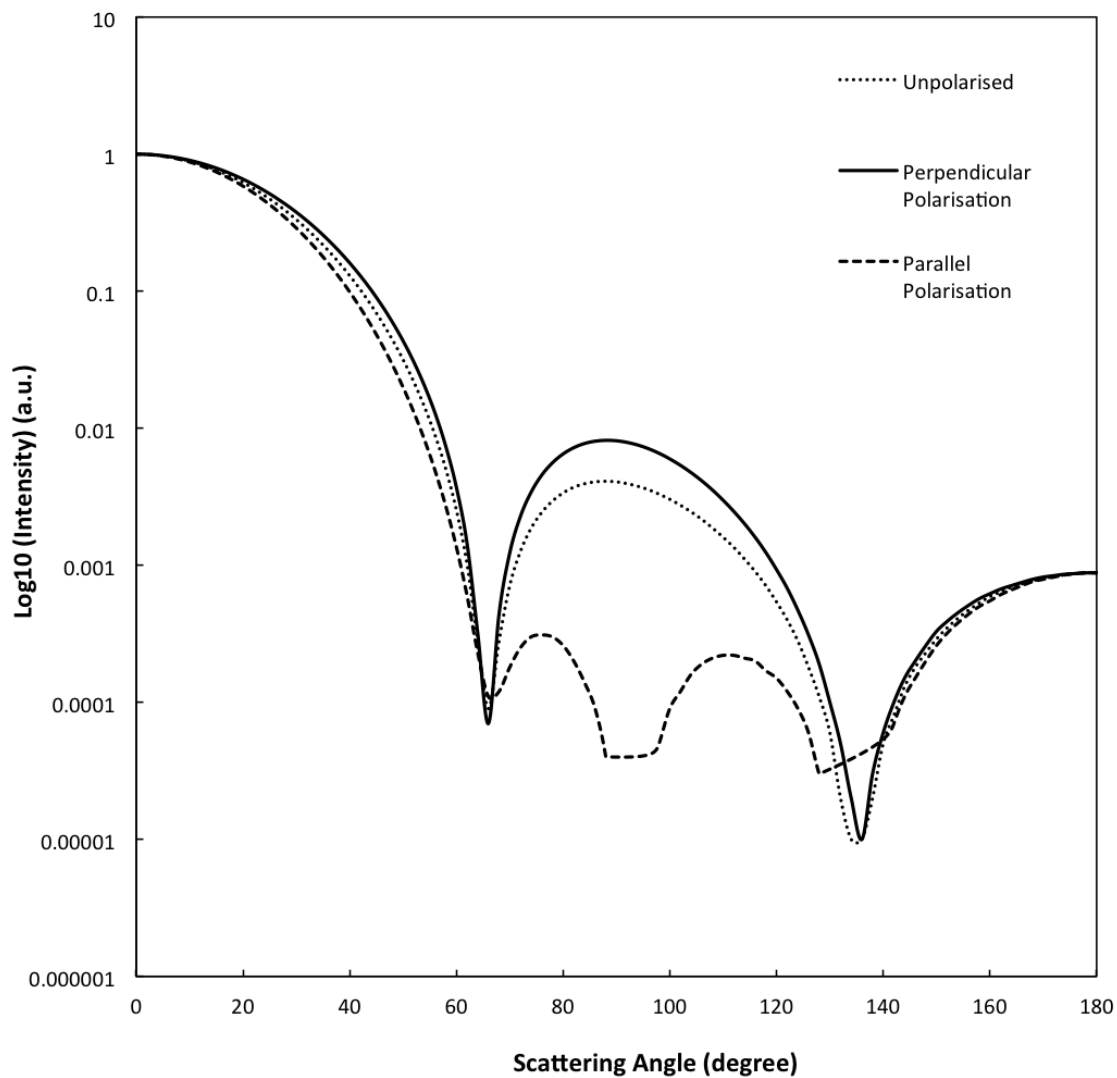


Figure 7.7: Mie scatter for a CD34+ cell with 72 mitochondria.

A.3.1 Determining scatter intensity with Mie calculations

In order to determine the scatter intensity over this collection range, we must solve for intensities using Mie Theory, Section 2.3. Since the calculations are long and involved, there are many versions of code available to calculate Mie scatter. This includes Fortran, C and Matlab code. Here, I have used a simple web-based calculator written by Scott Prahl [101] to demonstrate the Mie solution to scatter from a 532nm wave on a CD34+ cell. As only one homogeneous sphere can be modelled at a time, the CD34+ cell is approximated by its mitochondria, with a diameter of $0.5 \mu\text{m}$ and n of 1.42. The surrounding medium, cytoplasm, has a diameter of $6.5 \mu\text{m}$ and n of 1.38. Assuming that there are 72 mitochondria in a CD34+ cell, as Su approximated in his 2011 paper [26], the concentration of spheres can be calculated to be

$$\text{Concentration} = \frac{\text{Number of mitochondria}}{\text{Volume of cell}} = 0.5 \text{spheres}/\mu\text{m}^3. \quad (7.1)$$

Figure 7.7 shows the scattered intensity in arbitrary units over the angular range of 0° to 180° . The data is normalised to the maximum intensity, I_0 , at 0° . The normalised scatter intensity was then plotted on a logarithmic scale. Data for unpolarised, perpendicular polarisation, and parallel polarisation is shown. Since the laser used in this experiment is TM polarised, only the perpendicular polarisation will be considered.

Integrating under the curve for the angular range of 79° to 101° , I get a normalised intensity of 0.16 for a CD34+ cell. This number is incredibly approximate as it ignores scattering from other organelles in the cell. It also assumes the mitochondria to be evenly distributed in the cell and assumes there to be 72 mitochondria in the cell. Lastly, it takes the index of refraction of the medium to be that of the cytoplasm and ignores the radius of the cell and the existence of the water surrounding it. The

experimental normalised intensity should be higher than this.

A.3.2 Experimental scatter intensity

Overall scatter intensity can be collected with a photomultiplier tube (PMT) or using the scatter images as done in Section 5.5. I chose the latter method, as the experimental setup did not have to be changed.

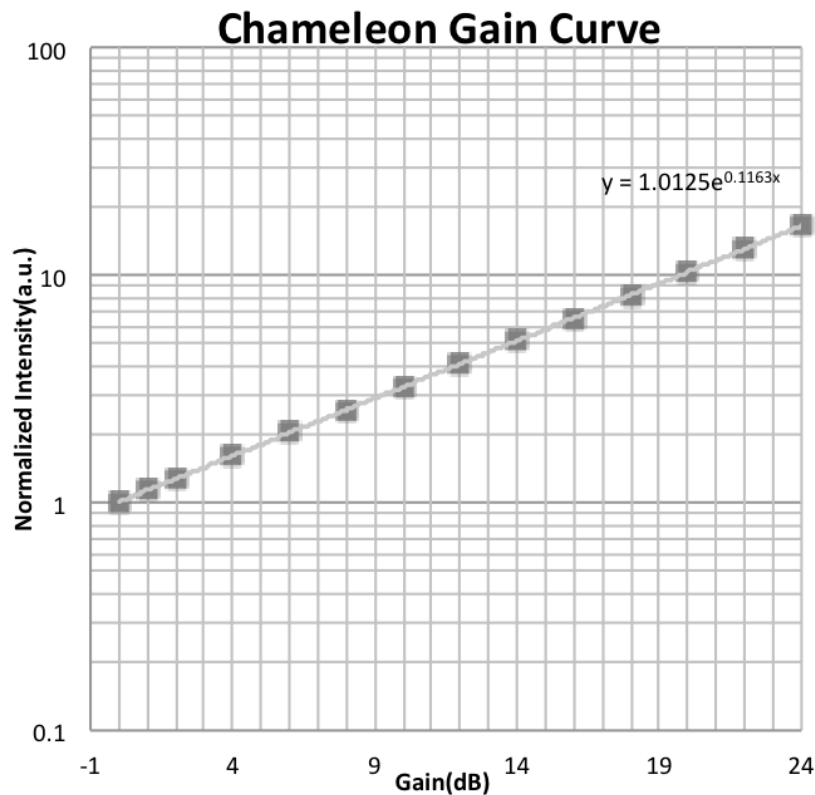


Figure 7.8: Chameleon CCD calibration curves of gain vs. normalised intensity [100]

For intensity measurements, software settings were recorded and not changed for the duration of the experiment. The settings used are shown in Table 7.1. However, it was necessary to adjust the software gain setting to ensure that pixels were not saturated and data was not lost. The gain setting differs due to the effectiveness of

Table 7.1: Software settings used for Intensity measurements

Brightness	6.238
Exposure	-0.061
Gamma	1
Pan	0
Tilt	0
Shutter	33.328 ms

different waveguides for each chip, fibre coupling efficiency, and also depending on the type of cell used, as some cells scatter more readily than others. The gain was then corrected for using calibration data for the chameleon CCD array [100], relating the gain to normalised intensity as shown in Figure 7.8. The image was only defocused by $100\mu\text{m}$ (as opposed to $200\mu\text{m}$ for the scattering images) to make it easier to identify by eye.

Scatter intensity for a CD34+ cell was determined from collected scatter pattern. When defocused by $100\mu\text{m}$, CD34+ cells were determined to have a diameter of approximately 60 pixels. Thus, a circular area with a diameter of 60 pixels was selected around the scattered cell image as shown in Figure 7.9. Imaging processing software ImageJ was used to extract an intensity histogram for the selected area. The overall output intensity in arbitrary units was determined by multiplying the intensity with the number of pixels with that intensity, and then it was averaged by the total number of pixels in the selection. If the gain was changed, the data was normalised with the use of Figure 7.8. To eliminate the possibility of different intensities due to changes in the light level, this data was normalised by the average intensity of a rectangular area (50 x 70 pixels) within the waveguide when the image is in focus, taking care to ensure that the image is not saturated. This normalisation ensures that the data collected is independent of a change in input light levels between

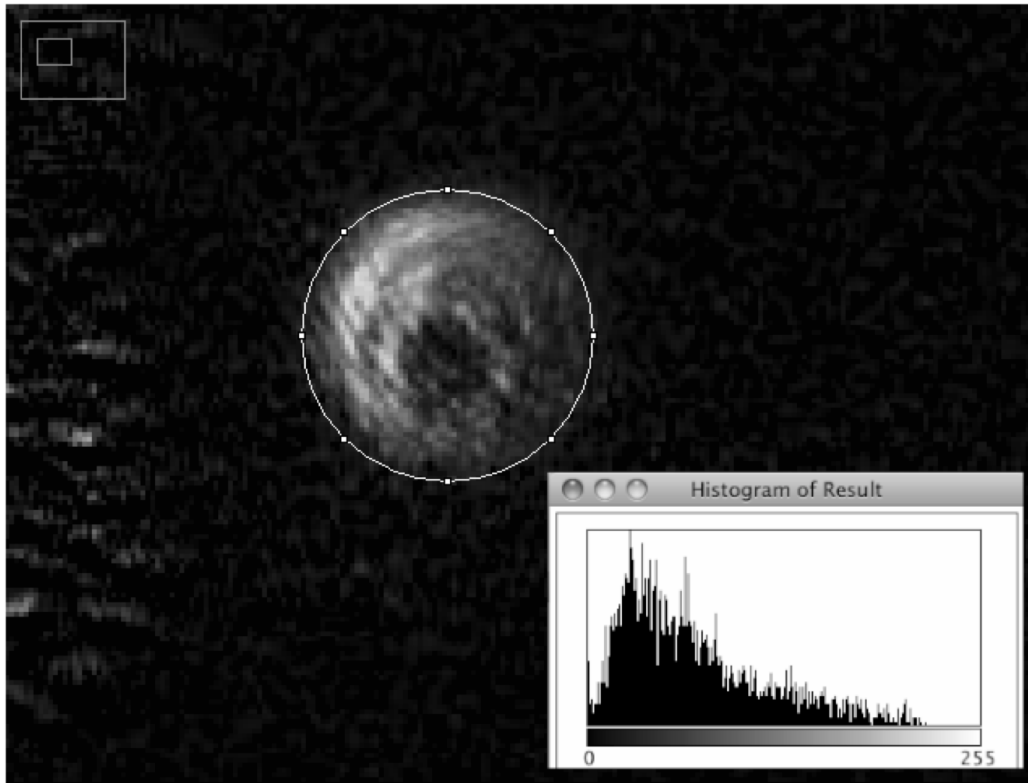


Figure 7.9: Selection in ImageJ of a 60 pixel circular area for the scatter pattern from a CD34+ cell with a histogram of the selection showing intensity data.

experiments. Results are shown in Figure 7.10.

As seen from the results, the scatter intensity for CD34+ varies widely. This is due to the variance of the cell within the channel, as the cell would scatter more light if it is closer and inline with the waveguide. From Figure 7.10, sample 2 and 4 were very well aligned with the light in the channel and this resulted in large intensities. Sample 1, 3, 5, and 6 were not as well aligned resulting in lower intensities. These lower intensities have an average of 0.22 which is 37% higher than the theoretical value. This could be due to factors and additional scatterers that the theoretical model did not take into account.

Thus, differentiating cells by intensity does not seem probable at this time as it

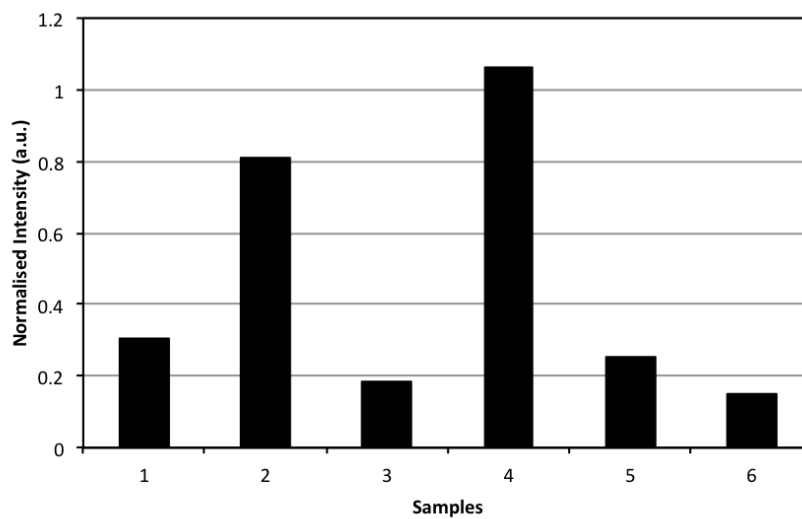


Figure 7.10: Normalised intensity for discrete CD34+ samples.

requires the cell to be in the same predictable position in the channel. This can be achieved through hydrodynamic focusing to limit the flow of the cell to the centre of the channel. 2D hydrodynamic focusing was explored in Chapter 6. More work has to be done to determine if collecting scatter intensity is a feasible option for the label-free cell cytometer.

A.4 Raw data for pressure to flow speed calibrations

The raw data required for the spherical volume test is listed as follows:

r , radius of falling drop = 470 ± 20 pixels = $2022 \pm 235 \mu\text{m}$

V , volume of falling drop = $4.33 \pm 0.5 \text{ mm}^3$

The raw data required for the pendant drop method is listed as follows:

σ , surface tension = $7.28\text{e-}2 \text{ N/m}^2$ [77]

ρ , density = 998 kg/m^3 [77]

g , gravity = 9.8 m/s^2

b , radius of curvature = 238 ± 5 pixels = $1020 \pm 113 \mu\text{m}$

z_0 , length of drop = 570 ± 10 pixels = $2450 \pm 269 \mu\text{m}$

r_0 , radius of dropping tip = 49.5 ± 5 pixels = $213 \pm 32 \mu\text{m}$

V , volume of drop = $8.23 \pm 1.14 \text{ mm}^3$

For a $200 \mu\text{m}$ wide channel,

A , cross-sectional area = $(200 \pm 5 \times 60 \pm 5) \mu\text{m} = 12000 \pm 1044 \mu\text{m}^2$

For a $60 \mu\text{m}$ wide channel,

A , cross-sectional area = $(60 \pm 5 \times 60 \pm 5) \mu\text{m} = 3600 \pm 424 \mu\text{m}^2$

Table 7.2: Raw data for pressure to flow speed calculations in a 200 μm wide channel, see Section 6.3.

Pressure		Time			Sperical volume test				Pendant drop test			
Pressure (mbarr)	Error	Δ Frame	Δ Time(s)	Error	Average Volume (μm^3)	Error	Speed (mm/s)	Error	Average Volume (μm^3)	Error	Speed (mm/s)	Error
0	0.0	0	0	0	0	0	0	0	0	0	0	0
12	2.6	173	173	2.8	4.33E+09	5.03E+08	2.1	0.3	8.23E+09	1.14E+09	4.0	0.7
12	2.6	177	177	2.8	4.33E+09	5.03E+08	2.0	0.3	8.23E+09	1.14E+09	3.9	0.6
12	2.6	178	178	2.8	4.33E+09	5.03E+08	2.0	0.3	8.23E+09	1.14E+09	3.9	0.6
12	2.6	182	182	2.8	4.33E+09	5.03E+08	2.0	0.3	8.23E+09	1.14E+09	3.8	0.6
12	2.6	184	184	2.8	4.33E+09	5.03E+08	2.0	0.3	8.23E+09	1.14E+09	3.7	0.6
15	2.6	115	115	2.8	4.33E+09	5.03E+08	3.1	0.5	8.23E+09	1.14E+09	6.0	1.0
15	2.6	137	137	2.8	4.33E+09	5.03E+08	2.6	0.4	8.23E+09	1.14E+09	5.0	0.8
15	2.6	140	140	2.8	4.33E+09	5.03E+08	2.6	0.4	8.23E+09	1.14E+09	4.9	0.8
15	2.6	141	141	2.8	4.33E+09	5.03E+08	2.6	0.4	8.23E+09	1.14E+09	4.9	0.8
15	2.6	144	144	2.8	4.33E+09	5.03E+08	2.5	0.4	8.23E+09	1.14E+09	4.8	0.8
27	2.6	65	65	2.8	4.33E+09	5.03E+08	5.5	0.8	8.23E+09	1.14E+09	10.5	1.8
27	2.6	66	66	2.8	4.33E+09	5.03E+08	5.5	0.8	8.23E+09	1.14E+09	10.4	1.8
27	2.6	66	66	2.8	4.33E+09	5.03E+08	5.5	0.8	8.23E+09	1.14E+09	10.4	1.8
27	2.6	67	67	2.8	4.33E+09	5.03E+08	5.4	0.8	8.23E+09	1.14E+09	10.2	1.7
27	2.6	66	66	2.8	4.33E+09	5.03E+08	5.5	0.8	8.23E+09	1.14E+09	10.4	1.8
27	2.6	67	67	2.8	4.33E+09	5.03E+08	5.4	0.8	8.23E+09	1.14E+09	10.2	1.7
40	2.6	1421	47	0.094	4.33E+09	5.03E+08	7.6	1.1	8.23E+09	1.14E+09	14.5	2.4
40	2.6	1433	48	0.094	4.33E+09	5.03E+08	7.5	1.1	8.23E+09	1.14E+09	14.4	2.3
40	2.6	1432	48	0.094	4.33E+09	5.03E+08	7.6	1.1	8.23E+09	1.14E+09	14.4	2.4
40	2.6	1435	48	0.094	4.33E+09	5.03E+08	7.5	1.1	8.23E+09	1.14E+09	14.3	2.3
40	2.6	1439	48	0.094	4.33E+09	5.03E+08	7.5	1.1	8.23E+09	1.14E+09	14.3	2.3
40	2.6	1440	48	0.094	4.33E+09	5.03E+08	7.5	1.1	8.23E+09	1.14E+09	14.3	2.3
65	2.6	838	28	0.094	4.33E+09	5.03E+08	12.9	1.9	8.23E+09	1.14E+09	24.5	4.0
65	2.6	839	28	0.094	4.33E+09	5.03E+08	12.9	1.9	8.23E+09	1.14E+09	24.5	4.0
65	2.6	841	28	0.094	4.33E+09	5.03E+08	12.9	1.9	8.23E+09	1.14E+09	24.5	4.0
65	2.6	841	28	0.094	4.33E+09	5.03E+08	12.9	1.9	8.23E+09	1.14E+09	24.5	4.0
65	2.6	843	28	0.094	4.33E+09	5.03E+08	12.8	1.9	8.23E+09	1.14E+09	24.4	4.0
65	2.6	842	28	0.094	4.33E+09	5.03E+08	12.8	1.9	8.23E+09	1.14E+09	24.4	4.0
90	2.6	579	19	0.094	4.33E+09	5.03E+08	18.7	2.7	8.23E+09	1.14E+09	35.5	5.8
90	2.6	579	19	0.094	4.33E+09	5.03E+08	18.7	2.7	8.23E+09	1.14E+09	35.5	5.8
90	2.6	578	19	0.094	4.33E+09	5.03E+08	18.7	2.7	8.23E+09	1.14E+09	35.6	5.8
90	2.6	580	19	0.094	4.33E+09	5.03E+08	18.6	2.7	8.23E+09	1.14E+09	35.5	5.8
90	2.6	580	19	0.094	4.33E+09	5.03E+08	18.6	2.7	8.23E+09	1.14E+09	35.5	5.8
90	2.6	580	19	0.094	4.33E+09	5.03E+08	18.6	2.7	8.23E+09	1.14E+09	35.5	5.8
115	2.6	446	15	0.094	4.33E+09	5.03E+08	24.2	3.5	8.23E+09	1.14E+09	46.1	7.6
115	2.6	446	15	0.094	4.33E+09	5.03E+08	24.2	3.5	8.23E+09	1.14E+09	46.1	7.6
115	2.6	447	15	0.094	4.33E+09	5.03E+08	24.2	3.5	8.23E+09	1.14E+09	46.0	7.5
115	2.6	445	15	0.094	4.33E+09	5.03E+08	24.3	3.5	8.23E+09	1.14E+09	46.2	7.6
115	2.6	446	15	0.094	4.33E+09	5.03E+08	24.2	3.5	8.23E+09	1.14E+09	46.1	7.6
115	2.6	447	15	0.094	4.33E+09	5.03E+08	24.2	3.5	8.23E+09	1.14E+09	46.0	7.5

Table 7.3: Raw data for pressure to flow speed calculations in a 60 μm wide channel, see Section 6.3.

Pressure		Time			Spherical volume test				Pendant drop test			
Pressure (mbarr)	Error	Δ Frame	Δ Time(s)	Error	Average Volume (μm^3)	Error	Speed (mm/s)	Error	Average Volume (μm^3)	Error	Speed (mm/s)	Error
0	0	0	0.0	0.0	0	0	0	0	0	0	0	0
14.9	2.5	2805	2805	2.8	4.33E+09	5.03E+08	0.4	0.1	8.23E+09	1.14E+09	0.8	0.1
14.9	2.5	2484	2484	2.8	4.33E+09	5.03E+08	0.5	0.1	8.23E+09	1.14E+09	0.9	0.2
14.9	2.5	3617	3617	2.8	4.33E+09	5.03E+08	0.3	0.1	8.23E+09	1.14E+09	0.6	0.1
14.9	2.5	2441	2441	2.8	4.33E+09	5.03E+08	0.5	0.1	8.23E+09	1.14E+09	0.9	0.2
14.9	2.5	3164	3164	2.8	4.33E+09	5.03E+08	0.4	0.1	8.23E+09	1.14E+09	0.7	0.1
27.4	2.5	946	946	2.8	4.33E+09	5.03E+08	1.3	0.2	8.23E+09	1.14E+09	2.4	0.4
27.4	2.5	1275	1275	2.8	4.33E+09	5.03E+08	0.9	0.2	8.23E+09	1.14E+09	1.8	0.3
27.4	2.5	1126	1126	2.8	4.33E+09	5.03E+08	1.1	0.2	8.23E+09	1.14E+09	2.0	0.4
27.4	2.5	1057	1057	2.8	4.33E+09	5.03E+08	1.1	0.2	8.23E+09	1.14E+09	2.2	0.4
27.4	2.5	1088	1088	2.8	4.33E+09	5.03E+08	1.1	0.2	8.23E+09	1.14E+09	2.1	0.4
39.9	2.5	17078	569	0.094	4.33E+09	5.03E+08	2.1	0.3	8.23E+09	1.14E+09	4.0	0.7
39.9	2.5	16730	558	0.094	4.33E+09	5.03E+08	2.2	0.4	8.23E+09	1.14E+09	4.1	0.7
39.9	2.5	15992	533	0.094	4.33E+09	5.03E+08	2.3	0.4	8.23E+09	1.14E+09	4.3	0.8
39.9	2.5	16301	543	0.094	4.33E+09	5.03E+08	2.2	0.4	8.23E+09	1.14E+09	4.2	0.8
39.9	2.5	17065	569	0.094	4.33E+09	5.03E+08	2.1	0.3	8.23E+09	1.14E+09	4.0	0.7
64.8	2.5	9977	333	0.094	4.33E+09	5.03E+08	3.6	0.6	8.23E+09	1.14E+09	6.9	1.3
64.8	2.5	9864	329	0.094	4.33E+09	5.03E+08	3.7	0.6	8.23E+09	1.14E+09	6.9	1.3
64.8	2.5	10009	334	0.094	4.33E+09	5.03E+08	3.6	0.6	8.23E+09	1.14E+09	6.8	1.2
64.8	2.5	9546	318	0.094	4.33E+09	5.03E+08	3.8	0.6	8.23E+09	1.14E+09	7.2	1.3
64.8	2.5	9491	316	0.094	4.33E+09	5.03E+08	3.8	0.6	8.23E+09	1.14E+09	7.2	1.3
89.7	2.5	6905	230	0.094	4.33E+09	5.03E+08	5.2	0.9	8.23E+09	1.14E+09	9.9	1.8
89.7	2.5	6915	231	0.094	4.33E+09	5.03E+08	5.2	0.9	8.23E+09	1.14E+09	9.9	1.8
89.7	2.5	6932	231	0.094	4.33E+09	5.03E+08	5.2	0.9	8.23E+09	1.14E+09	9.9	1.8
89.7	2.5	6882	229	0.094	4.33E+09	5.03E+08	5.2	0.9	8.23E+09	1.14E+09	10.0	1.8
114.6	2.5	5245	175	0.094	4.33E+09	5.03E+08	6.9	1.1	8.23E+09	1.14E+09	13.1	2.4
114.6	2.5	5254	175	0.094	4.33E+09	5.03E+08	6.9	1.1	8.23E+09	1.14E+09	13.0	2.4
114.6	2.5	5247	175	0.094	4.33E+09	5.03E+08	6.9	1.1	8.23E+09	1.14E+09	13.1	2.4
114.6	2.5	5254	175	0.094	4.33E+09	5.03E+08	6.9	1.1	8.23E+09	1.14E+09	13.0	2.4
114.6	2.5	5233	174	0.094	4.33E+09	5.03E+08	6.9	1.1	8.23E+09	1.14E+09	13.1	2.4

A.5 Raw data for hydrodynamic focused ratio to a ratio of pressures

Table 7.4: Raw data for Hydrodynamic focused ratio of sheath to sample as a function of increasing flow ratios for different main flow pressures, see Section 6.4.

Pressure (inH2O)		Ratio of Sheath to Sample		Focusing			
Main Flow	Sheath Flow	Ratio	Error	Focused Stream (px)	Focused Stream (μm)	Ratio	Error
17.5	16	0.91	0.04	50	200	1	0.05
17.5	17	0.97	0.04	48	192	0.96	0.05
17.5	18	1.03	0.04	32	128	0.64	0.05
17.5	19	1.09	0.04	28	112	0.56	0.05
17.5	20	1.14	0.04	22	88	0.44	0.05
17.5	21	1.20	0.05	17	68	0.34	0.05
17.5	22	1.26	0.05	9	36	0.18	0.05
17.5	23	1.31	0.05	6	24	0.12	0.05
17.5	24	1.37	0.05	0	0	0	0.05
12.5	11	0.88	0.05	50	200	1	0.05
12.5	12	0.96	0.06	41	164	0.82	0.05
12.5	13	1.04	0.06	30	120	0.6	0.05
12.5	14	1.12	0.06	22	88	0.44	0.05
12.5	15	1.20	0.06	10	40	0.2	0.05
12.5	16	1.28	0.07	4	16	0.08	0.05
12.5	17	1.36	0.07	0	0	0	0.05
7.5	7	0.93	0.09	50	200	1	0.05
7.5	8	1.07	0.10	34	136	0.68	0.05
7.5	9	1.20	0.11	16	64	0.32	0.05
7.5	10	1.33	0.11	6	24	0.12	0.05
7.5	11	1.47	0.12	0	0	0	0.05
5.5	4.5	0.82	0.12	50	200	1	0.05
5.5	5	0.91	0.13	36	144	0.72	0.05
5.5	6	1.09	0.14	17	68	0.34	0.05
5.5	7	1.27	0.15	9	36	0.18	0.05
5.5	7.5	1.36	0.16	0	0	0	0.05

A.6 LabVIEW code for fluorescent bead sorting

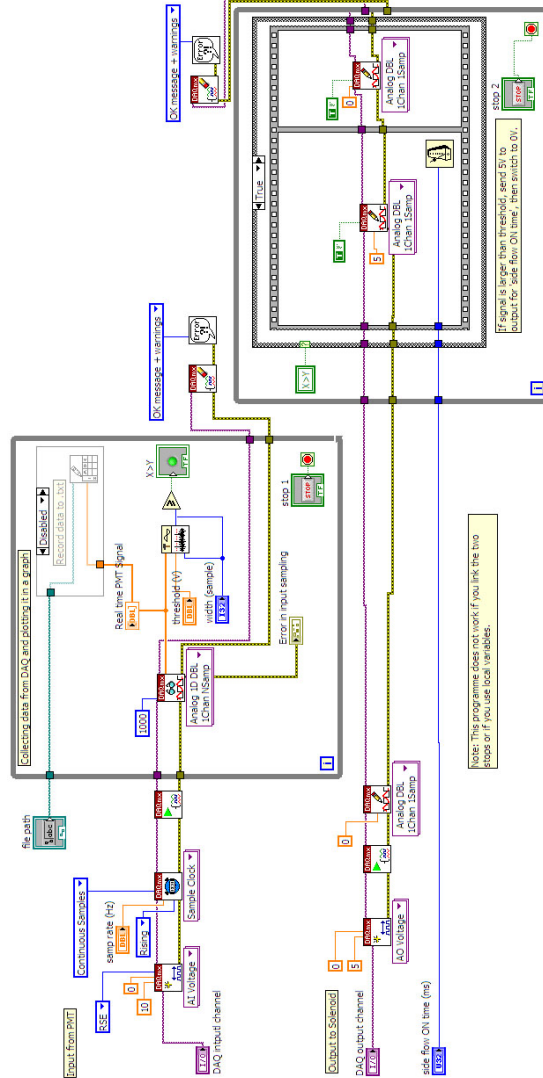


Figure 7.11: Back panel of LabVIEW showing the signal collection from the PMT which triggers the solenoid valve after a delay when the signal exceeds a threshold value for a certain amount of time.